

International Journal of Photoenergy

# Advanced Solar Technologies in Buildings

Lead Guest Editor: Mattia De Rosa

Guest Editors: Paolo Conti, Yasser M. Larimi, and Vincenzo Bianco





---

# **Advanced Solar Technologies in Buildings**

International Journal of Photoenergy

---

## **Advanced Solar Technologies in Buildings**

Lead Guest Editor: Mattia De Rosa

Guest Editors: Paolo Conti, Yasser M. Larimi,  
and Vincenzo Bianco



---

Copyright © 2019 Hindawi. All rights reserved.

This is a special issue published in "International Journal of Photoenergy." All articles are open access articles distributed under the Creative Commons Attribution License, which permits unrestricted use, distribution, and reproduction in any medium, provided the original work is properly cited.

## Editorial Board

M. S.A. Abdel-Mottaleb, Egypt  
Angelo Albini, Italy  
Alberto Álvarez-Gallegos, Mexico  
Vincenzo Augugliaro, Italy  
Detlef W. Bahnemann, Germany  
Simona Binetti, Italy  
Fabio Bisegna, Italy  
Thomas M. Brown, Italy  
Joaquim Carneiro, Portugal  
Yatendra S. Chaudhary, India  
Yong Chen, China  
Věra Cimrová, Czech Republic  
Gianluca Coccia, Italy  
Juan M. Coronado, Spain  
P. Davide Cozzoli, Italy  
Dionysios D. Dionysiou, USA  
Abderrazek Douhal, Spain  
Mahmoud M. El-Nahass, Egypt  
Polycarpos Falaras, Greece  
Chris Ferekides, USA  
Paolo Fornasiero, Italy  
Manuel Fuentes Conde, Spain  
Germà Garcia-Belmonte, Spain

Elisa Isabel Garcia-Lopez, Italy  
M. Ashraf Gondal, Saudi Arabia  
Giulia Grancini, Switzerland  
Pierluigi Guerriero, Italy  
Michael D. Heagy, USA  
Wing-Kei Ho, Hong Kong  
Jürgen Hüpkes, Germany  
M. Tariq Iqbal, Canada  
Adel A. Ismail, Kuwait  
Chun-Sheng Jiang, USA  
Zaiyong Jiang, China  
Cooper H. Langford, Canada  
Yuanzuo Li, China  
Manuel Ignacio Maldonado, Spain  
Santolo Meo, Italy  
Claudio Minero, Italy  
Antoni Morawski, Poland  
Fabrice Morlet-Savary, France  
Mohammad Muneer, India  
Maria da Graça P. Neves, Portugal  
Tsuyoshi Ochiai, Japan  
Kei Ohkubo, Japan  
Leonardo Palmisano, Italy

Thierry Pauporté, France  
Juan Manuel Peralta-Hernández, Mexico  
Philippe Poggi, France  
Carlo Renno, Italy  
Francesco Riganti-Fulginei, Italy  
Leonardo Sandrolini, Italy  
Jinn Kong Sheu, Taiwan  
Kishore Sridharan, India  
Zofia Stasicka, Poland  
Elias Stathatos, Greece  
Jegadesan Subbiah, Australia  
K. R. Justin Thomas, India  
Nikolai V. Tkachenko, Finland  
Koray Ulgen, Turkey  
Ahmad Umar, Saudi Arabia  
Thomas Unold, Germany  
Mark van Der Auweraer, Belgium  
Wilfried G.J.H.M. Van Sark, Netherlands  
Xuxu Wang, China  
Huiqing Wen, China  
Yanfa Yan, USA  
Jiangbo Yu, USA

# Contents

---

## **Advanced Solar Technologies in Buildings**

Mattia De Rosa , Paolo Conti, Yasser Mahmoudi, and Vincenzo Bianco  
Editorial (2 pages), Article ID 1709375, Volume 2019 (2019)

## **An Improved Empirical Model for Estimation of Temperature Effect on Performance of Photovoltaic Modules**

Abdul Rehman Jatoi , Saleem Raza Samo, and Abdul Qayoom Jakhrani  
Research Article (16 pages), Article ID 1681353, Volume 2019 (2019)

## **Design and Dynamic Modelling of a Hybrid Power System for a House in Nigeria**

Lawrence O. Aghenta , and M. Tariq Iqbal   
Research Article (13 pages), Article ID 6501785, Volume 2019 (2019)

## **Flexible, Front-Facing Luminescent Solar Concentrators Fabricated from Lumogen F Red 305 and Polydimethylsiloxane**

Ian A. Carbone , Katelynn R. Frawley, and Melissa K. McCann  
Research Article (9 pages), Article ID 8680931, Volume 2019 (2019)

## **Design and Analysis of a Stand-Alone PV System for a Rural House in Pakistan**

Amjad Iqbal , and M. Tariq Iqbal   
Research Article (8 pages), Article ID 4967148, Volume 2019 (2019)

## **Performance Modelling of Dual Air/Water Collector in Solar Water and Space Heating Application**

Viacheslav Shemelin , and Tomas Matuska   
Research Article (10 pages), Article ID 8560193, Volume 2019 (2019)

## **Numerical Investigations on Charging/Discharging Performance of a Novel Truncated Cone Thermal Energy Storage Tank on a Concentrated Solar Power System**

Qianjun Mao , Ning Liu, and Li Peng   
Research Article (17 pages), Article ID 1609234, Volume 2019 (2019)

## Editorial

# Advanced Solar Technologies in Buildings

**Mattia De Rosa** <sup>1</sup>, **Paolo Conti**<sup>2</sup>, **Yasser Mahmoudi**<sup>3</sup>, and **Vincenzo Bianco**<sup>4</sup>

<sup>1</sup>*UCD Energy Institute, University College Dublin, Belfield, Dublin 4, Ireland*

<sup>2</sup>*Department of Energy, Systems, Territory and Constructions Engineering (DESTEC), University of Pisa, Italy*

<sup>3</sup>*School of Mechanical and Aerospace Engineering, Queen's University Belfast, Stranmillis Road, Belfast BT95AG, UK*

<sup>4</sup>*DIME/TEC, Division of Thermal Energy and Environmental Conditioning, University of Genoa, Genoa 16145, Italy*

Correspondence should be addressed to Mattia De Rosa; [mattia.derosa@ucd.ie](mailto:mattia.derosa@ucd.ie)

Received 17 June 2019; Accepted 19 June 2019; Published 4 July 2019

Copyright © 2019 Mattia De Rosa et al. This is an open access article distributed under the Creative Commons Attribution License, which permits unrestricted use, distribution, and reproduction in any medium, provided the original work is properly cited.

The global growth of energy demand is putting pressure on establishing regulatory frameworks aimed at reducing the carbon footprint of our societies, thus mitigating the climate change. For instance, one of the main targets of the European Union's energy policies is the reduction of greenhouse emissions by 80-95% by 2050 [1]. Such decarbonisation process, as envisioned by most researchers and policy makers, requires policies promoting investments to support new low-carbon solutions, efficiency measures, and people behavioural changes.

Renewable energies are recognised as one of the most important pillars for achieving a more sustainable society. A recent report by the International Renewable Energy Agency (IRENA) indicates that the share of renewable energy in the power sector would increase from 25% in 2017 to 85% by 2050, mostly through growth in wind and solar power generation [2]. Therefore, greater efforts should be made to achieve a higher and widespread penetration of renewables in all economic sectors.

In this context, solar energy has been the subject of intense research and development efforts thanks to its promising and unmatched resource potential, which led to a large diffusion as residential, commercial, and industrial solar appliances over the last few decades. Among others, buildings represent an important sector for solar energy technologies, since they are responsible for about 39% of the total

primary energy consumption [3]. Therefore, the integration of solar technologies in buildings, such as advanced solar thermal collectors, photovoltaic (PV) and hybrid PV systems, the use of photoactive materials, solar cooling and passive solar systems, and energy storage, may lead to significant primary energy savings and carbon emission reduction.

Further research opportunities are still growing, looking at novel building applications where advanced material devices, integrated system configurations, design and management strategies, novel modelling, and assessment techniques are adopted. On the other hand, making solar energy cost-effective and market ready technologies requires the adoption of innovative modelling approaches and quantitative assessment procedures capable of (i) reducing the environmental and cost impacts of appliance production, installation, and disposal processes (i.e., life-cycle analysis-LCA), (ii) allowing the integration with existing facilities and infrastructures, and (iii) providing technical and economic optimisation of design and management, including control algorithms and smart grid integration.

This special issue is an attempt to collect articles on advanced solar technologies for building applications. It includes numerical and experimental works on photovoltaic systems and their integration at building level, novel solar concentrators, hybrid thermal-power systems, and energy storage coupled with thermal solar systems.

## Conflicts of Interest

The editors declare that they have no conflicts of interest regarding the publication of this special issue.

*Mattia De Rosa*  
*Paolo Conti*  
*Yasser Mahmoudi*  
*Vincenzo Bianco*

## References

- [1] European Commission, “2050 Energy Strategy. Online Report,” June 2019, <https://ec.europa.eu/energy/en/topics/energy-623-strategy-and-energy-union/2050-energy-strategy>.
- [2] International Energy Agency, “Renewable 2018 – market analysis and forecast from 2018 to 2023. Report,” 2018.
- [3] International Energy Agency, “Transition to sustainable buildings. Strategies and opportunities to 2050,” Technical Report, International Energy Agency, 2013.

## Research Article

# An Improved Empirical Model for Estimation of Temperature Effect on Performance of Photovoltaic Modules

Abdul Rehman Jatoi <sup>1</sup>, Saleem Raza Samo,<sup>1</sup> and Abdul Qayoom Jakhrani<sup>2</sup>

<sup>1</sup>Energy and Environment Engineering Department, Quaid-e-Awam University of Engineering Science and Technology (QUEST), Nawabshah 67480, Pakistan

<sup>2</sup>Chemical Engineering Department, Quaid-e-Awam University of Engineering Science and Technology (QUEST), Nawabshah 67480, Pakistan

Correspondence should be addressed to Abdul Rehman Jatoi; arjatoi@quest.edu.pk

Received 22 March 2019; Revised 23 May 2019; Accepted 30 May 2019; Published 4 July 2019

Guest Editor: Paolo Conti

Copyright © 2019 Abdul Rehman Jatoi et al. This is an open access article distributed under the Creative Commons Attribution License, which permits unrestricted use, distribution, and reproduction in any medium, provided the original work is properly cited.

It is prerequisite to predict the behaviour of photovoltaic (PV) modules in a particular geographical area where the system is to be installed for their better performance and increasing lifetime. For that, models are the easiest and acceptable tools to characterise the behaviour of PV modules in any location. The purpose of this study was to develop an empirical model to predict the influence of temperature on the performance of four different PV module technologies, namely, polycrystalline, monocrystalline, amorphous, and thin film in an outdoor environment. The model has been developed by fitting of one year experimental data using the least squares method. The estimated results of the developed model were validated with real-time data (winter and summer season) and a comparison of other existing model estimates using error analysis with 95% confidence interval. The proposed model estimations confirm that the monocrystalline module performs better in winter and polycrystalline in summer as compared to amorphous and thin film in the study area. During analysis, it is revealed that developed model results are more precise and appropriate among other existing model estimations. It is concluded that the proposed model estimations could be used for the prediction of PV module temperature in similar environmental conditions as that of the study area with more accuracy and confidence. It ultimately helps to develop cost-effective and efficient PV systems.

## 1. Introduction

The intensities of solar radiation, ambient temperature, wind speed, relative humidity, configuration, and method of mounting are considered to be responsible for variations in the power output of photovoltaic (PV) modules [1–6]. PV module temperature is one of the key parameters which affect the performance of photovoltaic (PV) modules after solar radiations [2, 4, 7, 8]. Photovoltaic power output is proportional to the PV module operating temperature [9, 10]. Since the change of PV module temperature depends on the variation of ambient temperature, as ambient temperature increases, the module temperature increases and vice

versa [4, 11]. It is because, the increase of temperature reduces the band gap of a PV module and increases the energy of the electrons in the material, which ultimately increases the recombination rate of internal carriers caused by the increasing amount of carrier concentrations [9, 12–14]. Consequently, it slightly increases the short-circuit current and considerably decreases open-circuit voltage [2, 9, 15]. Weather conditions affect the PV module temperature; therefore, its influence is necessary to be quantified. This can be done with the help of modeling, which eventually helps to design better systems for proper functioning. Several attempts have been made by different authors from different countries to exemplify the behaviour of PV modules. Some

models are intuitive, and others are analytical, numerical, or empirical. Nevertheless, the majority of models are validated in indoor environments of developed countries with the exception of a few in outdoor conditions. It is a very challenging task to develop a model which represents the behaviour of various module technologies simultaneously in outdoor environments. An exact module temperature estimation model is indispensable to achieve reliable data of PV module power output [5, 11, 16–22]. The models used for the prediction of module temperature can be categorized in different ways: steady-state or dynamic, explicit or implicit, etc. [2, 9, 11]. In steady-state modeling, all parameters are assumed to be independent of time (with small time interval, i.e., an hour). However, such models are useful for specific locations and module technologies, while in the dynamic models, some parameters are considered to be varied with respect to time. Dynamic models are preferable for high-resolution input data. Explicit models predict the value of photovoltaic module temperature directly, whereas the implicit correlations involve variables that themselves depend on module temperature. In implicit models, an iteration procedure is compulsory to get the outputs [2, 5, 9, 23–30]. Nevertheless, the selection of an appropriate model is crucial for the design and sizing of photovoltaic systems. The use of an inappropriate model gives faulty predictions thus making the systems over- or undersized. The oversized system becomes costly alternative, whereas undersizing causes malfunctioning of the system. This problem can be controlled through proper sizing and designing of system components with the help of precise modeling and using of long-term reliable data [9, 20, 31–34]. Unfortunately, long-term data are not available in developing countries [31] including Pakistan [35], and the reliability of data is also questionable. Actually, photovoltaic module temperature models are submodels of power output models, as these models predict the effect of temperature on the performance of photovoltaic modules. Most of such models estimate the temperature of photovoltaic modules in indoor conditions but not in outdoor environments [36–38]. The main objective of this study was to develop a simple empirical model for the estimation of the temperature effect on four different PV module technologies, namely, polycrystalline, monocrystalline, amorphous, and thin film in an outdoor environment.

## 2. Existing Photovoltaic Module Temperature Models

In [39], the researchers consider only one basic climatic variable such as the ambient temperature ( $T_a$ ) in their study. It is clear that one input variable does not reflect the whole behavior of the environment. The developed model is given in equation (1) and also used by [40].

$$T_m = 1.411 \times T_a - 6.414. \quad (1)$$

Muzathik [38] suggested three variable models with ambient temperature  $T_a$  (°C), global solar radiation  $G_{sr}$

( $W/m^2$ ), and wind speed  $W_v$  (m/s). The model and coefficients of each variable are provided as given in Equation 2.

$$T_m = 0.943 \times T_a + 0.0195 \times G_{sr} - 1.528 \times W_v + 0.3529. \quad (2)$$

In addition, [2] proposed a simple and semiempirical model for the calculation of module temperature as given in equation (3). The author considered  $T_a$  in (°C),  $G_{sr}$  in ( $W/m^2$ ), and  $W_v$  in (m/s). The same model is reported by [41].

$$T_m = T_a + \left( \frac{0.25}{5.7 + 3.8 \times W_v} \right) \times G_{sr}. \quad (3)$$

Duffie and Beckman [42] proposed a novel mathematical approach for the calculation of photovoltaic module temperature in controlled nominal operating cell temperature (NOCT) conditions:  $0.8 \text{ kW}/m^2$  solar radiation,  $20^\circ\text{C}$  ambient temperature, and  $1 \text{ m}/s$  wind speed. The model depends on the input of  $T_a$  (°C),  $G_{sr}$  ( $W/m^2$ ),  $W_v$  (m/s), and NOCT conditions as given in equation (4). Furthermore, the model is adopted by [9].

$$T_m = T_a + \left( \frac{9.5}{5.7 + 3.8 \times W_v} \right) \left( \frac{G_{sr}}{G_{sr-NOCT}} \right) \cdot (T_{m-NOCT} - T_{a-NOCT}) \left[ 1 - \frac{\eta_m}{\tau_\alpha} \right]. \quad (4)$$

Risser and Fuentes [43] also proposed three variable models with the same variables as that of Muzathik [38] as given in equation 5. The author considered  $T_a$  in (°C),  $G_{sr}$  in ( $W/m^2$ ), and  $W_v$  in (m/s). The same model is tested by [19].

$$T_m = 1.31 \times T_a + 0.0282 \times G_{sr} - 1.65 \times W_v + 3.81. \quad (5)$$

The authors [2, 38, 43] proposed new temperature models which were based on three basic input variables (solar radiations " $G_{sr}$ ," ambient temperature " $T_a$ ," and wind speed " $W_v$ "). The researchers proposed linear models in their studies, but the behaviour of climatic data is parabolic with respect to time. In the morning hours, the intensities of  $G_{sr}$  and  $T_a$  are directly proportional, but in the evening, these are less related due to the slight decreasing trend of temperature as compared to the sharp decrease of solar radiations. The authors [9, 42] proposed a mathematical approach for the calculation of photovoltaic module temperature based on NOCT conditions. Such conditions could not be familiarized with a real outdoor condition.

TABLE 1: Existing PV module models.

Name of author	Empirical models
Rahman et al. [39, 40]	$T_m = 1.411 \times T_a - 6.414$
Muzathik [38]	$T_m = 0.943 \times T_a + 0.0195 \times G_{sr} - 1.528 \times W_v + 0.3529$
Skoplaki et al. [2, 41]	$T_m = T_a + (0.25/5.7 + 3.8 \times W_v) \times G_{sr}$
Duffie and Beckman [9, 42]	$T_m = T_a + (9.5/5.7 + 3.8 \times W_v) (G_{sr}/G_{sr-NOCT}) (T_{m-NOCT} - T_{a-NOCT}) [1 - \eta_m/\tau_\alpha]$
Risser and Fuentes [19, 43]	$T_m = 1.31 \times T_a + 0.0282 \times G_{sr} - 1.65 \times W_v + 3.81$
Almaktar et al. [40]	$T_m = 0.77 \times T_a + 0.023 \times G_{sr} - 0.137 \times W_v - 0.206 \times R_h + 26.97$



(a) Map of Pakistan



(b) Study area

FIGURE 1: Geographical location of the study area (Google Maps).

TABLE 2: Electrical characteristics of examined photovoltaic modules [14, 46].

Module parameters	Unit	Module technologies			
		(p-Si) SUN-40P	(m-Si) SUN-40M	(a-Si) TPS-40	Thin film GS-50
$V_{oc}$	V	43	21.5	29	62
$I_{sc}$	A	1.29	2.55	2.3	1.42
$V_{max}$	V	35	17.5	18	43
$I_{max}$	A	1.14	2.29	2.2	1.17
$P_{max}$	W	40	40	40	50
Area of module	m <sup>2</sup>	0.27	0.24	0.76	0.74

Almaktar et al. [40] proposed a temperature model which depends on four climatic variables, namely, solar radiations “ $G_{sr}$ ,” ambient temperature “ $T_a$ ,” wind speed “ $W_v$ ,” and relative humidity “ $R_h$ ” as given in Equation 6.

$$T_m = 0.77 \times T_a + 0.023 \times G_{sr} - 0.137 \times W_v - 0.206 \times R_h + 26.97. \quad (6)$$

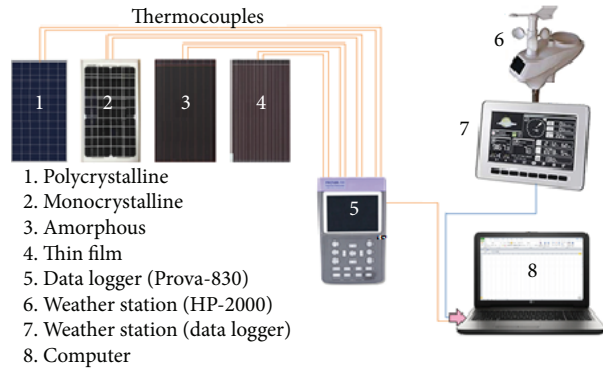
It is already mentioned that the behaviour of climatic data is parabolic in nature with respect to the time of the day. Therefore, in this study, an empirical, nonlinear, multivariate, and least squares model was developed and proposed to calculate the PV module temperature in an outdoor envi-

ronment. Table 1 shows the well-known PV module temperature models.

### 3. Materials and Methods

**3.1. Study Area.** The study was conducted in Nawabshah city, Shaheed Benazirabad District, Sindh, Pakistan, as shown in Figure 1. It is one of the hottest places and located at 26.14°N, 68.23°E [44] and mean 37 m above sea level [45].

**3.2. Experimental Setup.** An experimental setup was installed at the Energy and Environment Engineering Department, QUEST, Nawabshah. Four generic photovoltaic modules (polycrystalline, monocrystalline, amorphous, and thin film) were used in this study, and their specifications are given in

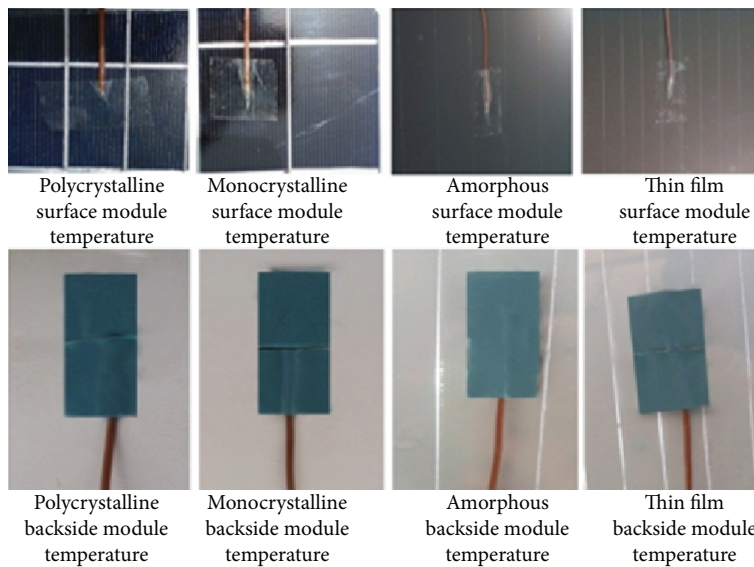


(a) Schematic flow diagram of experimental setup

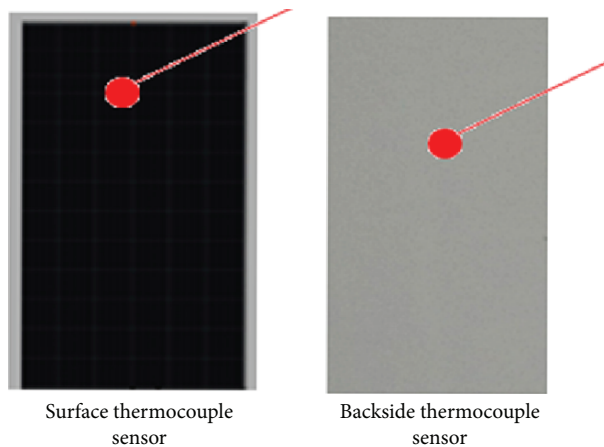


(b) Experimental setup for data logging

FIGURE 2: Experimental setup.



(a) Pasted thermocouples on surface and backside of each PV modules



(b) Positions of thermocouple sensors (surface and backside of PV modules)

FIGURE 3: Pasted thermocouple sensors on the surface and backside of each photovoltaic module.

Table 2. The photovoltaic modules were fixed on an iron structure, facing true south at an inclination of 12° to the horizontal plane. Figure 2 shows the schematic diagram and

experimental setup. The data of each PV module was recorded for a whole year from November, 2015, to October, 2016, for the development of a suitable model for the

TABLE 3: Accuracy of equipment used in this study.

Parameters	Unit	Weather station (HP-2000) Accuracy	Module temperature recorder (Prova-830) Accuracy
$G_{sr}$	$W/m^2$	$\pm 15\%$	—
$T_a$	$^{\circ}C$	$\pm 1.0^{\circ}C$	—
$W_v$	m/s	$\pm 1$ m/s (wind speed < 5) $\pm 10\%$ (wind speed > 5)	—
$R_h$	%	$\pm 5\%$	—
$T_m$	$^{\circ}C$	—	$\pm 0.1\%$ or $1.0^{\circ}C$

prediction of module temperature. The data was measured at an interval of 1 hour from 07 to 18 hours daily. Global solar radiation  $G_{sr}$  ( $W/m^2$ ), ambient temperature  $T_a$  ( $^{\circ}C$ ), wind speed  $W_v$  (m/s), and relative humidity  $R_h$  (%) were measured with HP-2000. Photovoltaic module temperature was recorded with the help of Prova-830 (8 channel thermocouple data logger). A total of eight numbers (two on each PV module) of k-type thermocouples were pasted on the surface and backside of the photovoltaic modules as shown in Figure 3 [14, 46]. The accuracy of equipment used for data measurement is given in Table 3. The temperature sensors were pasted on the surface and backside of photovoltaic module as that of [8], and then, the average of temperature was taken as the module operating temperature [14, 46, 47].

#### 4. Proposed Empirical Model

In this section, we develop a model for the estimation of the temperature effect on different photovoltaic (PV) module technologies, namely, polycrystalline, monocrystalline, amorphous, and thin film in the outdoor environment. In model development, one dependent variable (module temperature) and four basic independent climatic variables (global solar radiation, ambient temperature, wind speed, and relative humidity) were adopted. Furthermore, the correlation of the dependent variable with each independent variable was analyzed. The correlation of module temperature ( $T_m$ ) with the global solar radiation ( $G_{sr}$ ) was found to be 0.89217, ambient temperature ( $T_a$ ) 0.73765, wind speed ( $W_v$ ) 0.075766, and relative humidity ( $R_h$ ) -0.55918. The relationship between climatic parameters and module temperature was found to be nonlinear because of the parabolic curve. Thus, it was deduced from the curve fitting that polynomial models might be suitable models, as these cover the maximum number of measured data points. Further scrutiny of models was made by fitting the data with different degrees of polynomials (1-9 degrees). It was found that the 2<sup>nd</sup> degree polynomial model covers the maximum number of data points of the measured data. Thus, an empirical second degree multivariate nonlinear model was proposed with fitting of data with the least squares method. It was assumed that photovoltaic module temperature ( $T_m$ ) is the function of four variables, namely,  $G_{sr}$ ,  $T_a$ ,  $W_v$ , and  $R_h$ . Thus, the basic function of PV module temperature ( $T_m$ ) is given in equation (7).

$$T_m = f(G_{sr}, T_a, W_v, R_h). \quad (7)$$

The general form of the model would be given in Equation 8.

$$T_m = (a_1 G_{sr} + a_2 T_a + a_3 W_v + a_4 R_h + a_5) \times (b_1 G_{sr} + b_2 T_a + b_3 W_v + b_4 R_h + b_5). \quad (8)$$

By expanding equation (8) with the combination of all four independent variables, equation (9) is developed, which demonstrates the output and input parameters and all involved coefficients.

$$T_m = (a_1 G_{sr} b_2 T_a + a_1 G_{sr} b_3 W_v + a_1 G_{sr} b_4 R_h + a_2 T_a b_1 G_{sr} + a_2 T_a b_3 W_v + a_2 T_a b_4 R_h + a_3 W_v b_1 G_{sr} + a_3 W_v b_2 T_a + a_3 W_v b_4 R_h + a_4 R_h b_1 G_{sr} + a_4 R_h b_2 T_a + a_4 R_h b_3 W_v + a_5 W_v^2 b_3 + a_5 b_4 R_h + a_3 W_v b_5 + a_2 T_a b_5 + a_5 b_3 W_v + a_4 R_h^2 b_4 + a_1 G_{sr} b_5 + a_5 b_1 G_{sr} + a_4 R_h b_5 + a_5 b_2 T_a + a_2 T_a^2 b_2 + a_1 G_{sr}^2 b_1 + a_5 b_5). \quad (9)$$

Let  $T_{m\_meas}$  be the measured module temperature and  $T_{m\_est}$  be the estimated module temperature. The least squares method assumes that the sum of the squares of the residuals (error) is less. Therefore, it can be estimated using Equation 10.

$$E_i = \min \sum_{i=1}^n (T_{m\_meas_i} - T_{m\_est_i}(G_{sr_i}, T_{a_i}, W_{v_i}, R_{h_i}; \beta))^2. \quad (10)$$

where  $i = 1, 2, \dots, n$ , as  $n = 4392$  and  $\beta$  is the set of the coefficients of the model. The minimum value of  $E$  occurs when the gradient is zero. The model contains  $m = 25$  parameters; therefore, the gradient equation is 25. Furthermore, the minimum values of  $E$  and  $r_i$  are calculated through equations (11) and (12).

$$\frac{\partial E_i}{\partial \beta_j} = 2 \sum_{i=1}^n r_i \frac{\partial r_i}{\partial \beta_j} = 0. \quad (11)$$

where  $j = 1, 2, \dots, m = 25$ .

$$r_i = (T_{m\_meas_i} - T_{m\_est_i}(G_{sr_i}, T_{a_i}, W_{v_i}, R_{h_i}; \beta)). \quad (12)$$

TABLE 4: Proposed model coefficients.

Model coefficients	Photovoltaic module technologies			
	Polycrystalline	Monocrystalline	Amorphous	Thin film
$\alpha$	22.5505	31.3750	33.9800	32.4500
$\beta_1$	0.03753	0.03858	0.03622	0.03340
$\beta_2$	$-5.71 \times 10^{-7}$	$-1.91 \times 10^{-6}$	0.00000	$-1.974 \times 10^{-6}$
$\gamma_1$	0.005892	0.6672	0.1191	0.2982
$\gamma_2$	0.01179	0.0000	0.01078	0.007552
$\delta$	-0.0002703	-0.0002805	-0.000245	-0.0001666
$\lambda$	-0.6070	-6.4460	-5.0350	-4.9540
$\zeta$	-0.0960	-0.2100	-0.1691	-0.1935

The model equation (12) is complex and time-consuming. Thus, it requires to be simplified for easy computation and application. For that, symbolic derivatives of equation 12 were put in MAPLE software, by producing a system of equations with the coefficients  $\beta_j$ . Then, the obtained system of equations from MAPLE software was solved iteratively in MATLAB software. The coefficients of the developed model were approximated with an error tolerance of 0.0001. The general form of the developed model for the estimation of all four types of photovoltaic (PV) module temperatures is shown in equation (13), and model coefficients are given in Table 4.

$$T_m = \alpha_0 + \beta_1(G_{sr}) + \beta_2(G_{sr})^2 + \gamma_1(T_a) + \gamma_2(T_a)^2 + \delta(G_{sr})(T_a) + \lambda(W_v) + \zeta(R_h). \quad (13)$$

where  $\alpha_0$ ,  $\beta_1$ ,  $\beta_2$ ,  $\gamma_1$ ,  $\gamma_2$ ,  $\delta$ ,  $\lambda$ , and  $\zeta$  are least squares coefficients of the proposed model.

## 5. Statistical Analysis

Statistical analysis was conducted to see the variation between models' estimated and measured results. The coefficient of determination ( $R^2$ ) [48, 49], root mean square error (RMSE), and mean absolute error (MAE) [40, 48–50] were used as statistical indicators as given in equation (14), respectively. The root mean square error (RMSE) and mean absolute error (MAE) are considered in °C. The statistical analysis was done at 95% confidence level.

$$R^2 = \frac{\sum_{i=1}^n (T_{m\_est_i} - \bar{T}_{m\_est_i})^2}{\sum_{i=1}^n (T_{m\_meas_i} - \bar{T}_{m\_meas_i})^2},$$

$$RMSE = \sqrt{\frac{\sum_{i=1}^n (T_{m\_est_i} - T_{m\_meas_i})^2}{n}}, \quad (14)$$

$$MAE = \frac{1}{n} \sum_{i=1}^n (T_{m\_est_i} - T_{m\_meas_i}).$$

where  $\bar{T}_{m\_est}$  is the average estimated module temperature and  $\bar{T}_{m\_meas}$  is the average measured module temperature.

## 6. Results and Discussion

**6.1. Weather Conditions.** The average hourly global solar radiation ( $G_{sr}$ ), maximum and minimum ambient temperature ( $T_a$ ), wind speed ( $W_v$ ), and relative humidity ( $R_h$ ) of a whole year from November, 2015, to October, 2016, are shown in Figures 4–7. The yearly average total global solar radiations were found to be 6224.35 kWh/m<sup>2</sup>/day with a maximum average of 835.25 W/m<sup>2</sup> at 12 hours and a minimum average of 86.02 W/m<sup>2</sup> at 07 hours. The values of global solar radiations are given in Figure 4. The maximum  $T_a$  was noted as 34.67°C at 15 hours and the minimum as 21.35°C at 07 hours with a yearly average of 30.11°C during the study period. The ambient temperature values are shown in Figure 5. Similarly, Figure 6 displays the wind speed. The maximum yearly average  $W_v$  was recorded as 2.60 m/s at 16 hours and the minimum as 1.30 m/s at 07 hours with a yearly average of 2.14 m/s. Likewise, the maximum yearly average  $R_h$  was noted as 76.90% at 07 hours and the minimum as 26.25% with a yearly average of 42.66%. The  $R_h$  is given in Figure 7. The yearly average values of climatic conditions like  $G_{sr}$ ,  $T_a$ ,  $W_v$ , and  $R_h$  are given in Table 5. Relative humidity was found inversely proportional to the intensity of global solar radiation and ambient temperature.

**6.2. Validation of Proposed Model Results.** The proposed model results were validated by comparing its estimations with measured data of winter season (for the months of December and January 2017) and summer season (for the months of May and June 2017) and with estimations of other existing models.

**6.3. Proposed and Existing Model Estimations versus Measured Data of Winter Season.** The comparison of the proposed model estimation versus measured and other existing model results of polycrystalline, monocrystalline, amorphous, and thin film modules are shown in Figures 8–11 for winter season, respectively. The average proposed model has estimated 0.19°C (0.61%), 0.48°C (1.61%), 0.06°C (0.19%), and 0.07°C (0.24%) low module temperatures for polycrystalline, monocrystalline, amorphous, and thin film modules, respectively, than measured ones. It was found that

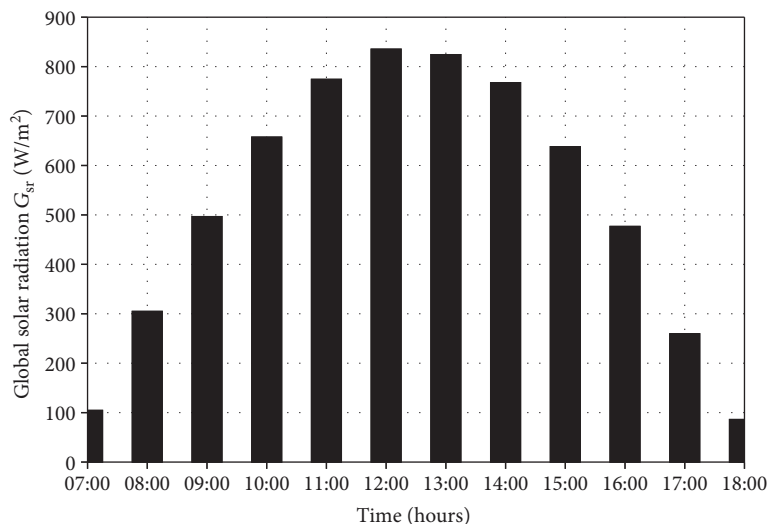


FIGURE 4: Yearly hourly average values of global solar radiation.

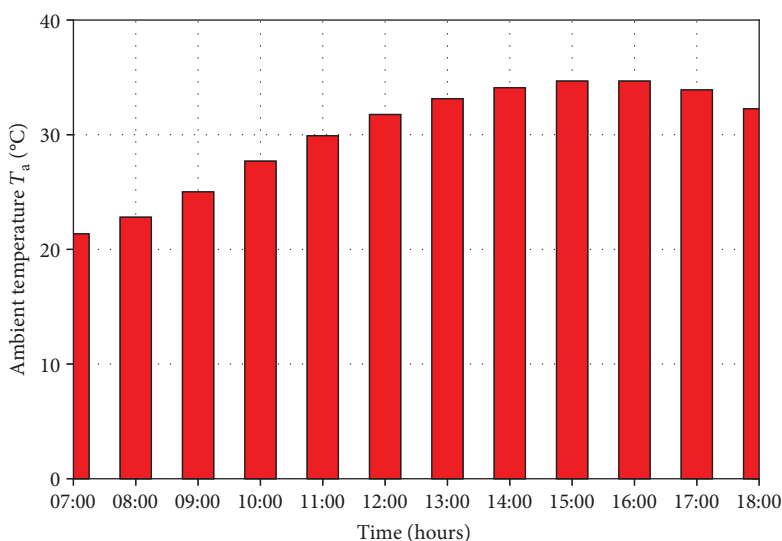


FIGURE 5: Yearly hourly average values of ambient temperature.

monocrystalline has a least percentage of module temperature than other module technologies. It was revealed that Rahman et al. [39], Muzathik [38], Skoplaki et al. [2] and Duffie and Beckman [42] models' predicted results are lower than those of the measured and proposed models' estimated module temperature because of the lower number of input parameters. Risser and Fuentes [43] and Almaktar et al. [40] models gave higher average module temperature of  $3.40^{\circ}C$  (10.91%) and  $6.32^{\circ}C$  (16.83%) for polycrystalline,  $4.61^{\circ}C$  (15.38%) and  $7.53^{\circ}C$  (25.09%) for monocrystalline,  $3.34^{\circ}C$  (10.68%) and  $6.25^{\circ}C$  (20.00%) for amorphous, and  $4.62^{\circ}C$  (15.43%) and  $7.54^{\circ}C$  (25.14%) for thin film modules, respectively, than the proposed model estimations.

**6.4. Proposed and Existing Model Estimations versus Measured Data of Summer Season.** The comparison of the proposed model estimation versus measured and other

existing model results of polycrystalline, monocrystalline, amorphous, and thin film modules are shown in Figures 12–15 for summer season, respectively. The proposed model gave  $0.43^{\circ}C$  (0.84%) higher module temperature for polycrystalline and  $1.31^{\circ}C$  (2.65%),  $0.90^{\circ}C$  (1.76%), and  $1.07^{\circ}C$  (2.15%) lower module temperature for monocrystalline, amorphous, and thin film modules than the measured module temperature. It was found that monocrystalline estimates a least percentage of module temperature than amorphous and thin film modules. It was found that Rahman et al. [39], Muzathik [38], Skoplaki et al. [2], and Duffie and Beckman [42] models' predicted results are lower than those of the measured and proposed models' estimated values. Risser and Fuentes [43] and Almaktar et al. [40] models gave higher module temperatures of  $15.79^{\circ}C$  (30.42%) and  $10.21^{\circ}C$  (19.68%) for polycrystalline,  $18.41^{\circ}C$  (37.35%) and  $12.83^{\circ}C$  (26.03%) for

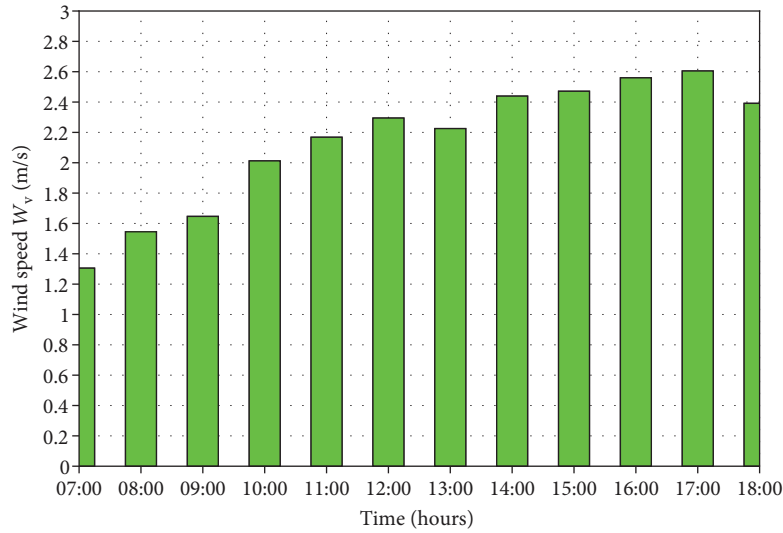


FIGURE 6: Yearly hourly average values of wind speed.

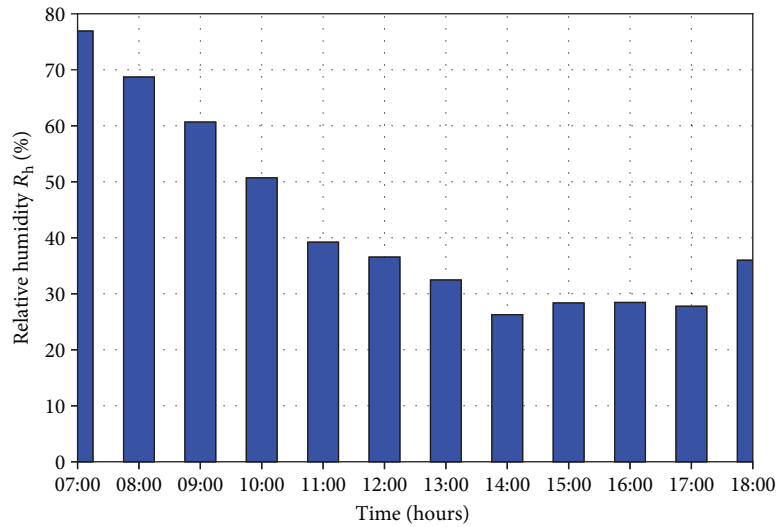


FIGURE 7: Yearly hourly average values of relative humidity.

TABLE 5: Yearly average values of climatic conditions.

	$G_{sr}$ ( $W/m^2$ )	$T_a$ ( $^{\circ}C$ )	$W_v$ (m/s)	$R_h$ (%)
Maximum values	835.25	34.67	2.60	76.90
Minimum values	86.02	21.35	1.30	26.25
Average values	518.69	30.11	2.14	42.66

monocrystalline,  $16.64^{\circ}C$  (32.60%) and  $11.07^{\circ}C$  (21.68%) for amorphous, and  $18.04^{\circ}C$  (36.32%) and  $12.46^{\circ}C$  (25.09%) for thin film modules, respectively, than the proposed model's estimated values. It was found that the proposed model estimates a low temperature with 1.61% in winter and 2.65% in summer from monocrystalline than other measured modules.

## 7. Error Analysis

The error analysis of the proposed model estimations was checked with measured data of winter season and summer season and with estimations of other existing models. The coefficient of determination ( $R^2$ ), root mean square error (RMSE) ( $^{\circ}C$ ), and mean absolute error (MAE) ( $^{\circ}C$ ) of each PV module of winter season (months of December and January) are summarized in Tables 6–8 and of the season of summer (months of May and June) in Tables 9–11, respectively.

In winter season, the maximum  $R^2$  was given by the proposed model with 0.996, 0.998, 0.992, and 0.994 and the minimum by Rahman et al. [39] model with 0.646, 0.707, 0.650, and 0.725 for polycrystalline, monocrystalline, amorphous, and thin film modules, respectively. Similarly, the minimum

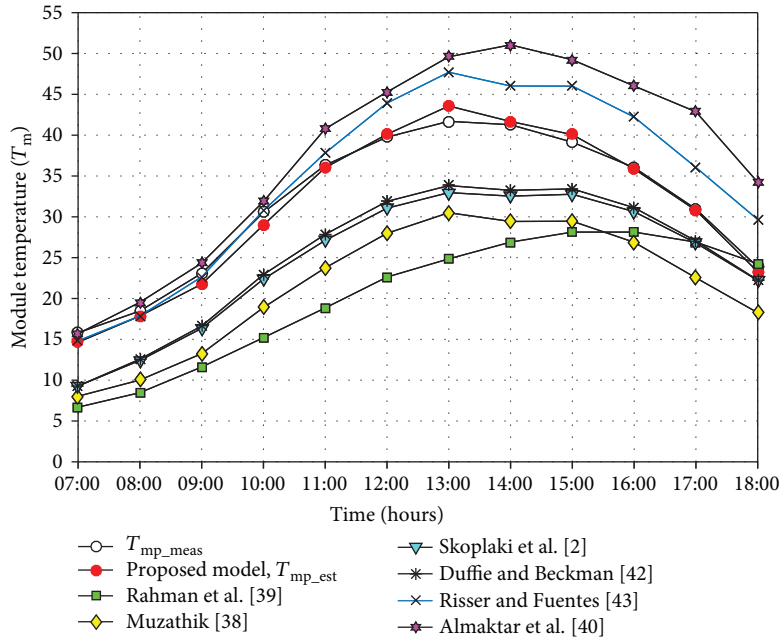


FIGURE 8: Proposed model estimation versus measured data and other existing model module temperature values of polycrystalline module during winter.

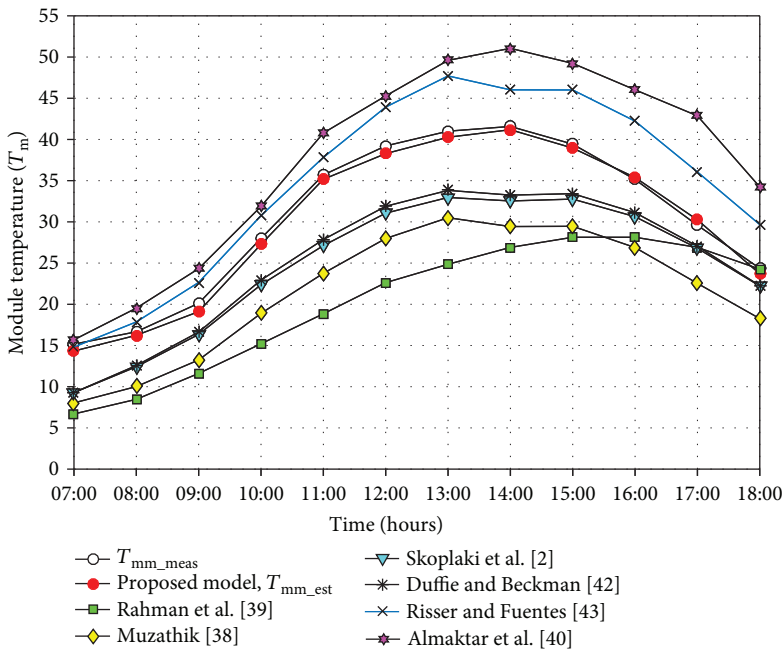


FIGURE 9: Proposed model estimation versus measured data and other existing model module temperature values of monocrystalline module during winter.

RMSE was noted by the proposed model with 0.955, 0.673, 0.898, and 0.763 and the maximum by Rahman et al. [39] model with 12.357, 11.009, 12.177, and 10.809 for polycrystalline, monocrystalline, amorphous, and thin film modules, respectively, than other existing models. Likewise, the minimum MAE was noted by the proposed model with 0.782, 0.636, 0.721, and 0.666 and the maximum by Rahman et al.

[39] model with 11.165, 9.884, 11.069, and 9.813 for polycrystalline, monocrystalline, amorphous, and thin film modules, respectively, than other existing models.

In summer season, the maximum  $R^2$  was given by the proposed model with 0.996, 0.995, 0.993, and 0.992 and the minimum by Rahman et al. [39] model with 0.496, 0.402, 0.477, and 0.456 for polycrystalline, monocrystalline,

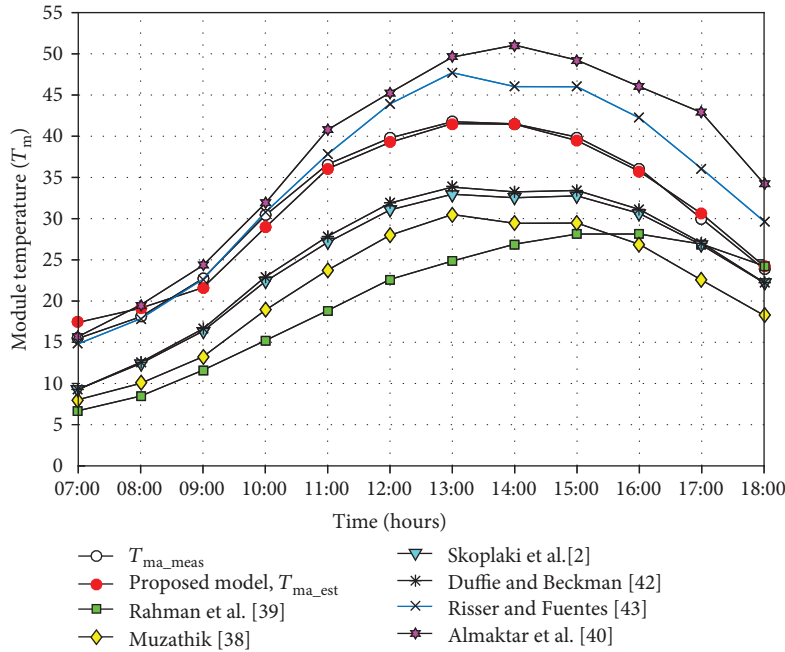


FIGURE 10: Proposed model estimation versus measured data and other existing model module temperature values of amorphous module during winter.

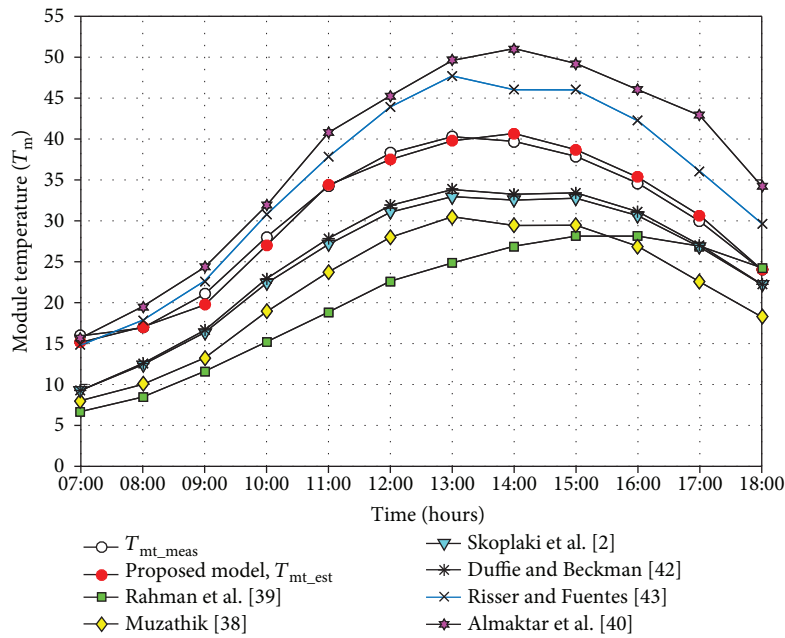


FIGURE 11: Proposed model estimation versus measured data and other existing model module temperature values of thin film module during winter.

amorphous, and thin film modules, respectively. Similarly, the minimum RMSE was noted by the proposed model with 0.996, 1.330, 1.262, and 1.502 and the maximum by Risser and Fuentes [43] model with 15.833, 18.564, 16.694, and 18.107 for polycrystalline, monocrystalline, amorphous, and thin film modules, respectively, than other existing models. Likewise, the minimum MAE was noted by the proposed

model with 0.832, 1.176, 1.078, and 1.180 and the maximum by Risser and Fuentes [43] model with 15.796, 18.413, 16.649, and 18.041 for polycrystalline, monocrystalline, amorphous, and thin film modules, respectively, than other existing models.

The proposed model gave the maximum  $R^2$  and minimum RMSE and MAE than other existing model estimations.

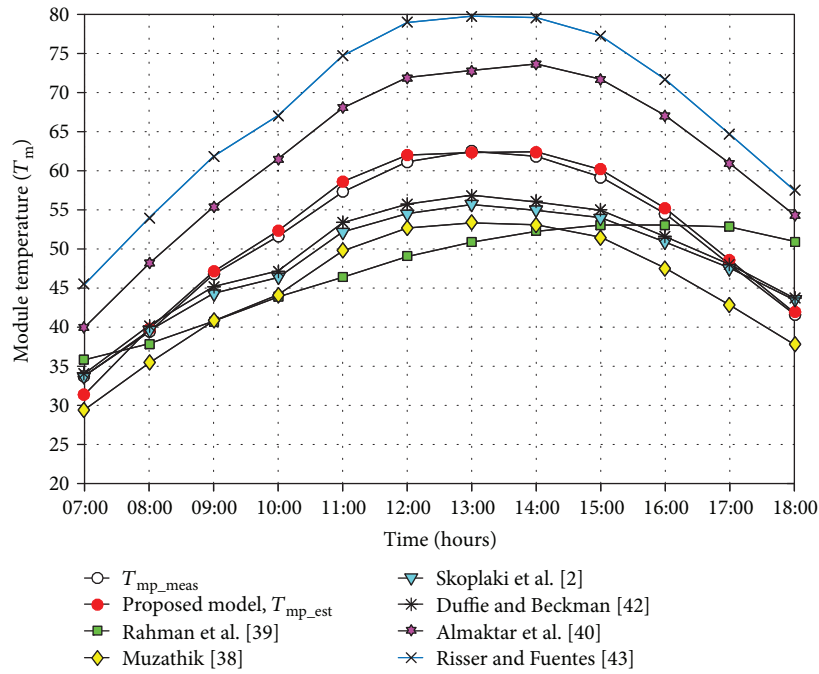


FIGURE 12: Proposed model estimation versus measured data and other existing model module temperature values of polycrystalline module during summer.

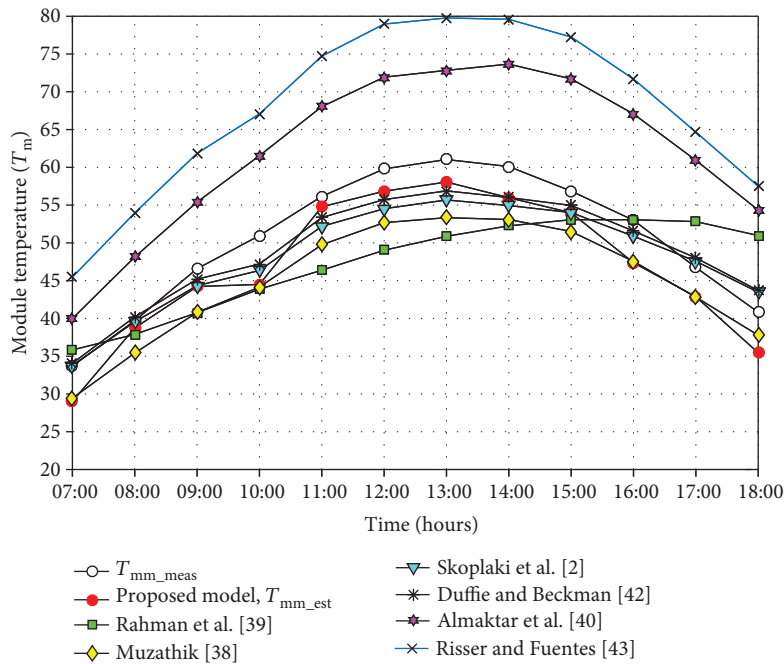


FIGURE 13: Proposed model estimation versus measured data and other existing model module temperature values of monocrystalline module during summer.

Thus, the proposed model results are more appropriate than other existing model results. It was observed that the models of one input variable show the minimum coefficient of determination and maximum root mean square error as well as the mean absolute error and vice versa for more input variable models.

### 8. Conclusions

Photovoltaic (PV) operating temperature plays an important role in the PV conversion process after solar radiation. It is a very challenging task to develop a model which represents the behaviour of various module technologies in outdoor

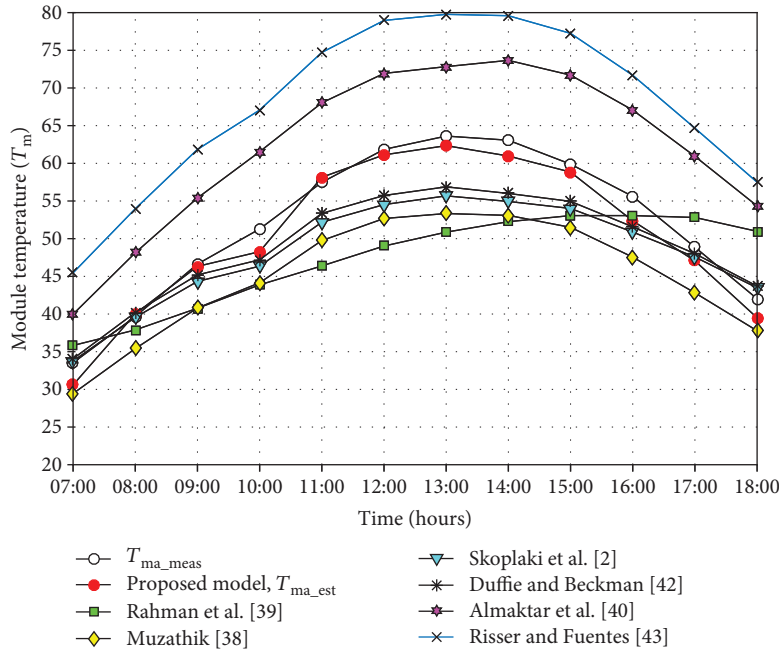


FIGURE 14: Proposed model estimation versus measured data and other existing model module temperature values of amorphous module during summer.

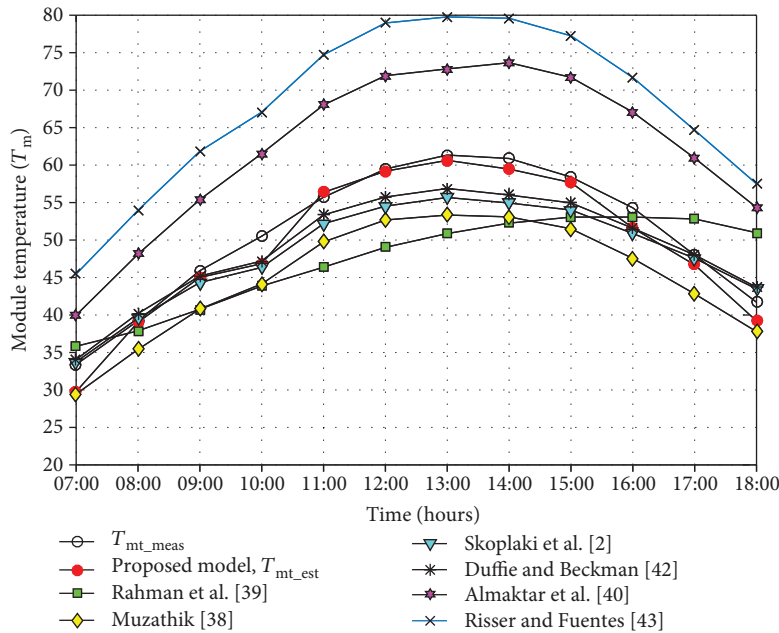


FIGURE 15: Proposed model estimation versus measured data and other existing model module temperature values of thin film module during summer.

environments. An empirical second degree polynomial multivariate model was developed using the least squares data fitting method to estimate the module temperature in outdoor conditions. It was validated by comparing the proposed model estimations with real-time measured data of winter and summer season and other existing model estimations through error analysis. It was revealed that the proposed model estimated the least temperature for

monocrystalline module with 0.48°C (1.61%) in winter season and 1.31°C (2.66%) in summer season than other examined module technologies. Risser and Fuentes [43] and Almakhtar et al. [40] models gave a higher average of module temperature with 4.62°C (15.43%) and 7.54°C (25.14%) for thin film in winter and 18.41°C (37.35%) and 12.83°C (26.03%) for monocrystalline modules in summer than the proposed model estimated values. It was found that Rahman

TABLE 6: Coefficient of determination ( $R^2$ ) of each PV module in winter.

S. no.	Name of model	Coefficient of determination ( $R^2$ )			
		(p-Si)	(m-Si)	(a-Si)	Thin film
(1)	Proposed model	0.996	0.998	0.992	0.994
(2)	Rahman et al. [39]	0.646	0.707	0.650	0.725
(3)	Muzathik [38]	0.970	0.982	0.968	0.986
(4)	Skoplaki et al. [2]	0.946	0.965	0.942	0.969
(5)	Duffie and Beckman [42]	0.955	0.970	0.949	0.974
(6)	Risser and Fuentes [43]	0.972	0.982	0.969	0.986
(7)	Almaktar et al. [40]	0.924	0.953	0.925	0.962

TABLE 7: Root mean square error (RMSE) of each PV module in winter.

S. no.	Name of model	Root mean square error (RMSE) ( $^{\circ}\text{C}$ )			
		(p-Si)	(m-Si)	(a-Si)	Thin film
(1)	Proposed model	0.955	0.673	0.898	0.763
(2)	Rahman et al. [39]	12.357	11.009	12.177	10.809
(3)	Muzathik [38]	9.935	8.678	9.854	8.560
(4)	Skoplaki et al. [2]	6.992	5.713	6.900	5.560
(5)	Duffie and Beckman [42]	6.468	5.194	6.407	5.057
(6)	Risser and Fuentes [43]	4.104	5.093	7.566	5.243
(7)	Almaktar et al. [40]	7.335	8.243	4.481	8.344

TABLE 8: Mean absolute error (MAE) of each PV module in winter.

S. no.	Name of model	Mean absolute error (MAE) ( $^{\circ}\text{C}$ )			
		(p-Si)	(m-Si)	(a-Si)	Thin film
(1)	Proposed model	0.782	0.636	0.721	0.666
(2)	Rahman et al. [39]	11.165	9.884	11.069	9.813
(3)	Muzathik [38]	9.636	8.426	9.701	8.413
(4)	Skoplaki et al. [2]	6.512	5.302	6.576	5.289
(5)	Duffie and Beckman [42]	6.047	4.838	6.112	4.825
(6)	Risser and Fuentes [43]	3.407	4.616	3.987	4.685
(7)	Almaktar et al. [40]	6.322	7.532	6.543	7.544

TABLE 9: Coefficient of determination ( $R^2$ ) of each PV module in summer.

S. no.	Name of model	Coefficient of determination ( $R^2$ )			
		(p-Si)	(m-Si)	(a-Si)	Thin film
(1)	Proposed model	0.996	0.995	0.993	0.992
(2)	Rahman et al. [39]	0.496	0.402	0.477	0.476
(3)	Muzathik [38]	0.991	0.980	0.990	0.984
(4)	Skoplaki et al. [2]	0.976	0.943	0.974	0.971
(5)	Duffie and Beckman [42]	0.983	0.955	0.983	0.979
(6)	Almaktar et al. [40]	0.982	0.946	0.973	0.974
(7)	Risser and Fuentes [43]	0.981	0.980	0.984	0.984

TABLE 10: Root mean square error (RMSE) of each PV module in summer.

S. no.	Name of model	Root mean square error (RMSE) ( $^{\circ}\text{C}$ )			
		(p-Si)	(m-Si)	(a-Si)	Thin film
(1)	Proposed model	0.996	1.330	1.262	1.502
(2)	Rahman et al. [39]	8.458	7.179	8.137	7.292
(3)	Muzathik [38]	7.444	4.790	6.665	5.234
(4)	Skoplaki et al. [2]	5.150	3.172	4.590	3.530
(5)	Duffie and Beckman [42]	4.363	2.655	3.853	2.952
(6)	Almaktar et al. [40]	10.321	13.114	11.209	12.596
(7)	Risser and Fuentes [43]	15.833	18.564	16.694	18.107

TABLE 11: Mean absolute error (MAE) of each PV module in summer.

S. no.	Name of model	Mean absolute error (MAE) ( $^{\circ}\text{C}$ )			
		(p-Si)	(m-Si)	(a-Si)	Thin film
(1)	Proposed model	0.832	1.176	1.078	1.180
(2)	Rahman et al. [39]	7.603	6.363	7.286	6.434
(3)	Muzathik [38]	7.053	4.436	6.200	4.808
(4)	Skoplaki et al. [2]	4.447	2.813	3.954	3.147
(5)	Duffie and Beckman [42]	3.799	2.239	3.334	2.646
(6)	Almaktar et al. [40]	10.218	12.835	11.071	12.463
(7)	Risser and Fuentes [43]	15.796	18.413	16.649	18.041

et al. [39] model shows the least behavior of module temperature than the measured, proposed model estimations and other existing model estimation values in both seasons. The proposed model gave around 0.998 coefficient of determination for monocrystalline and low root mean square error and mean absolute error in both seasons. It is concluded that the proposed model is more appropriate for the estimation of photovoltaic module temperature in outdoor conditions because the proposed model gave a maximum coefficient of determination and minimum root mean square error and mean absolute error in both seasons. It is recommended that the time interval of data recording may be reduced from 1 hour to minutes and PV module technologies with the same ratings may be used for a comparison purpose. The performance and effect of temperature on both free standing and building integrated systems may be checked and verified in outdoor environments.

## Nomenclature

$G_{sr}$ :	Global solar radiation ( $\text{W}/\text{m}^2$ )
$T_a$ :	Ambient temperature ( $^{\circ}\text{C}$ )
$W_v$ :	Wind speed (m/s)
$R_h$ :	Relative humidity (%)
$T_m$ :	Module temperature ( $^{\circ}\text{C}$ )
$^{\circ}\text{C}$ :	Degree centigrade
m/s:	Meter per second
%:	Percentage
PV:	Photovoltaic
p-Si:	Polycrystalline
m-Si:	Monocrystalline
a-Si:	Amorphous

$V_{oc}$ :	Open-circuit voltage (V)
$I_{sc}$ :	Short-circuit current (A)
$V_{max}$ :	Maximum voltage (V)
$I_{max}$ :	Maximum current (A)
$P_{max}$ :	Maximum power (W)
$\text{kW}/\text{m}^2$ :	Kilowatt per square meter
$\text{kWh}/\text{m}^2/\text{d}$ :	Kilowatt hour per square meter per day
$\text{W}/\text{m}^2$ :	Watt per square meter
$\text{mW}/\text{cm}^2$ :	Milliwatts per square centimeter
$T_m$ :	Module temperature ( $^{\circ}\text{C}$ )
$T_{m\_meas}$ :	Measured module temperature ( $^{\circ}\text{C}$ )
$T_{m\_est}$ :	Estimated module temperature ( $^{\circ}\text{C}$ )
$T_{mp\_meas}$ :	Polycrystalline measured module temperature ( $^{\circ}\text{C}$ )
$T_{mp\_est}$ :	Polycrystalline estimated module temperature ( $^{\circ}\text{C}$ )
$T_{mm\_meas}$ :	Monocrystalline measured module temperature ( $^{\circ}\text{C}$ )
$T_{mm\_est}$ :	Monocrystalline estimated module temperature ( $^{\circ}\text{C}$ )
$T_{ma\_meas}$ :	Amorphous measured module temperature ( $^{\circ}\text{C}$ )
$T_{ma\_est}$ :	Amorphous estimated module temperature ( $^{\circ}\text{C}$ )
$T_{mt\_meas}$ :	Thin film measured module temperature ( $^{\circ}\text{C}$ )
$T_{mt\_est}$ :	Thin film estimated module temperature ( $^{\circ}\text{C}$ )
m:	Meter
$\text{m}^2$ :	Meter square
$\eta_m$ :	Efficiency of module
$\tau_{\alpha}$ :	Transmittance of glass
$k_r$ :	Ross coefficient
$R^2$ :	Coefficient of determination
RMSE:	Root mean square error ( $^{\circ}\text{C}$ )
MAE:	Mean absolute error ( $^{\circ}\text{C}$ )

SUN: Sanak SK Union  
 TPS: Topray Solar, Shenzhen  
 NOCT: Nominal operating cell temperature  
 STC: Standard test conditions  
 QUEST: Quaid-e-Awam University of Engineering,  
 Science and Technology

#### Proposed model coefficient

$\alpha_0$ : Alpha<sub>0</sub> (general coefficients)  
 $\beta_1$ : Global solar radiation ( $G_{sr}$ )  
 $\beta_2$ : Global solar radiation ( $G_{sr}^2$ )  
 $\gamma_1$ : Ambient temperature ( $T_a$ )  
 $\gamma_2$ : Ambient temperature ( $T_a^2$ )  
 $\delta$ : Global solar radiation and ambient temperature  
 ( $G_{sr} * T_a$ )  
 $\lambda$ : Wind speed ( $W_v$ )  
 $\xi$ : Relative humidity ( $R_h$ ).

#### Data Availability

The data used to support the findings of this study are available from the corresponding author upon request.

#### Conflicts of Interest

The authors have no conflict of interest.

#### Authors' Contributions

The authors have worked and contributed equally to this paper. The research article is submitted with the approval of all authors.

#### Acknowledgments

The authors acknowledge the financial support provided by the Quaid-e-Awam University of Engineering, Science and Technology (QUEST), Nawabshah (QUEST NO. 15).

#### References

- [1] A. Rouholamini, H. Pourgharibshahi, R. Fadaeinedjad, and M. Abdolzadeh, "Temperature of a photovoltaic module under the influence of different environmental conditions – experimental investigation," *International Journal of Ambient Energy*, vol. 37, no. 3, pp. 266–272, 2016.
- [2] E. Skoplaki, A. G. Boudouvis, and J. A. Palyvos, "A simple correlation for the operating temperature of photovoltaic modules of arbitrary mounting," *Solar Energy Materials and Solar Cells*, vol. 92, no. 11, pp. 1393–1402, 2008.
- [3] V. Sharma and S. S. Chandel, "Performance and degradation analysis for long term reliability of solar photovoltaic systems: a review," *Renewable and Sustainable Energy Reviews*, vol. 27, pp. 753–767, 2013.
- [4] A. Q. Jakhrani, A. K. Othman, A. R. H. Rigit, and S. R. Samo, "Comparison of solar photovoltaic module temperature models," *World Applied Sciences Journal*, vol. 14, no. 3, pp. 1–8, 2011.
- [5] E. Barykina and A. Hammer, "Modeling of photovoltaic module temperature using Faïman model: sensitivity analysis for different climates," *Solar Energy*, vol. 146, pp. 401–416, 2017.
- [6] M. E. Meral and F. Dincer, "A review of the factors affecting operation and efficiency of photovoltaic based electricity generation systems," *Renewable and Sustainable Energy Reviews*, vol. 15, no. 5, pp. 2176–2184, 2011.
- [7] A. Luketa-Hanlin and J. Stein, *Improvement and validation of a transient model to predict photovoltaic module temperature*, no. SAND2012-4307C, 2012Sandia National Laboratories, 2012.
- [8] I. Marinić-Kragić, S. Nižetić, F. Grubišić-Čabo, and A. M. Papadopoulos, "Analysis of flow separation effect in the case of the free-standing photovoltaic panel exposed to various operating conditions," *Journal of Cleaner Production*, vol. 174, pp. 53–64, 2018.
- [9] A. Q. Jakhrani, A. K. Othman, A. R. H. Rigit, and S. R. Samo, "Determination and comparison of different photovoltaic module temperature models for Kuching, Sarawak," in *2011 IEEE Conference on Clean Energy and Technology (CET)*, pp. 231–236, Kuala Lumpur, Malaysia, June 2011.
- [10] Y. Lee and A. A. O. Tay, "Finite element thermal analysis of a solar photovoltaic module," *Energy Procedia*, vol. 15, pp. 413–420, 2012.
- [11] E. Skoplaki and J. A. Palyvos, "On the temperature dependence of photovoltaic module electrical performance: a review of efficiency/power correlations," *Solar Energy*, vol. 83, no. 5, pp. 614–624, 2009.
- [12] H. Yan, X. Wang, M. Yao, and X. Yao, "Band structure design of semiconductors for enhanced photocatalytic activity: the case of TiO<sub>2</sub>," *Progress in Natural Science: Materials International*, vol. 23, no. 4, pp. 402–407, 2013.
- [13] S. A. Kalogirou, *Solar Energy Engineering: Processes and Systems*, Academic Press Elsevier, USA, 2nd Edition edition, 2014.
- [14] A. R. Jatoi, S. R. Samo, and A. Q. Jakhrani, "Influence of temperature on electrical characteristics of different photovoltaic module technologies," *International Journal of Renewable Energy Development*, vol. 7, no. 2, pp. 85–91, 2018.
- [15] A. Q. Jakhrani, A. K. Othman, A. R. H. Rigit, R. Bainsi, S. R. Samo, and L. P. Ling, *Investigation of solar photovoltaic module power output by various models*, NED University Journal of Research, Thematic Issue on Energy, 2012.
- [16] S. N. Sharan, S. S. Mathur, and T. C. Kandpal, "Analytical performance evaluation of combined photovoltaic-thermal concentrator-receiver systems with linear absorbers," *Energy Conversion and Management*, vol. 27, no. 4, pp. 361–365, 1987.
- [17] B. Sandnes and J. Rekstad, "A photovoltaic/thermal (PV/T) collector with a polymer absorber plate: experimental study and analytical model," *Solar Energy*, vol. 72, no. 1, pp. 63–73, 2002.
- [18] T. T. Chow, "Performance analysis of photovoltaic-thermal collector by explicit dynamic model," *Solar Energy*, vol. 75, no. 2, pp. 143–152, 2003.
- [19] E. Skoplaki and J. A. Palyvos, "Operating temperature of photovoltaic modules: a survey of pertinent correlations," *Renewable Energy*, vol. 34, no. 1, pp. 23–29, 2009.
- [20] A. Q. Jakhrani, S. R. Samo, S. A. Kamboh, J. Labadin, and A. R. H. Rigit, "An improved mathematical model for computing power output of solar photovoltaic modules," *International Journal of Photoenergy*, vol. 2014, Article ID 346704, 9 pages, 2014.

- [21] C. Cancro, S. Ferlito, and G. Graditi, "Forecasting the working temperature of a concentrator photovoltaic module by using artificial neural network-based model," in *AIP Conference Proceedings*, vol. 1766no. 1, pp. 090004–090007, Freiburg, Germany, 2016.
- [22] S. Pindado, J. Cubas, E. Roibás-Millán, F. Bugallo-Siegel, and F. Sorribes-Palmer, "Assessment of explicit models for different photovoltaic technologies," *Energies*, vol. 11, no. 6, article 1353, 2018.
- [23] M. Mattei, G. Notton, C. Cristofari, M. Muselli, and P. Poggi, "Calculation of the polycrystalline PV module temperature using a simple method of energy balance," *Renewable Energy*, vol. 31, no. 4, pp. 553–567, 2006.
- [24] D. Faiman, "Assessing the outdoor operating temperature of photovoltaic modules," *Progress in Photovoltaics: Research and Applications*, vol. 16, no. 4, pp. 307–315, 2008.
- [25] I. Santiago, D. Trillo-Montero, I. M. Moreno-Garcia, V. Pallarés-López, and J. J. Luna-Rodríguez, "Modeling of photovoltaic cell temperature losses: a review and a practice case in South Spain," *Renewable and Sustainable Energy Reviews*, vol. 90, pp. 70–89, 2018.
- [26] A. D. Jones and C. P. Underwood, "A thermal model for photovoltaic systems," *Solar Energy*, vol. 70, no. 4, pp. 349–359, 2001.
- [27] S. Armstrong and W. G. Hurley, "A thermal model for photovoltaic panels under varying atmospheric conditions," *Applied Thermal Engineering*, vol. 30, no. 11–12, pp. 1488–1495, 2010.
- [28] D. Torres Lobera and S. Valkealahti, "Dynamic thermal model of solar PV systems under varying climatic conditions," *Solar Energy*, vol. 93, pp. 183–194, 2013.
- [29] A. Q. Jakhriani, A. K. Othman, A. R. H. Rigit, S. R. Samo, and S. A. Kamboh, "A novel analytical model for optimal sizing of standalone photovoltaic systems," *Energy*, vol. 46, no. 1, pp. 675–682, 2012.
- [30] M. Almakhtar, H. Abdul Rahman, M. Y. Hassan, and I. Saeh, "Artificial neural network-based photovoltaic module temperature estimation for tropical climate of Malaysia and its impact on photovoltaic system energy yield," *Progress in Photovoltaics: Research and Applications*, vol. 23, no. 3, pp. 302–318, 2015.
- [31] A. Teke, H. B. Yildirim, and Ö. Çelik, "Evaluation and performance comparison of different models for the estimation of solar radiation," *Renewable and Sustainable Energy Reviews*, vol. 50, pp. 1097–1107, 2015.
- [32] W. Zhou, C. Lou, Z. Li, L. Lu, and H. Yang, "Current status of research on optimum sizing of stand-alone hybrid solar-wind power generation systems," *Applied Energy*, vol. 87, no. 2, pp. 380–389, 2010.
- [33] M. I. Al-Najideen and S. S. Alrwashdeh, "Design of a solar photovoltaic system to cover the electricity demand for the faculty of Engineering-Mu'tah University in Jordan," *Resource-Efficient Technologies*, vol. 3, no. 4, pp. 440–445, 2017.
- [34] S. Alsadi and T. Khatib, "Photovoltaic power systems optimization research status: a review of criteria, constraints, models, techniques, and software tools," *Applied Sciences*, vol. 8, no. 10, article 1761, 2018.
- [35] M. A. Ahmed, F. Ahmed, and A. W. Akhtar, "Distribution of total and diffuse solar radiation at Lahore, Pakistan," *Journal of Scientific Research*, vol. 40, no. 1, pp. 37–43, 2010.
- [36] J. S. Stein, C. P. Cameron, B. Bourne, A. Kimber, J. Posbic, and T. Jester, "A standardized approach to PV system performance model validation," in *2010 35th IEEE Photovoltaic Specialists Conference*, pp. 001079–001084, Honolulu, HI, USA, June 2010.
- [37] M. B. Ammar, M. Chaabene, and Z. Chtourou, "Artificial neural network based control for PV/T panel to track optimum thermal and electrical power," *Energy Conversion and Management*, vol. 65, pp. 372–380, 2013.
- [38] M. A. Muzathik, "Photovoltaic modules operating temperature estimation using a simple correlation," *International Journal of Energy Engineering*, vol. 4, no. 4, pp. 151–158, 2014.
- [39] H. A. Rahman, K. M. Nor, M. Y. Hassan, and M. S. Majid, "Empirical models for the correlation of global solar radiation under Malaysia environment," *International Review on Modelling and Simulations*, vol. 4, no. 4, pp. 1864–1870, 2011.
- [40] M. Almakhtar, H. A. Rahman, M. Y. Hassan, and S. Rahman, "Climate-based empirical model for PV module temperature estimation in tropical environment," *Applied Solar Energy*, vol. 49, no. 4, pp. 192–201, 2013.
- [41] C. Coskun, U. Toygar, O. Sarpdag, and Z. Oktay, "Sensitivity analysis of implicit correlations for photovoltaic module temperature: a review," *Journal of Cleaner Production*, vol. 164, pp. 1474–1485, 2017.
- [42] J. A. Duffie and W. A. Beckman, *Solar Engineering of Thermal Processes*, John Wiley & Sons, Inc., Hoboken, New Jersey, 3rd Edition edition, 2006.
- [43] V. V. Risser and M. K. Fuentes, "Linear regression analysis of flat-plate photovoltaic system performance data," in *5th Photovoltaic Solar Energy Conference*, pp. 623–627, Athens, Greece, 1984.
- [44] A. Soomro, S. R. Samo, A. R. Jatoy, and A. Q. Jakhriani, "Energy conservation in office building by utilization of daylighting," *International Journal of Natural and Engineering Sciences*, vol. 10, no. 1, pp. 1–6, 2016.
- [45] W. Ahmad, A. Fatima, U. K. Awan, and A. Anwar, "Analysis of long term meteorological trends in the middle and lower Indus Basin of Pakistan—a non-parametric statistical approach," *Global and Planetary Change*, vol. 122, pp. 282–291, 2014.
- [46] A. R. Jatoy, S. R. Samo, and A. Q. Jakhriani, "Influence of ambient temperature and solar radiations on photovoltaic module's temperature and power output," *International Journal of Natural and Engineering Sciences*, vol. 10, no. 2, pp. 43–47, 2016.
- [47] B. J. Huang, P. E. Yang, Y. P. Lin et al., "Solar cell junction temperature measurement of PV module," *Solar Energy*, vol. 85, no. 2, pp. 388–392, 2011.
- [48] A. Massi Pavan, A. Mellit, and V. Lughi, "Explicit empirical model for general photovoltaic devices: experimental validation at maximum power point," *Solar Energy*, vol. 101, pp. 105–116, 2014.
- [49] R. C. Deo and M. Şahin, "Application of the artificial neural network model for prediction of monthly standardized precipitation and evapotranspiration index using hydrometeorological parameters and climate indices in eastern Australia," *Atmospheric Research*, vol. 161–162, pp. 65–81, 2015.
- [50] N. Savvakis and T. Tsoutsos, "Performance assessment of a thin film photovoltaic system under actual Mediterranean climate conditions in the island of Crete," *Energy*, vol. 90, pp. 1435–1455, 2015.

## Research Article

# Design and Dynamic Modelling of a Hybrid Power System for a House in Nigeria

Lawrence O. Aghenta  and M. Tariq Iqbal 

*Electrical and Computer Engineering Department, Faculty of Engineering and Applied Science, Memorial University of Newfoundland, St. John's, NL, Canada*

Correspondence should be addressed to Lawrence O. Aghenta; loaghenta@mun.ca

Received 26 October 2018; Revised 27 December 2018; Accepted 19 January 2019; Published 30 April 2019

Guest Editor: Paolo Conti

Copyright © 2019 Lawrence O. Aghenta and M. Tariq Iqbal. This is an open access article distributed under the Creative Commons Attribution License, which permits unrestricted use, distribution, and reproduction in any medium, provided the original work is properly cited.

This paper presents the design and dynamic modelling of a hybrid power system for a house in Nigeria. Thermal modelling of the house under consideration is carried out using BEopt software to accurately study the heat loss through the walls, windows, doors, and roof of the house. The analysis of this thermal model is used to determine hourly load data. Design of an optimum hybrid power system for the house is done with HOMER Pro software. The hybrid power system is made up of a diesel generator and a stand-alone PV system. The proposed PV system consists of PV arrays, DC–DC boost converter, MPPT controller, single-phase full-bridge inverter, inverter voltage mode controller (PI controller), and single-phase step-up transformer. Dynamic simulation of the proposed PV system component of the hybrid power system is carried out in MATLAB/Simulink environment to study the power quality, harmonics, load impact, voltage transients, etc. of the system, and the simulation results are presented in the paper.

## 1. Introduction

Electricity is one of the basic amenities of man because of its wide usage in various aspects of life. Thus, the need for a reliable source of power supply cannot be over emphasized. Unfortunately, electrical power supply in developing countries like Nigeria is unreliable, thereby making life difficult. Nigeria is a federal republic in West Africa, bordering Benin in the west, Chad and Cameroon in the east, and Niger in the north. Its coast in the south lies on the Gulf of Guinea in the Atlantic Ocean. It comprises 36 states and the Federal Capital Territory, where the capital, Abuja, is located [1]. Nigeria is often referred to as the “Giant of Africa,” owing to its large population and economy. With 186 million inhabitants, Nigeria is the most populous country in Africa and the seventh most populous country in the world [1]. Nigeria is the 12th largest producer of petroleum in the world, and the 8th largest exporter, and has the 10th largest proven reserves. Apart from petroleum, Nigeria is also blessed with other natural resources including natural gas, tin, iron ore, coal, limestone, niobium, lead, zinc, and arable land. Despite these

abundant natural resources, the country is unable to generate enough electricity to support the national population. Presently, the amount of generated power is about 9 percent of the required power needed to completely electrify the country (about 80,000 MW capacity is required but barely 7,445 MW is installed) [2]; thus, the country continues to experience extreme electricity shortage and prolonged periods of power outages such that a typical Nigerian household has electric power supply for 5 hours a day on the average. Over the years, households have had to rely mostly on private power generators to meet their electricity needs. However, the growing price of petroleum products to power these generators is a major concern for the average household. Also, the noise and fumes from these generators are having significant impacts on the environment as the fumes continue to contribute to the carbon footprints of the houses. To avoid these negative environmental impacts of fossil fuel usage, it is important to find ways to economically utilize clean and sustainable sources of energy such as wind and solar energies to meet the electricity needs of the house. Various literatures presented in [3] have reported abundant

solar resource potential of between 3.5 kWh/m<sup>2</sup>/day and 7.0 kWh/m<sup>2</sup>/day across Nigeria and average sunshine duration of 6.25 hours per day. This is corroborated by the April 2018 weekly agrometeorological data for the dekad bulletin of the Nigerian Meteorological Agency (NiMet) [4], which shows an average solar irradiation for a northern city like Zaria to be 23.4 MJ/m<sup>2</sup>/day (6.5 kWh/m<sup>2</sup>/day) and that for a southern city like Benin City to be 17.3 MJ/m<sup>2</sup>/day (4.81 kWh/m<sup>2</sup>/day). Despite these large solar resources, Nigeria is yet to fully integrate solar energy into its energy generation mix.

## 2. Literature Review

Individuals and researchers across Nigeria have over the years taken advantage of the availability of abundant solar resources and its ease of use to design photovoltaic (PV) systems to meet their private energy needs. Udoakah et al. [5] designed a 1 kVA PV system for electrical laboratory in the Faculty of Engineering at the University of Uyo to solve the problem of sudden power failures during laboratory sessions. The major components of their off-grid PV system design include two 150 W solar panels connected in parallel (PV module), an inverter unit, one 12 V, 100 AH deep cycle battery, charge controller unit, and an automatic control unit to automatically switch from the inverter to the public power supply whenever the public power was available and vice versa. Elsewhere, Okoye et al. [3] proposed a stand-alone solar PV system design solution and cost model analysis using both intuitive and numerical methods. The authors considered constant electrical load demands of a house each in three different major cities in Nigeria: Onitsha, located in the southeast region; Kano, located in northwest region; and Lagos, located in the southwest region as case studies using the 2016 meteorological solar radiation data sets for these cities in their analysis. In their solution, they used intuitive and numerical methods to calculate the required PV area and capacity, the number of PV modules, the corresponding capacities of the battery, the inverter, and the charge controller while using the life cycle cost analysis model to investigate the optimal cost solution for the PV system design which takes into account the initial capital investment, the present cost of the battery, the inverter, the charge controller, and the balance of system cost to estimate the net present value of the PV system as well as the estimated future value of the system using appropriate discount rates for each of the components of the PV system. Akinyele and Rayudu [6] proposed an off-grid PV system design solution to solve electrical power problems in two rural households in Nigeria using HOMER software for the modelling and analysis of the PV system and cost. In their research, they considered energy consumption scenarios of two households in Agwandodo settlement in Gwagwalada, Abuja, with moderate loads. Considering the average loads and operating hours of the domestic appliances for each of these houses, they used both MATLAB and HOMER tools to obtain the daily load profiles for the two houses. They then used HOMER software to

obtain the optimized component sizes of the stand-alone PV systems for the houses and costs.

In yet another development, Adaramola et al. [7] presented the feasibility analysis of hybrid PV solar-diesel power system application for the remote areas in the northern part of Nigeria using Jos and its environs in Plateau State as a case study. In their solution, electrical energy of 1.5 MWh per day with daily peak load of 236 kW was simulated for rural areas with a population of about 1,500 households and with the assumption that each household consumed 1 kWh of energy per day. The values were then used to determine the ratings of the other components of the proposed hybrid PV solar-diesel system including PV modules, diesel generator, battery, and power converter.

In most of the above mentioned papers, the energy requirements for their hybrid/PV system design have been estimated by calculating the power requirement of each device in the house and estimating the approximate number of hours each device would utilize power in a day. The problem with this method of estimating energy needs for PV system design is that it does not consider the type and size of the locations of electrical appliances, the building materials, orientation and dimensions of the house, and heat loss through the walls, windows, doors, and roofs of the house. Also, the intuitive and numerical methods of estimating energy requirements presented in the other papers above have some drawbacks. Although the intuitive methodology is relatively simple to compute compared to the numerical method, it has the drawback of often over sizing or under sizing the entire system due to not modelling the interactions among the subsystem components [3]. The numerical method, on the other hand, is a complex solution prone to errors as it involves a lot of parameter estimations.

In this paper, the enumerated shortcomings above are addressed in designing a hybrid power system. This paper involves three major tasks. Firstly, a detailed thermal modelling of the chosen house using BEopt software is completed. Secondly, optimum hybrid power system design using HOMER Pro software is presented. Finally, MATLAB/Simulink dynamic simulation of the optimum PV system component of the proposed hybrid power system is presented along with the simulation results. Specifically, the contributions of this study include the following:

- (i) Thermal modelling of the house, taking into account important parameters such as the type and size of the house, location and orientation of the house, materials used in building the house, number and types of appliances in the house, and number of occupants, as well as heat loss through the walls and windows. Such modelling resulted in a detailed hourly and annual load profile of the house. This, to the best of the authors' knowledge from reviewed literatures, has never been done for the determination of load profiles in that region
- (ii) Determination of the optimal renewable energy mix and conventional diesel generator size of the hybrid power system for the specific house in Nigeria



FIGURE 1: House side view.



FIGURE 2: BEopt software house design.

- (iii) Assessment of the optimal system configuration to achieve energy independence for the house
- (iv) MATLAB/Simulink dynamic simulation of the PV system component of the proposed hybrid power system to study the power quality, harmonics, load impact, and voltage transients under various conditions specific to the house under consideration

### 3. Thermal Modelling of the House in BEopt

In order to design a hybrid power system for a household, it is important to accurately determine the energy needs of the household for which the system is being designed. This can be achieved through thermal modelling of the house [8]. Building energy optimization (BEopt) software, developed by the National Renewable Energy Laboratory, provides capabilities to evaluate residential building designs and identify cost-optimal solution at various levels of whole-house energy savings along the path to zero net energy [8, 9]. It provides detailed simulation-based analysis based on specific house characteristics, such as size, architecture, occupancy, vintage, location, and utility rates. BEopt can be used to analyze both new construction and existing home retrofits, as well as single-family detached and multifamily buildings, through evaluation of single building designs, parametric sweeps, and cost-based optimizations [9]. The chosen house is located in Benin City (latitude 6°20'0" N and longitude 5°38'0" E), Edo State, Nigeria. It is a south-facing bungalow building with a total area of 2,375 sqft, one front door and one back door, one big living room, five bedrooms, three bathrooms, one kitchen, windows of various sizes, corridors, concrete walls, ceilings, and aluminum roofs. The side view of the house is shown in Figure 1. Using the specific parameters of the house for BEopt thermal modelling and

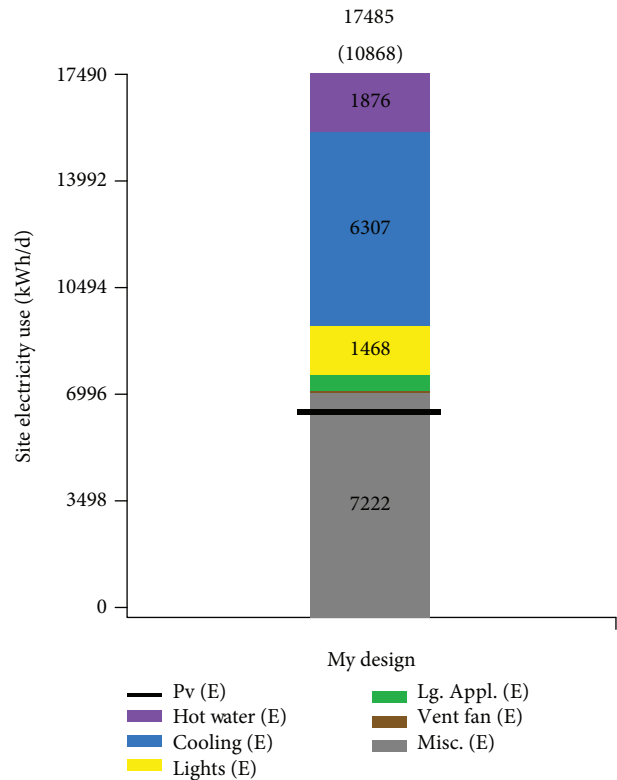


FIGURE 3: House annual energy consumption from BEopt simulation.

simulations (Figure 2), the house was found to require an annual energy consumption of 17,485 kWh/year (about 2 kW average load) as shown in Figure 3. The generated daily, monthly, and yearly load profiles of the house are shown in Figure 4. However, the PV system component of the hybrid power system is designed for a load of 1.5 kW with the assumption that the extra refrigerators and heavy air conditioners included in BEopt simulation will be removed before switching to the PV system.

### 4. Optimum Hybrid Power System Design with HOMER Pro

A hybrid power system is made up of various components. In designing a hybrid power system, factors such as the size of the components, system configurations, adequacies of the various renewable energy resources in that region, project economics with changing loads and component costs, life cycle of the system, net present cost of the system, cost of energy to the end user, maintenance costs, and annual operating costs of the hybrid system will help the decision-maker to determine the most cost-effective solutions of the hybrid system to meet the electrical loads for which it is being designed [10]. Hybrid Optimization of Multiple Energy Resources (HOMER) software, developed by the National Renewable Energy Laboratory, models micropower systems with single or multiple power sources (e.g., photovoltaics and wind turbines), and helps to design off-grid and grid-connected systems in the most cost-effective ways by taking the factors above into consideration [10, 11]. It simulates

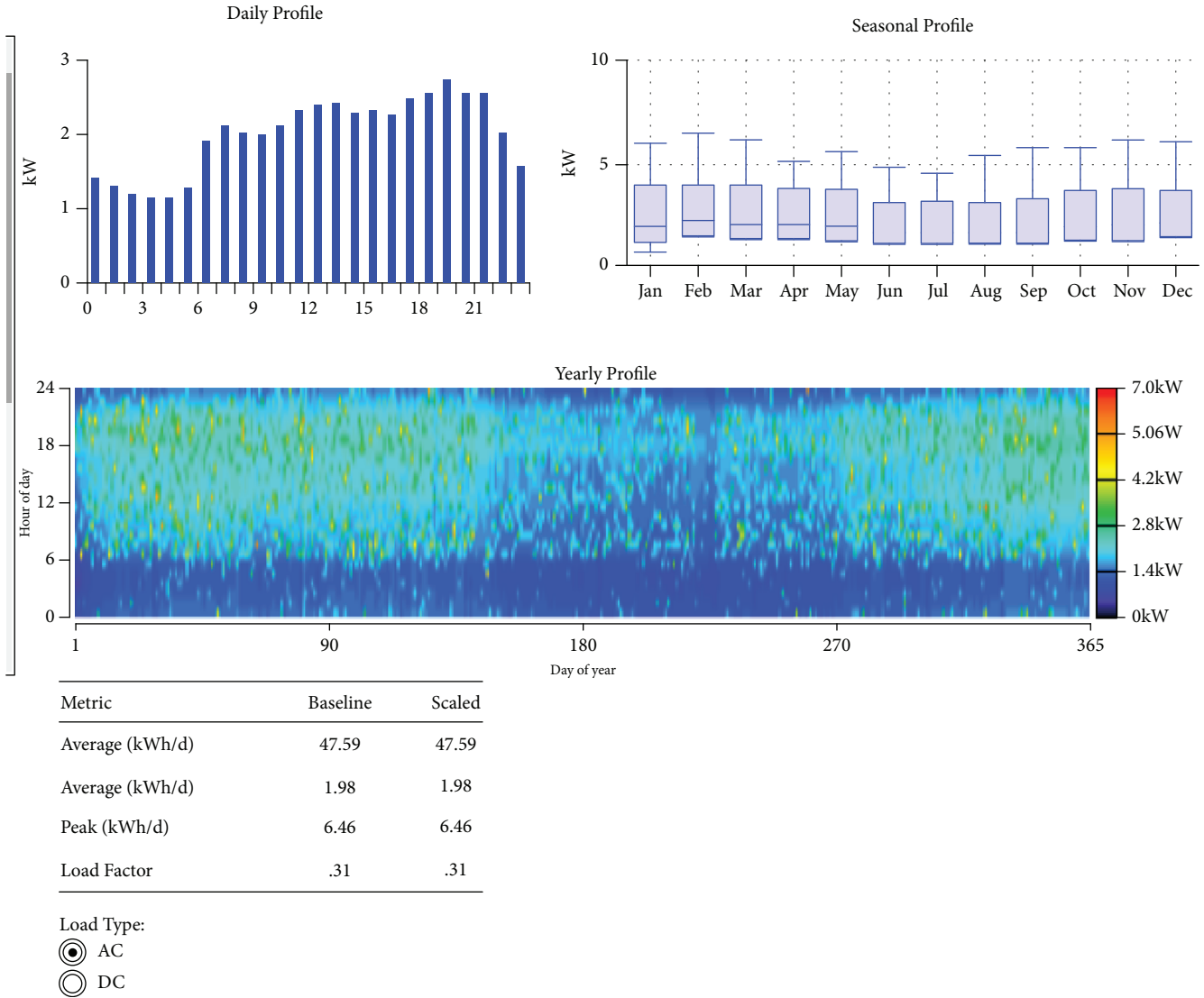


FIGURE 4: Daily, monthly, and annual load profile of the house from BEopt simulation.

various configurations to find the least-cost combinations that meet the electrical loads being considered. HOMER’s optimization and sensitivity analysis capabilities help to answer important design questions such as “Which technologies are most cost-effective? What size should components be? What happens to the project’s economics if costs or loads change? Is the renewable energy resource adequate?” [11]. From the house thermal model with BEopt software, the generated annual hourly load data (Figure 4) for the house was exported into HOMER Pro software for generator/PV system sizing and optimum hybrid power system design. The simulation was done using the solar irradiation data of the house location (Figure 5), actual PV modules, converters, and batteries, and the optimized hybrid power system configuration is shown in Figure 6. Figure 7 shows a HOMER-optimized hybrid power system design based on the technical and economic data available. Such a system, designed for 25 years life cycle, will have a total net present cost (NPC) of USD 106,307.90, a levelized cost of energy (CoE) of USD 0.4734

per kWh, and an annual operating cost of USD 5,650.04. The system will also have an excess energy of 14.9 percent which can be used to power the bulbs outside the fence of the house. The diesel generator will help to provide backup power during prolonged extreme weather conditions when the primary battery backup power from the PV system is unavailable. The rest of this paper is dedicated to the design and dynamic modelling of the proposed PV system component in the optimal hybrid power system.

### 5. The Proposed PV System Components

The proposed PV system is a stand-alone PV system comprising of PV arrays, DC-DC boost converter, MPPT controller, battery bank, DC-AC converter (inverter), inverter voltage mode controller, single-phase step-up transformer, and the single-phase AC loads of the house under consideration. Figure 8 shows a block diagram of the proposed PV system.

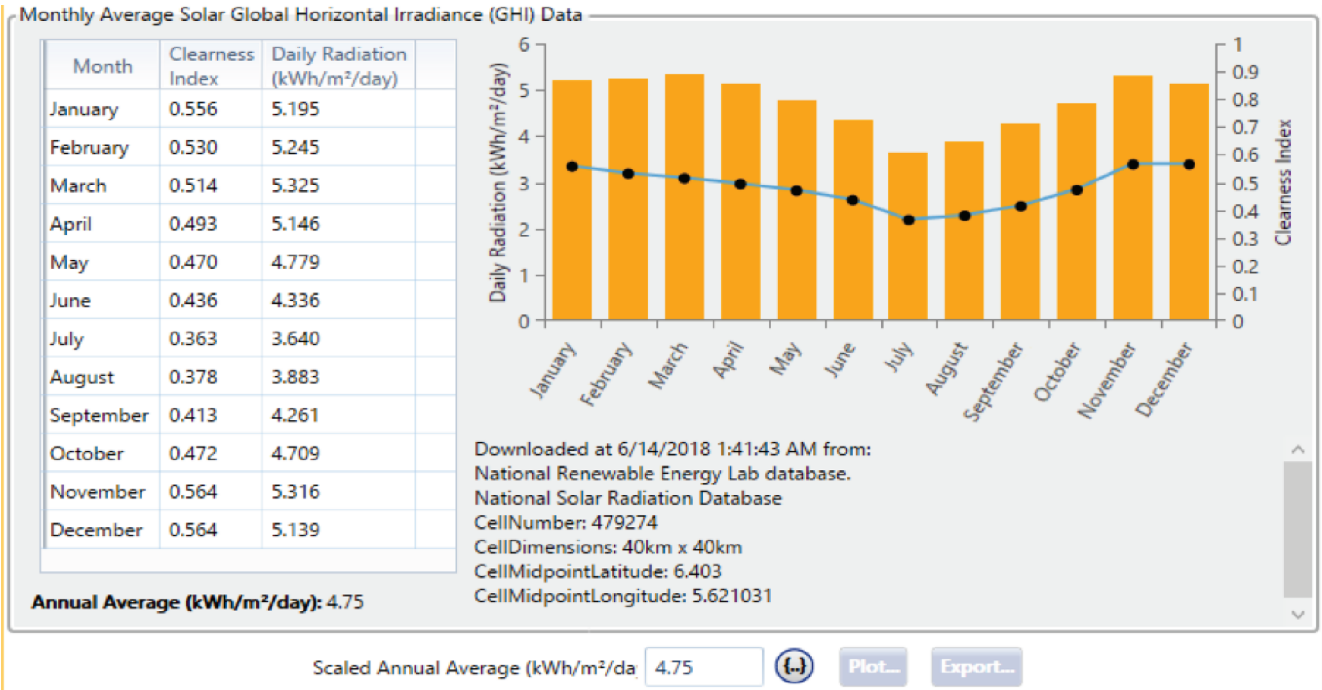


FIGURE 5: Downloaded solar irradiance of the house location.

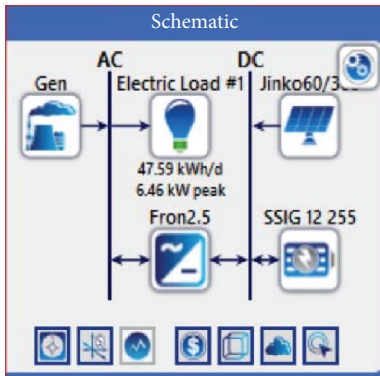


FIGURE 6: HOMER-optimized hybrid power system configuration.

5.1. PV Arrays. Photovoltaics (PV) are used to convert sunlight directly into electricity [12, 13]. A solar cell is a PN junction diode with current flowing in the reverse direction. A number of solar cells make up PV modules. PV array consists of strings of modules connected in parallel, each string consisting of modules connected in series [13]. Temperature and irradiation level are the two main factors that affect PV array outputs. Change in temperature and irradiation level results in change in voltage and current, as well as power generated by PV systems [14]. Figure 9 shows a solar cell model using a current source  $I_L$  (light-generated current), diode ( $I_0$  and  $nI$  parameters), series resistance  $R_s$ , and shunt resistance  $R_{sh}$  to represent the irradiance and temperature-dependent I-V characteristics [14]. The diode I-V characteristics for a single module are defined by equations (1) and (2) below [14]. The PV array used for this project is the Jinko Solar

JMK300M-72 PV array manufactured by Jinko Solar. The array comprises of 4 strings of 12 panels of PV modules to give an output power of maximum 14.4kW ( $12 \times 4 \times 300 = 14.4$  kW). The I-V and P-V characteristics of the PV array at various temperature and irradiation levels are shown in Figure 10.

$$I_d = I_0 \left[ \exp \left( \frac{V_d}{V_T} \right) - 1 \right], \quad (1)$$

$$V_T = \frac{KT}{q} \times nl \times N_{cell}, \quad (2)$$

where  $I_d$  is the diode current (A),  $V_d$  is the diode voltage (V),  $I_0$  is the diode saturation current (A),  $nl$  is the diode ideality factor, a number close to 1.0,  $K$  is the Boltzman constant =  $1.3806e-23$  J.K-1,  $T$  is the cell temperature (K), and  $N_{cell}$  is the number of cells connected in series in a module.

5.2. DC-DC Boost Converter. The DC-DC boost converter stabilizes and steps up (boosts) the unregulated DC voltage from the PV array to a DC bus voltage output, 48V, needed to charge the battery. The output voltage of the DC-DC boost converter is fed into the inverter for conversion to AC voltage. The circuit diagram of the DC-DC boost converter is shown in Figure 11. From the circuit diagram, the output voltage and current of the DC-DC boost converter are given by equations (3) and (4), respectively [15]. From the equations, it can be seen that the output of the converter depends on both the input

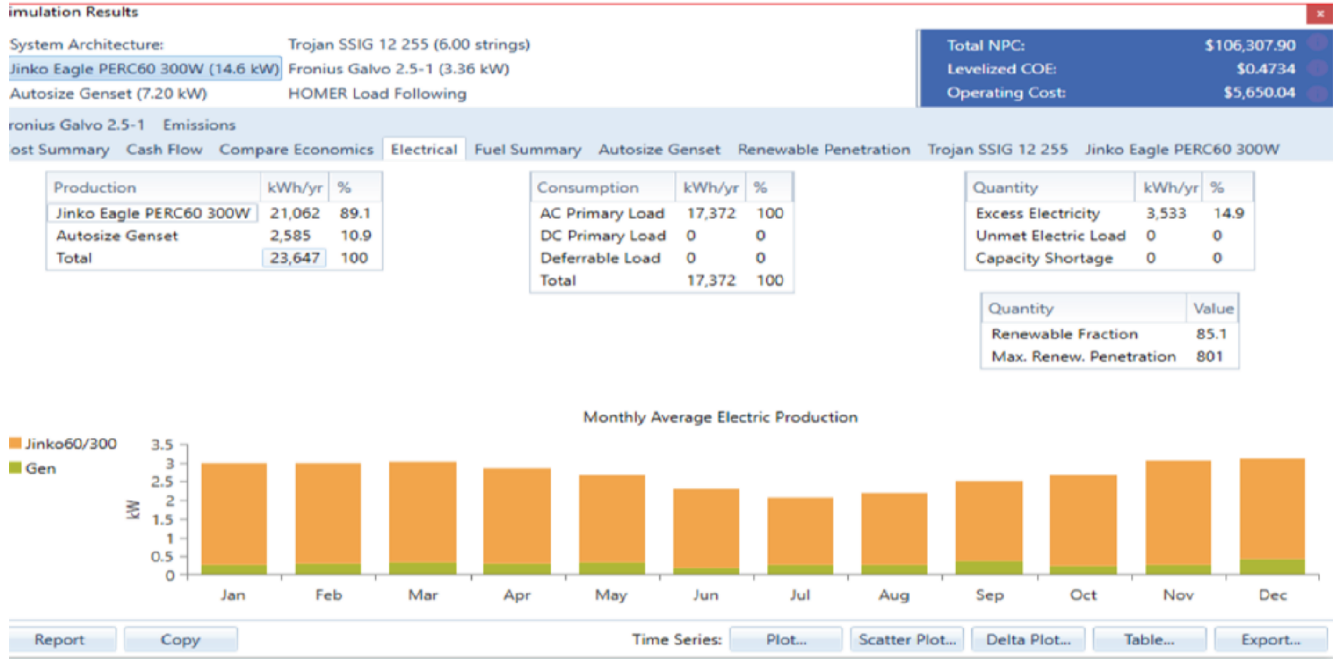


FIGURE 7: HOMER-optimized results and parameters.

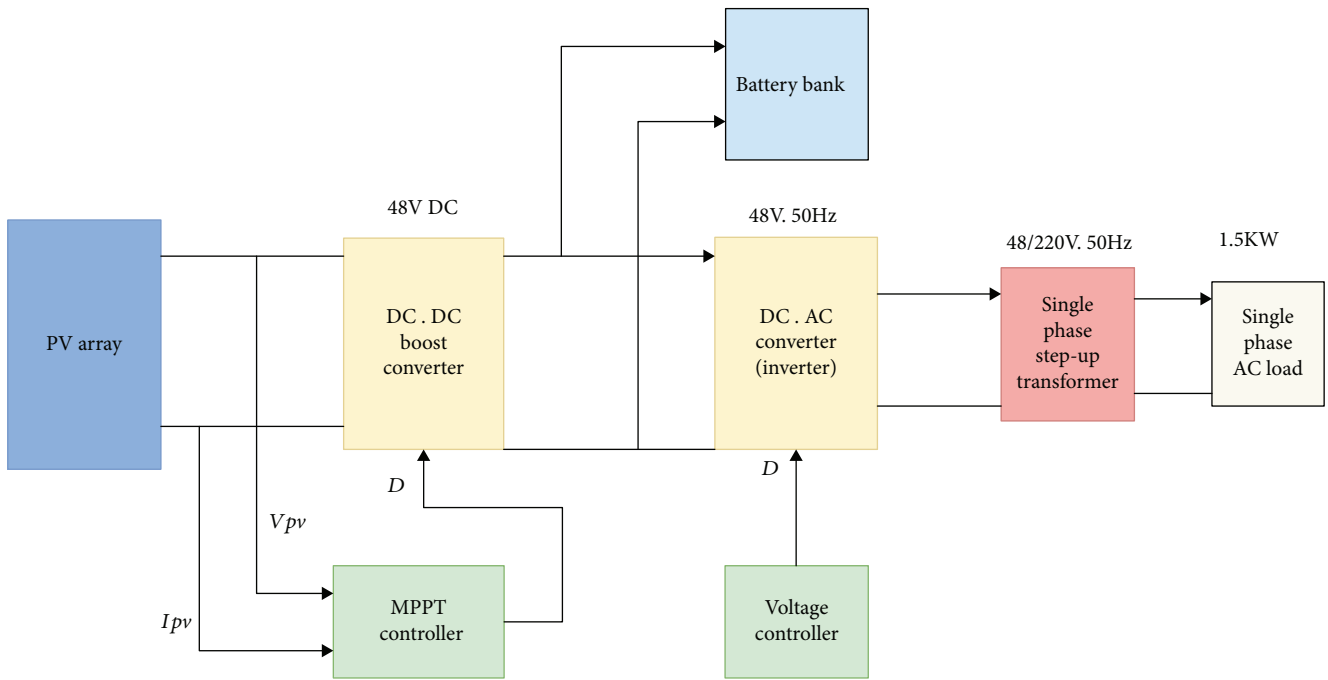


FIGURE 8: Proposed PV system block diagram.

and the duty cycle,  $D$ . Therefore, with a fixed input, the output can be controlled by controlling its duty cycle.

$$V_{dc2} = \frac{1}{(1-D)} \times V_{dc1}, \quad (3)$$

$$I_{dc2} = (1-D) \times I_{dc1}, \quad (4)$$

where  $D$  is the duty cycle of the converter.

**5.3. MPPT Controller.** At any given time, the point on the I-V curve where the solar module operates is called the operating point (OP) and it corresponds to a given irradiance ( $G$ ) and temperature ( $T$ ), which are geographical conditions. Without any external electrical control, the module OP is largely dictated by changes in the line and the load seen by the module at its output [13]. The I-V curve represents the power produced and delivered to the load. Therefore, it is important that the solar module operates at its maximum power point

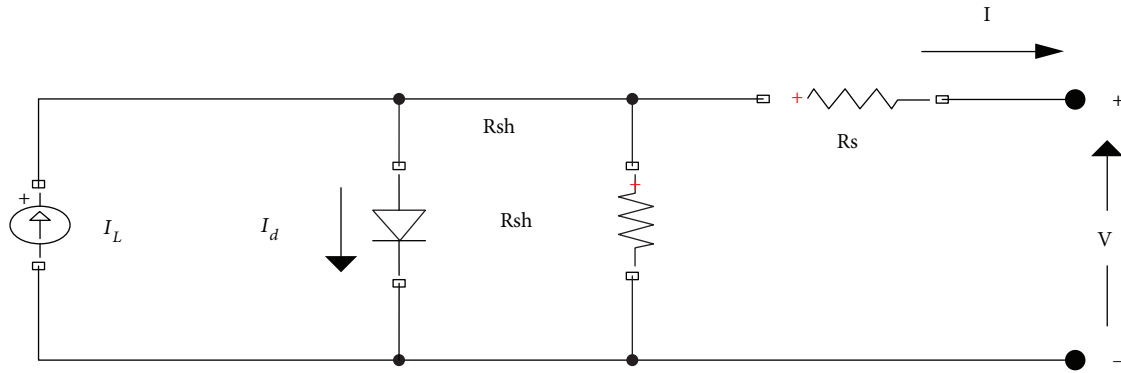


FIGURE 9: Diode model of a PV module.

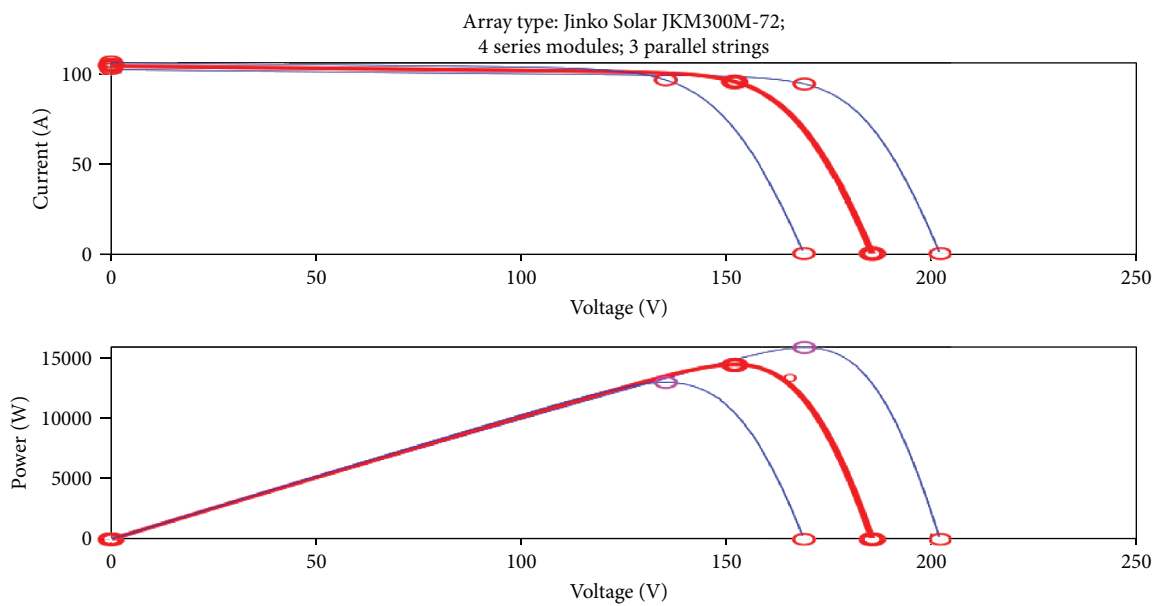


FIGURE 10: I-V and P-V characteristics of Jinko Solar JKM300M-72 PV array.

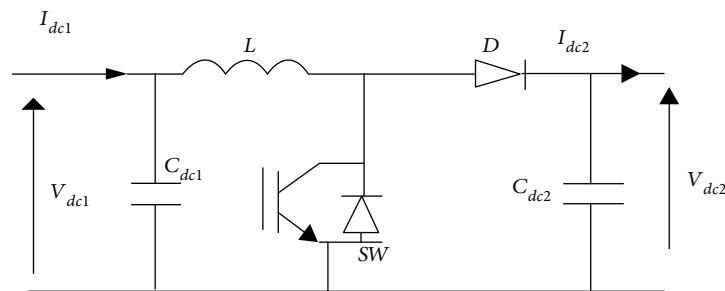


FIGURE 11: DC-DC boost converter circuit diagram.

(MPP). For maximum power output, it is important to force the module to operate at the OP corresponding to maximum power point. With changes in  $G$  and  $T$ , the I-V curve changes, which means that the previous MPP (OP) is no longer valid, and a new MPP is created. Thus, to have MPP at all times, changes in the I-V curve have to be tracked to know the new MPP, a process called maximum power

point tracking (MPPT). This is achieved using various algorithms. In this paper, the incremental conductance MPPT algorithm is chosen due to its efficiency and accuracy [13]. The voltage and current from the PV array are the inputs of the algorithm, and the generated pulses from the algorithm are used to control the duty cycle,  $D$ , of the DC-DC boost converter. This algorithm is independent of the solar

panel characteristics, rather the panel terminal voltage is changed according to its value relative to the maximum power point voltage. Equations (5) and (6) and Figure 12 illustrate the algorithm. Figure 13 shows the flow chart of this algorithm. In this project, the algorithm is implemented using Simulink blocks.

$$P = V * I, \quad (5)$$

$$\frac{dP}{dV} = \frac{d(I * V)}{dV} = V * \frac{dI}{dV} + I = 0, \quad (6)$$

where  $P$  is power,  $V$  is voltage,  $I$  is Current,  $dI/dV$  is incremental conductance, and  $I/V$  is panel conductance. At MPPT,  $dI/dV = -I/V$  or  $dP/dV = 0$ .

**5.4. Battery System.** The main purpose of the battery bank is to store extra electrical power generated by the solar PV system and to deliver the stored electrical power to the household electrical loads whenever the PV system is unavailable. The battery system is made up of 24 total batteries (6 strings in parallel, each string size being 4 batteries) of the 12 V Trojan SSIG 12, 255 lead acid battery type. The battery nominal voltage is 48 V ( $12 \text{ V} \times 4$ ), the total capacity is 1,542 Ah ( $257 \times 6$ ), and its autonomy is 29.9 hours which means that the battery system can power the house for almost one and half days if the PV system is out for maintenance or not producing power due to bad weather conditions. The Simulink block model for a lead acid battery is used to model these battery parameters.

**5.5. DC-AC Converter (Inverter).** An inverter converts a DC input supply voltage into a symmetric AC voltage of desired magnitude and frequency [16]. The single-phase voltage source inverter in this system converts the fixed DC voltage (48 V) from the DC-DC boost converter into a single-phase AC voltage (48 V) with a fixed frequency of 50 Hz. In this paper, a single-phase full-bridge inverter with insulated gate bipolar transistors (IGBTs) switches is considered. It consists of four choppers: four switches/gates S1, S2, S3, and S4 and four transistors T1, T2, T3, and T4. With T1 and T2 turned on simultaneously, input voltage appears across the load, while for T3 and T4, voltage is reversed (-Vs). Figure 14 shows a typical full-bridge IGBT-based single-phase inverter [17].

**5.6. Inverter Voltage Mode Controller.** The inverter output voltage is easily affected by variations in the line and other system parameters [16]. Therefore, there is the need for a proper control scheme to maintain a constant voltage regardless of system disturbance. The voltage mode controller scheme is proposed in this work due to its reliability and ease of implementation [16, 17]. As shown in Figure 15, the DC voltage from the boost converter is sensed and compared with a reference value. The error produced is sent to a PI controller and the PI controller produces an output which is a DC quantity. This DC quantity is multiplied by a sinusoidal value to convert it into an AC value which is then compared with a triangular waveform to produce pulses for controlling the inverter switches/gates [16].

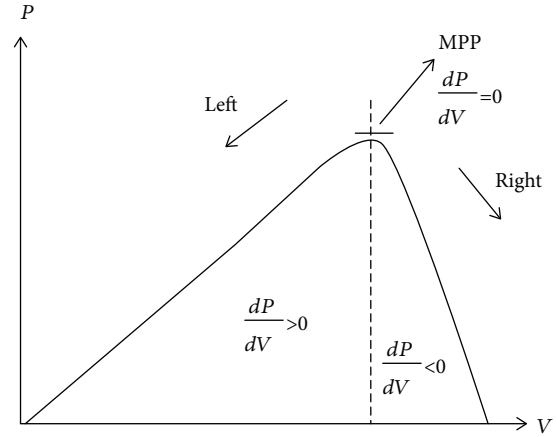


FIGURE 12: MPPT process.

**5.7. Single-Phase Step-Up Transformer.** A transformer is an electrical device used to transfer electrical energy from one level to the other at the same frequency by means of a changing magnetic field. It consists of two windings, the primary and secondary windings, separated by a magnetic core. When a transformer is used to “increase” the voltage on its secondary winding with respect to the primary, it is called a step-up transformer and when it is used to “decrease” the voltage on the secondary winding with respect to the primary, it is called a step-down transformer [18]. In this research, a single-phase step-up transformer is used to step up the 48 V voltage output from the inverter to 220 V at 50 Hz to match the household AC loads.

## 6. Proposed PV System Dynamic Simulation with MATLAB/Simulink

Dynamic modelling and simulation is the necessary first step in design, optimization, and performance analysis. In order to study the dynamic behaviors of the PV system component of the proposed hybrid power system with respect to power quality, harmonics, load impact, and voltage transients, the PV system component was simulated in MATLAB/Simulink environment under various conditions specific to the house. The complete MATLAB/Simulink model is shown in Figure 16. Each of the subsystems has been developed using standard equations and calculated and standard parameters from the manufacturers’ data sheets.

**6.1. Dynamic Simulation Results.** The most important dynamic simulation results are shown in Figures 17–22. Figure 18 shows the solar irradiance and temperature on which the PV array is made to operate, as well as the generated power output. Figure 19 shows the current, state of charge (SOC) and voltage (48 V) of the battery, and from the SOC, it can be seen that the battery is being charged by the PV system for future use. Figure 20 shows the constant DC voltage output (48 V) of the DC-DC boost converter while Figure 21 shows the generated AC voltage and frequency of the inverter (48 V, 50 Hz) fed to the transformer. The transformer steps this voltage up at the same frequency

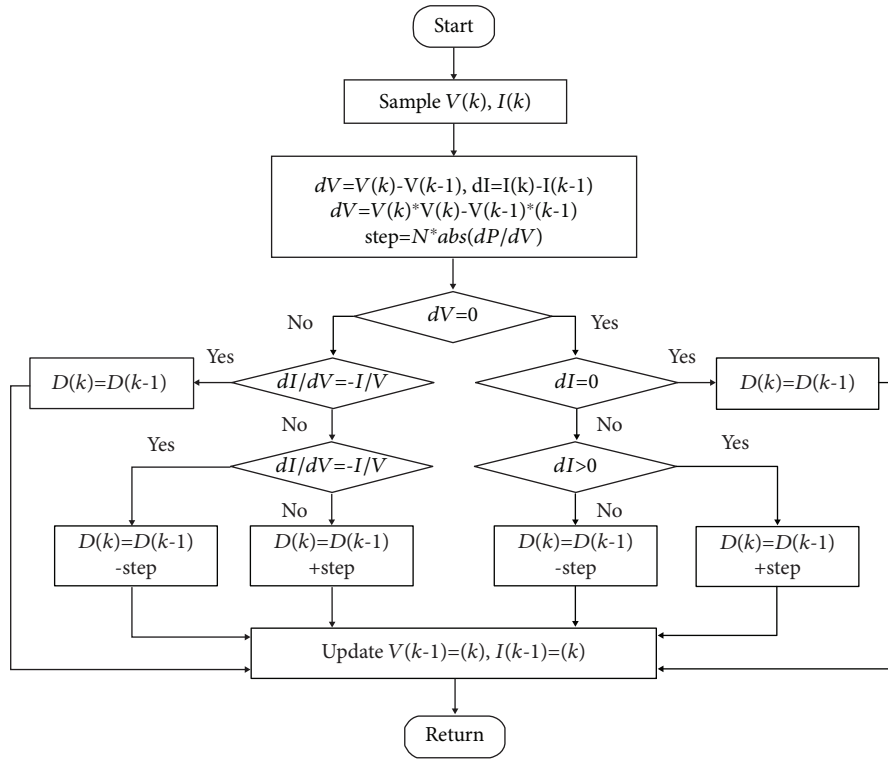


FIGURE 13: Incremental conductance MPPT flow chart.

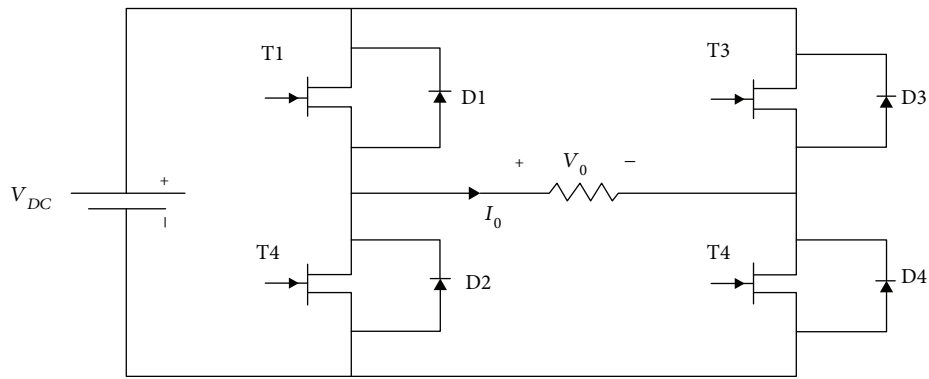


FIGURE 14: The full-bridge IGBT-based single-phase inverter.

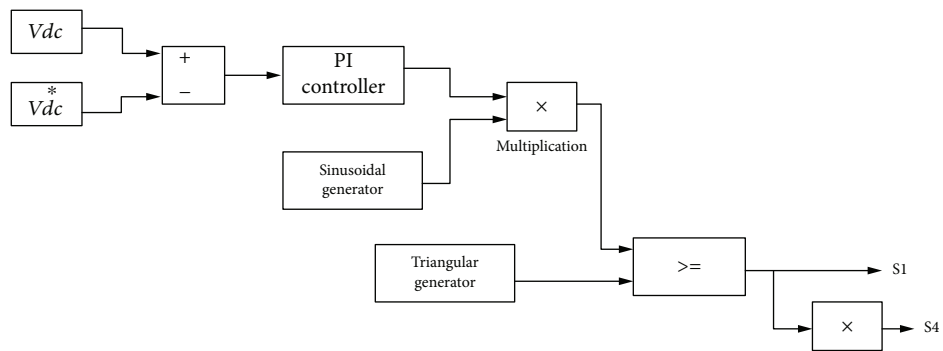


FIGURE 15: Inverter voltage mode controller block.

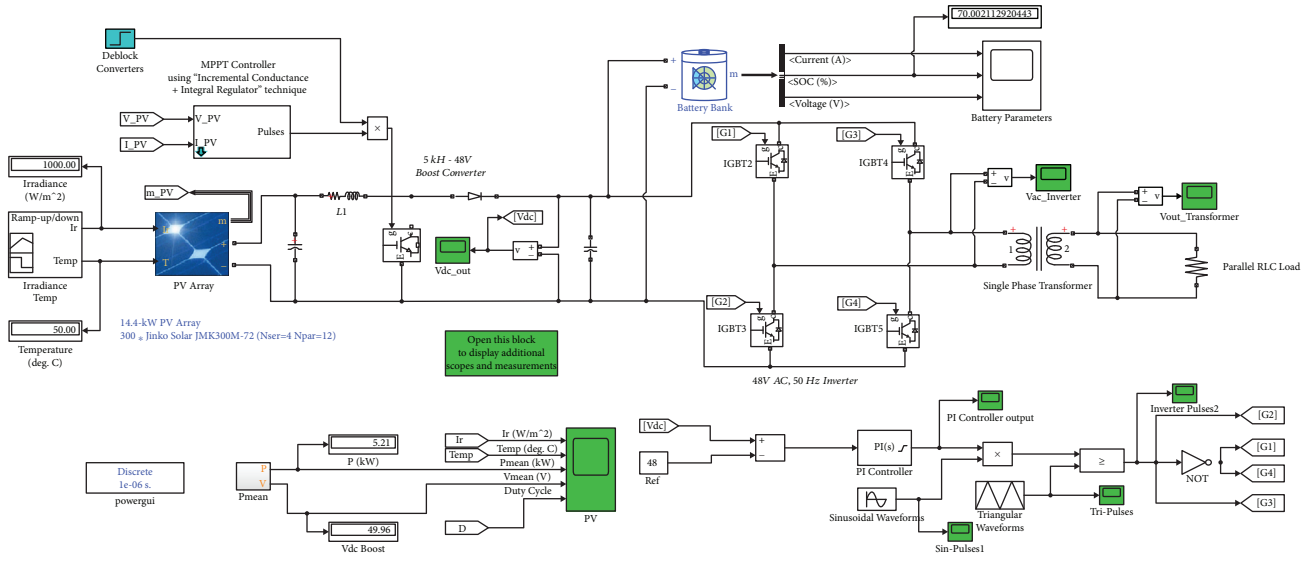


FIGURE 16: MATLAB/Simulink model of the proposed PV system.

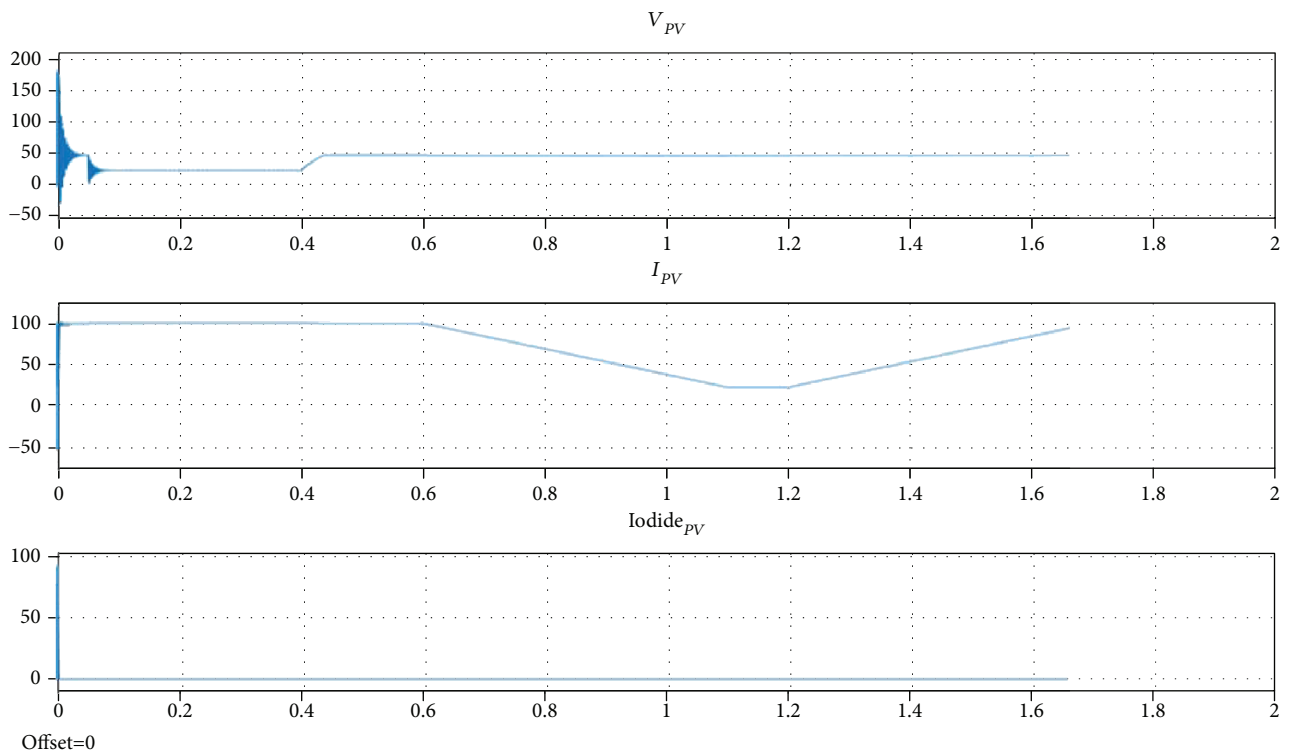


FIGURE 17: PV array voltage and current.

to 220 V for the household AC loads as shown in Figure 22. All dynamic simulations were done for 3 seconds only.

**7. Future Work**

In the future, battery management system (state of charge controller) can be included and a more sophisticated inverter control scheme (e.g., voltage oriented control, VOC) is recommended for faster response in cases of severe system

disturbance such as sudden overload. Also, hardware implementation of the proposed stand-alone PV system is to be carried out for real-life testing.

**8. Conclusions**

In this paper, thermal modelling of a house in Benin City, Edo State, Nigeria, has been carried out with BEopt software, taking into account important parameters such as the type

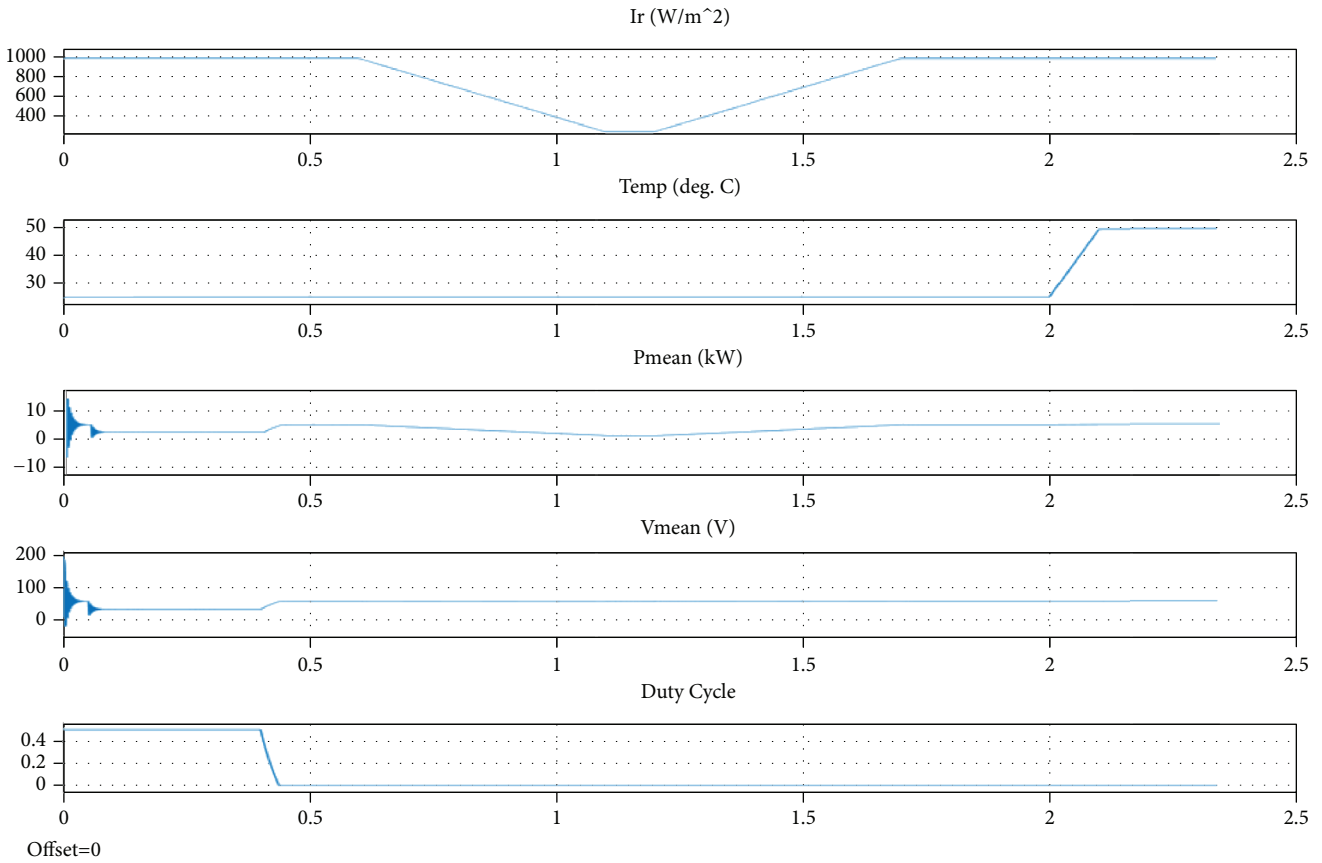


FIGURE 18: Solar irradiance, temperature, and generated power.

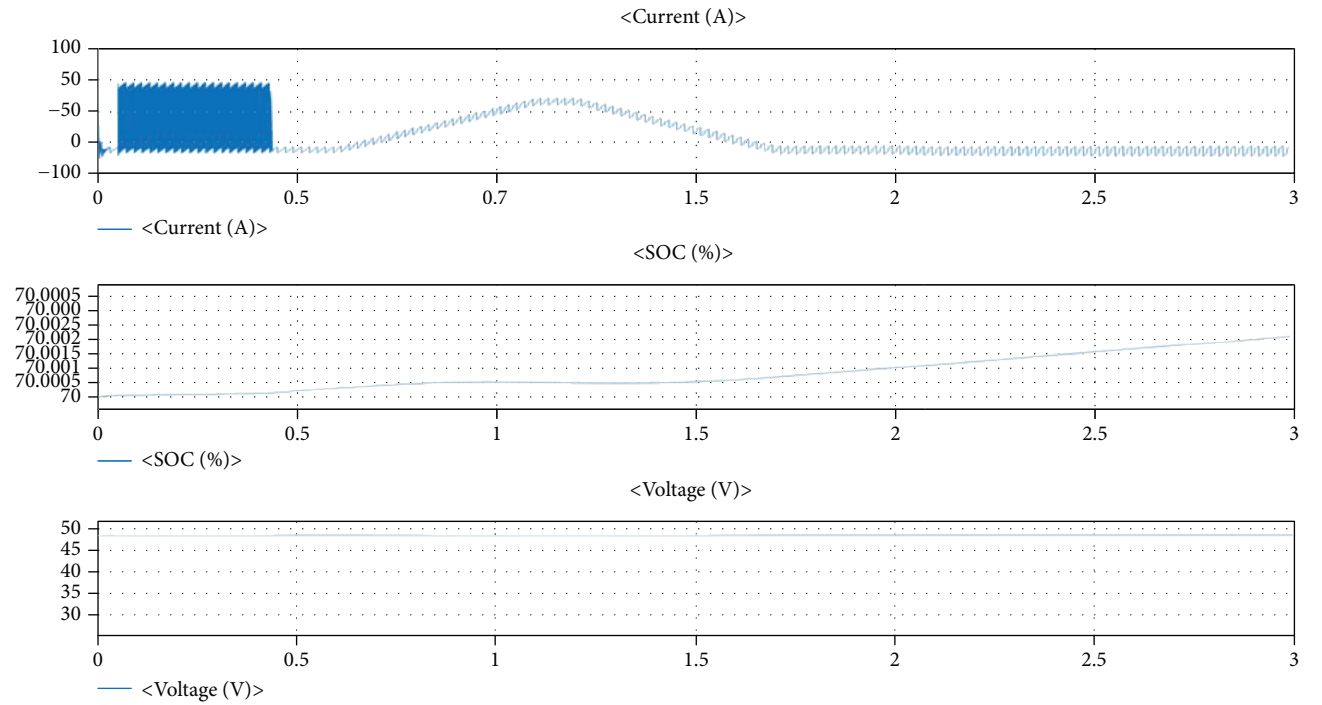


FIGURE 19: Battery current, state of charge, and voltage.

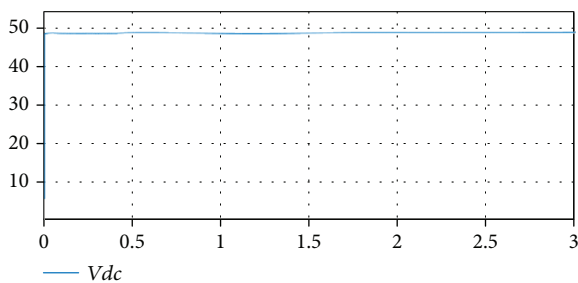


FIGURE 20: DC-DC boost converter output voltage.

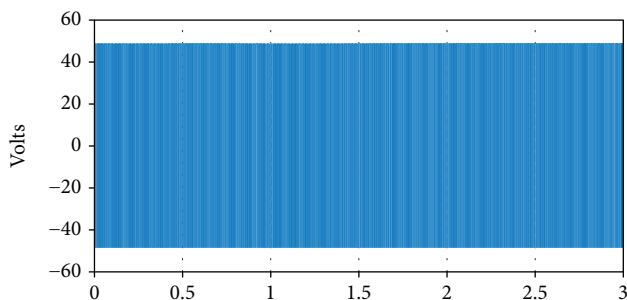


FIGURE 21: Inverter output voltage.

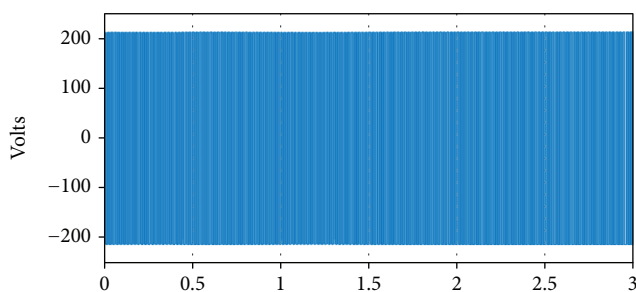


FIGURE 22: Single-phase step-up transformer output voltage/load voltage.

and size of the house, location, and orientation of the house, materials used in building the house, number and types of appliances in the house, and number of occupants. This is because the actual energy needs of a house have been found to be affected by these parameters. Having known the energy needs of the house (17,485 kWh) from BEopt thermal modelling, HOMER Pro software package was used to find an optimum stand-alone hybrid power system solution for the chosen house. To achieve this, the generated annual load profile of the house from BEopt thermal modelling simulation was imported into HOMER Pro software, and through its Add/Remove window, various components of the proposed hybrid power system, such as solar PV arrays, diesel generator, converters, and battery, were selected for simulation. This simulation took into account the project parameters, such as project lifetime, and economic parameters (i.e., costs gotten from the component manufacturers' websites), as well as the available solar irradiance in that region which was downloaded from the National Solar Radiation Database with HOMER resource window. In HOMER Pro, various

systems were simulated and technoeconomic analysis was carried out considering factors such as the size of the components, system configurations, adequacies of the various renewable energy resources, project economics with changing loads and component costs, life cycle of the system, net present cost of the system, cost of energy to the end user, maintenance costs, and annual operating costs of the hybrid power system in determining the optimum solution of the hybrid power system to meet the electrical loads of the house. The optimum hybrid power system was found to comprise of a conventional diesel generator and a solar PV system. In order to test the power quality, harmonics, load impact, and voltage transients of the proposed solar PV system component of the hybrid power system, dynamic simulation was carried out in MATLAB/Simulink environment under various system conditions. The simulated results show that the solar PV system is fully capable of powering the house and could serve as a potential solution to the energy crisis in that region.

### Data Availability

The data used to support the findings of this study are available from the corresponding author upon request.

### Conflicts of Interest

The authors declare that there is no conflict of interest regarding the publication of this paper.

### Acknowledgments

The authors would like to thank the School of Graduate Studies, Faculty of Engineering and Applied Science, Memorial University of Newfoundland for providing the conducive environment to carry out this research. The authors would also like to thank the Natural Sciences and Engineering Research Council (NSERC) of Canada Energy Storage Technology Network (NESTNet) for funding this research.

### References

- [1] <https://en.wikipedia.org/wiki/Nigeria>.
- [2] [https://en.wikipedia.org/wiki/List\\_of\\_power\\_stations\\_in\\_Nigeria](https://en.wikipedia.org/wiki/List_of_power_stations_in_Nigeria).
- [3] C. O. Okoye, O. Taylan, and D. K. Baker, "Solar energy potentials in strategically located cities in Nigeria: review, resource assessment and PV system design," *Renewable and Sustainable Energy Reviews*, vol. 55, no. 2016, pp. 550–566, 2016.
- [4] Nigerian Meteorological Agency (NiMet), "Agrometeorological Bulletin No. 10, DEKAD 2 April (11-20) 2018," <https://www.nimet.gov.ng/>.
- [5] Y.-O. N. Udoakah, E. E. Nta, I. E. Okon, and U. E. Akpabio, "Design of a 1 kva PV system for electrical laboratory in Faculty of Engineering, University of Uyo, Nigeria," in *IEEE Global Humanitarian Technology Conference (GHTC 2014)*, pp. 1–5, San Jose, CA, USA, 2014.
- [6] D. O. Akinyele and R. K. Rayudu, "Distributed photovoltaic power generation for energy-poor households: the Nigerian perspective," in *2013 IEEE PES Asia-Pacific Power and Energy*

- Engineering Conference (APPEEC)*, pp. 1–6, Kowloon, Hong Kong, 2013.
- [7] M. S. Adaramola, S. S. Paul, and O. M. Oyewola, “Assessment of decentralized hybrid PV solar-diesel power system for applications in northern part of Nigeria,” *Energy for Sustainable Development*, vol. 19, pp. 72–82, 2014.
- [8] T. A. Jesha and M. T. Iqbal, “Thermal simulation and energy consumption analysis of two houses in St. John’s, Newfoundland,” *Procedia Engineering*, vol. 105, pp. 607–612, 2015.
- [9] <https://beopt.nrel.gov>.
- [10] G. Alamri and T. Iqbal, “Sizing of a hybrid power system for a house in Libya,” in *2016 IEEE 7th Annual Information Technology, Electronics and Mobile Communication Conference (IEMCON)*, pp. 1–6, Vancouver, BC, Canada, 2016.
- [11] <https://www.homerenergy.com>.
- [12] <https://www.pveducation.org/pvcdrom/introduction/solar-energy>.
- [13] S. Peake, Ed., *Renewable Energy: Power for Sustainable Future*, Oxford University Press, 4th edition, 2018.
- [14] <https://www.mathworks.com/help/physmod/sps/powersys/ref/pvarray.html>.
- [15] S. S. Mohammed and D. Devaraj, “Simulation and analysis of stand-alone photovoltaic system with boost converter using MATLAB/Simulink,” in *2014 International Conference on Circuits, Power and Computing Technologies [ICCPCT-2014]*, pp. 814–821, Nagercoil, India, 2014.
- [16] K. Dubey and M. T. Shah, “Design and simulation of solar PV system,” in *2016 International Conference on Automatic Control and Dynamic Optimization Techniques (ICACDOT)*, pp. 568–573, Pune, India, 2016.
- [17] S. M. Cherati, N. A. Azli, S. M. Ayob, and A. Mortezaei, “Design of a current mode PI controller for a single-phase PWM inverter,” in *2011 IEEE Applied Power Electronics Colloquium (IAPEC)*, pp. 180–184, Johor Bahru, Malaysia, 2011.
- [18] <https://www.electronics-tutorials.ws/transformer/transformer-basics.html>.

## Research Article

# Flexible, Front-Facing Luminescent Solar Concentrators Fabricated from Lumogen F Red 305 and Polydimethylsiloxane

Ian A. Carbone <sup>1</sup>, Katelynn R. Frawley,<sup>1</sup> and Melissa K. McCann<sup>2</sup>

<sup>1</sup>Department of Environmental Science and Sustainability, Allegheny College, Meadville, PA 16335, USA

<sup>2</sup>Department of Materials Science and Engineering, Washington University, St. Louis, MO 63160, USA

Correspondence should be addressed to Ian A. Carbone; [icarbone@allegheny.edu](mailto:icarbone@allegheny.edu)

Received 24 January 2019; Revised 12 March 2019; Accepted 28 March 2019; Published 30 April 2019

Guest Editor: Mattia De Rosa

Copyright © 2019 Ian A. Carbone et al. This is an open access article distributed under the Creative Commons Attribution License, which permits unrestricted use, distribution, and reproduction in any medium, provided the original work is properly cited.

Luminescent solar concentrators (LSCs) fabricated with transparent host materials and fluorescent organic dyes are cost effective and versatile tools for solar power production. In this study, the first flexible, front-facing LSCs utilizing Lumogen F Red 305 (LR305) and polydimethylsiloxane (PDMS) were demonstrated. Bulk-doped devices, fabricated with dye evenly distributed throughout the waveguide, were optimized for light gain with LR305 concentrations between 0.075 and 0.175 g/l. Thin-film devices, fabricated with a thin layer of luminescent material applied to the bottom side of the waveguide, were optimized between 0.5 and 0.75 g/l. The bulk-doped and thin-film devices produced light gains of 1.86 and 1.89, respectively, demonstrating that flexible designs can be developed without sacrificing power production. Bulk-doped devices proved to be less effective than thin-film devices at collecting direct light due to the placement of fluorescent dyes above the front-facing solar cell. Thin-film devices demonstrated less light collection than bulk-doped devices further from the device centers possibly due to quenching and self-absorption losses at higher dye concentrations. Light collection was minimally impacted by moderate bending in both LSC designs, suggesting that flexible, front-facing devices could be effectively deployed on curved and uneven surfaces. Finally, optical measurements of the LSC waveguides suggest that they could support plant growth underneath. Similar designs could be developed for applications in agricultural settings.

## 1. Introduction

Photovoltaic module prices have decreased dramatically over the last decade [1, 2], and by some estimates, U.S. and global solar capacities will more than double in the next five years [3, 4]. In light of the growth and trajectory of solar markets, it is important to investigate the space-related requirements and limitations of solar technologies in order to develop land resources mindfully. Several researchers have explored best practices for minimizing land use and environmental disturbances when working with more established solar technologies [5–9], while several others have developed systems that allow for power generation in a greater variety of locations [10–14]. Luminescent solar concentrators (LSCs), first developed in the 1970s, are a promising group of semitransparent solar devices that can be deployed in a variety of alternative settings [15–17]. In this manuscript, we explore the use of

LSCs for more efficient solar power generation and space utilization in agricultural settings.

LSCs consist of one or more solar cells attached to a transparent plate, or waveguide, that has been doped with a fluorescent dye [16, 17]. Dye molecules can be dispersed throughout the waveguiding material in what we refer to as a “bulk-doped” device or applied in a concentrated layer to the front or back of what is commonly called a “thin-film” device [18]. In both cases, the fluorescent material serves to absorb and reemit light inside the waveguide, where a significant fraction becomes trapped due to total internal reflection. Strategically placed solar cells mounted onto the waveguides collect concentrated light and generate electricity. Due to their semitransparent designs, LSCs can be developed for a greater variety of applications than conventional photovoltaics. Waveguides can be designed to absorb and transmit desired portions of the electromagnetic spectrum,

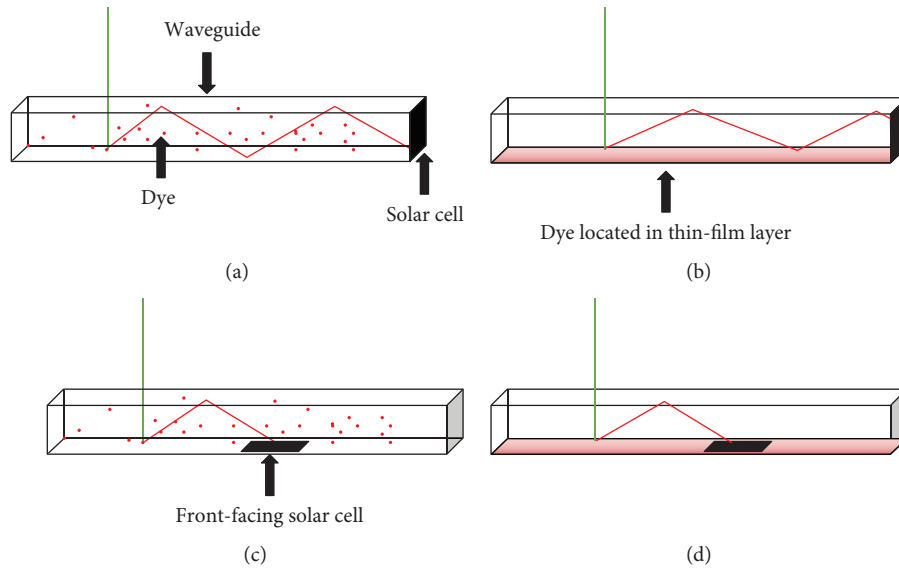


FIGURE 1: Conventional bulk-doped (a) and thin-film (b) LSC designs utilizing edge-mounted solar cells. Front-facing bulk-doped (c) and thin-film (d) LSC designs. Dye molecules are dispersed throughout the waveguiding material in the bulk-doped device and applied in a concentrated layer to the backside of the thin-film device. Both designs rely on total internal reflection in the waveguide to concentrate light.

and LSC panels can be integrated into built environments as power-generating windows [14, 19–23].

Most published LSC designs place solar cells on the edges of waveguides in order to maximize light gain (Figures 1(a) and 1(b)); however, some researchers have focused recent efforts on developing bottom-mounted, or front-facing, designs (Figures 1(c) and 1(d)) [24–30]. By orienting the solar cells to face the light source, they are able to collect direct light in addition to concentrated light. On larger LSCs with significant distances between edges, front-facing cells can also be strategically placed to minimize the average distance traveled by concentrated light in the waveguide. Another advantage of front-facing designs is that they allow designers to control the fraction of the LSC area that is covered by solar cells. Front-facing LSCs with power conversion efficiencies of 6.8% have been fabricated by covering 31% of the device area with solar cells [24]. Other devices have been able to double the photon flux received by embedded solar cells with 5% solar cell coverage [24].

In addition to device geometry, dye selection and processing can significantly impact LSC performance. Dye-dye and dye-host interactions can cause quenching and/or self-absorption losses, and waveguides often decrease in performance when dyes are highly concentrated or unevenly distributed in their host matrix [31–33].

BASF’s Lumogen F Red 305 (LR305) is a soluble perylene dye with a high fluorescence quantum yield and high photostability, making it one of the most popular LSC dyes available [31–33]. LR305 is also a well-suited LSC material for agricultural applications. When LR305 is suspended in ethanol, polycarbonate, and polydimethylsiloxane (PDMS), absorbance maxima occur at 578, 573, and 560 nm, respectively, and emission maxima in these materials occur at 613, 597, and 590 nm, respectively [31]. Because most plants rely on the red and blue portions of the solar spectrum,

LR305-based materials can avoid interfering with the wavelengths required for photosynthesis. In 2016, Corrado et al. [19] demonstrated vegetable production underneath front-facing LSC panels fabricated with LR305 in a demonstration greenhouse. A follow-up study concluded that these greenhouse LSCs had no negative impacts on tomato production and that some varieties of crops might respond positively to the LSC greenhouse conditions [34]. Similar greenhouse panels that offer wavelength-selective power production have since entered the marketplace, and there appears to be a growing market for solar materials that also support growing environments [35, 36]. As LSCs continue to be developed for agricultural applications, there is an opportunity to develop new devices that can be deployed in growing environments that are ill-suited for rigid LSC panels. For curved and uneven surfaces, like hoop houses, low tunnels, and open fields, a flexible LSC fabric would be far more easily deployed and maintained.

A number of studies have developed flexible LSCs [28, 31, 37–41], and one of the most well-documented flexible waveguide materials is polydimethylsiloxane (PDMS), a silicon-based organic polymer with high transparency, flexibility, and durability. Past research has demonstrated successful edge-mounted LSCs using PDMS and LR305 [31, 42]; however, this study is the first to utilize these materials in a front-facing LSC design. After optimizing bulk-doped and thin-film designs for dye concentration, a detailed analysis of waveguide properties and light gains is carried out to help guide future device development.

## 2. Materials and Methods

*2.1. Device Fabrication.* To begin the LSC fabrication process, reference cells were prepared and characterized before being incorporated into finished LSC devices. 17.5%

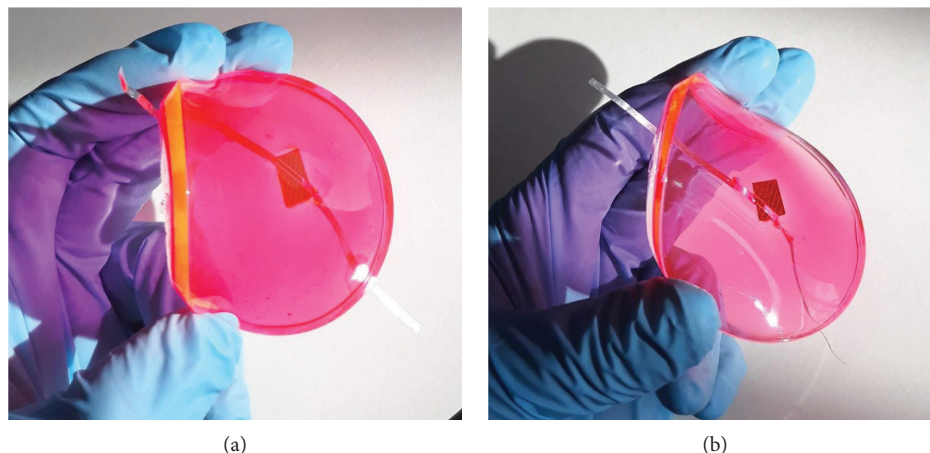


FIGURE 2: Finished LSC devices. The bulk-doped LSC (a) has dye evenly distributed throughout the waveguide. The thin-film LSC (b) has a thin ( $\sim 0.26$  mm) layer of concentrated dye applied to the bottom surface. The front-facing solar cell can be seen in the center of both flexible devices.

efficient MISOL monocrystalline solar cells were cut into  $\sim 1$  cm  $\times$  1 cm reference cells using a diamond scribe, and 3 inches of tabbing wire were soldered onto the front and back contacts. More precise reference cell areas were measured using a HP Scanjet 8300 scanner and GIMP image manipulation software for the calculation of reference cell efficiencies. Finally, reference cells were electrically characterized (see details in Section 2.3) and set aside until the waveguides were fabricated.

Bulk-doped waveguides were constructed by combining Dow Corning SYLGARD 184 base and curing agents with a base to curing agent ratio of 10:1. BASF LR305, which was stored in an 8 g/l toluene solution, was combined with the SYLGARD 184 mixtures to achieve the desired device dye concentrations. After combining thoroughly by hand, the PDMS mixtures were poured into 7 cm diameter glass petri dishes to form 4 mm thick films. The PDMS mixtures were placed into an evacuated vacuum oven until all air bubbles were released and then heated for 30 minutes at  $100^\circ\text{C}$  to cure. After removing the solid waveguides from the petri dishes, reference cells were attached to the centers of the waveguides using a small amount of the undoped SYLGARD 184 mixture. The materials were heated for an additional 10 minutes to complete the bulk-doped LSCs. We found that the durability of finished LSCs could be significantly increased by attaching a thin layer of rigid material to the back of the solar cells; however, this was not necessary for the devices characterized in this study. A finished bulk-doped device is pictured in Figure 2(a).

The thin-film device fabrication process began by modifying the bulk-doped procedure to produce clear waveguides that contained no dye. After attaching reference cells to the clear waveguides, SYLGARD 184 mixtures were created with the desired thin-film dye concentrations. 1 ml of the dye mixtures was poured onto the back of each waveguide, spread with a spatula, and allowed to settle for one hour on a level surface. The devices were heated for an additional 10 minutes at  $100^\circ\text{C}$  to cure the dye-containing layers. A finished thin-film device is pictured in Figure 2(b).

It is worth recognizing that our “thin-film” LSCs belong to a broader class of designs that contain concentrated layers of dye on the top or bottom surfaces of the waveguide. The dye-containing layers used in this study, however, would not be considered “thin-films” by the standards of modern materials science. Our fabrication methods deposited films that were approximately 0.26 mm thick.

In this experiment, bulk-doped and thin-film LSCs were fabricated and tested with concentrations ranging from 0.02 to 0.50 g/l and 0.25 to 1.00 g/l, respectively. 3 LSCs were constructed at 7 concentrations for each device type. The 42 LSCs considered in this study were optically and electrically characterized as described in the sections below.

**2.2. Optical Characterization.** Absorbance and transmittance measurements of LSC waveguides were carried out on an Ocean Optics spectroscopy system with USB2000+ spectrometer, LS-1 light source, and SpectraSuite software. Absorbance spectra of bulk-doped and thin-film LSCs allow us to compare light collection in the two designs. Transmittance values are compared to the absorbance spectra of plant pigments to assess LSC compatibility with growing environments. For reference, the optical properties of LR305-doped PDMS waveguides have been studied in greater detail by Buffa et al. [31] and Steinbruck et al. [43].

**2.3. Electrical Characterization.** I-V curves of naked reference cells and finished LSCs were measured with an AM1.5 Abet-Technologies SunLite 11002 solar simulator and Keithley 2400 SourceMeter. During characterization, the LSCs were situated above a sheet of 83% reflective office paper by placing 1.6 mm foam spacers underneath the center and outer edges of the LSCs. A 4 mm strip of 83% reflective paper was also taped around the outer edges of the devices to standardize test conditions across devices and measurements. Short circuit currents, open circuit voltages, fill factors, and power conversion efficiencies were calculated from the I-V curves of each LSC before and after the attachment of the reference cells to quantify changes in light collection. The

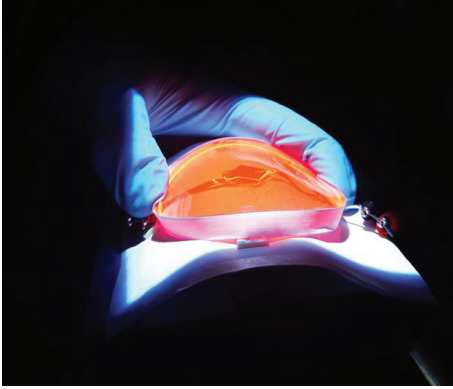


FIGURE 3: Electrical characterization of a bulk-doped LSC device pressed over a 5 cm bend tool. The LSC is placed above and inside of the 83% reflective paper. Due to the rigid solar cell placed in the device center, only regions outside the 1 cm  $\times$  1 cm square were allowed to bend.

majority of this study's analysis focuses on changes to the short circuit current, which are directly proportional to changes in the photon flux received by the reference cells. We define light gain as follows:

$$\text{Light gain} = \frac{I_{\text{LSC-short circuit}}}{I_{\text{Reference cell-short circuit}}}. \quad (1)$$

After the initial device characterization, a masking experiment was carried out to compare light collection from different locations on the LSC surfaces. Masks were created to shade the perimeter regions of each device from incident light, and light gains were measured over a range of mask radii. Light gains were then divided by the exposed areas, and values were compared in order to highlight differences between the inner and outer regions of the LSC devices.

Bent devices were also electrically characterized to investigate the impacts of bending on light concentration. Like the above measurements, LSCs were placed 1.6 mm above 83% reflective paper. Both the paper and the LSCs were pressed over bend tools (partial cylinders with radii of curvature between 2 and 8 cm) and characterized with I-V curves. For clarity, Figure 3 provides an image of a bulk-doped LSC being characterized over a 5 cm bend tool.

Device performances during the bending experiments were calculated according to

$$\text{Bent performance} = \frac{I_{\text{Bent LSC}} - I_{\text{Ref. cell}}}{I_{\text{Flat LSC}} - I_{\text{Ref. cell}}}. \quad (2)$$

Following this equation, short circuit current measurements of the naked reference cells were subtracted from the short circuit currents of completed, bent LSCs in order to isolate light gains attributed to concentrated light in the waveguide (as opposed to the collection of direct light). These values were then scaled by their unbent values so that trends could be easily compared across devices.

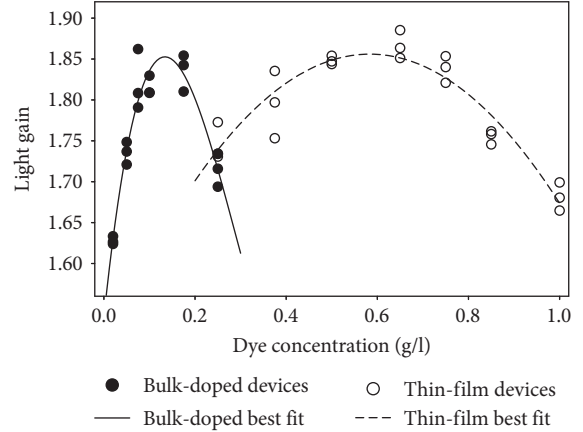


FIGURE 4: Light gains of bulk-doped and thin-film devices plotted against dye concentration. Bulk-doped devices were optimized for light gain with LR305 concentrations between 0.075 and 0.175 g/l. Thin-film devices were optimized between 0.5 and 0.75 g/l. Best fit second-order polynomials are included to visualize trends in each data set.

### 3. Results and Discussion

**3.1. Optimization of Dye Concentrations.** Both bulk-doped and thin-film LSCs were fabricated over a range of dye concentrations and characterized so that light gains could be compared. Figure 3 presents the light gains of all 42 LSCs considered in this study and shows that individual devices varied in performance by up to 5% even when they utilized the same design and dye concentration. These differences were likely due to minor variations in device construction. Bonds between device layers and dye distributions varied slightly between LSCs as did the sizes and placements of solar cells and contacts.

Despite these differences, the light gains in both sets of devices were clearly correlated with dye concentration. Figure 4 indicates that bulk-doped devices were optimized with LR305 concentrations between 0.075 and 0.175 g/l. These values are consistent with the optimized concentrations found by Buffa et al. [31] for side-mounted LSCs made from LR305 and PDMS.

Because thin-film devices utilized thinner layers of luminescent material, higher dye concentrations were necessary to maintain light absorption. The thin-film LSCs in this study exhibited their highest light gains between 0.5 and 0.75 g/l, which is significantly lower than previously published thin-film LSCs made with LR305 and PMMA [33, 44]. Dye aggregation issues documented in previous studies of LR305 and PDMS may be responsible for limiting performance at higher concentrations [31].

**3.2. Individual Devices.** The individual bulk-doped and thin-film LSCs with the largest light gains are characterized in greater detail below. The IV curves of reference cells and completed LSCs presented in Figure 5 allowed for the calculations of the efficiencies and light gains presented in Table 1. While the thin-film device with 0.65 g/l dye

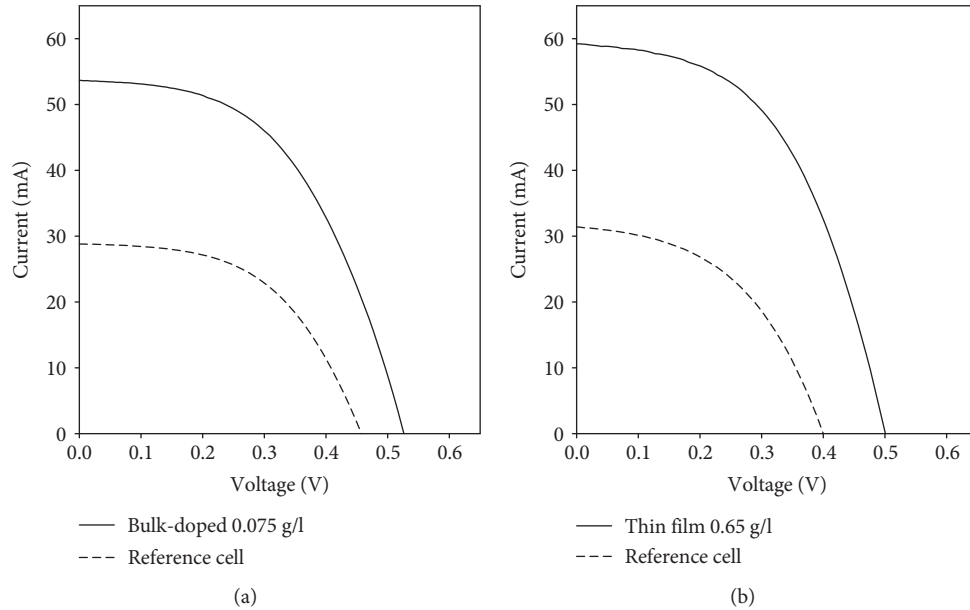


FIGURE 5: IV curves of optimized bulk-doped (a) and thin-film (b) LSCs and reference cells. Open circuit voltages and short circuit current both experience gains with increased irradiance. The relatively low open circuit voltages of the naked reference cells may suggest that a relatively high fraction of incident light was obstructed by contacts and tabbing wire located on the cell surface.

TABLE 1: Characteristics of optimized bulk-doped and thin-film LSCs.

Device structure	Dye concentration (g/l)	Light gain	Ref. cell efficiency (%)	Final device efficiency (%)
Bulk-doped	0.075	1.86	6.43	0.37
Thin film	0.65	1.89	5.76	0.39

concentration recorded a slightly greater light gain than the 0.075 g/l bulk-doped device, the two values were within the ranges of experimental uncertainty observed between similarly constructed devices. In an earlier study of thin-film, front-facing devices made with LR305 and PMMA, Corrado et al. [24] demonstrated a light gain of 1.85 for LSCs with the same cell size (1 cm  $\times$  1 cm) and coverage (2.6%) as the devices in this study. This value is 3% less than the optimized light gains in this study, suggesting that flexible devices can be constructed with PDMS as opposed to PMMA without sacrificing light concentration.

The efficiencies of optimized bulk-doped and thin-film LSCs were 0.37% and 0.39%, respectively. These values are lower than many previously published front-facing LSCs [24, 29, 30] for two major reasons. First, the LSCs in this study were designed to optimize light gain rather than device efficiency. As a result, a relatively small fraction (2.6%) of the LSC areas were covered with solar cells, resulting in lower efficiencies. Secondly, the hand-cut and soldered reference cells had relatively low efficiencies before they were incorporated into completed LSCs. The relatively low open circuit voltages of the naked reference cells in Figure 5 suggest that a relatively high fraction of incident light was obstructed by contacts and tabbing wire located on the cell surface. While this should not have had a significant impact on light gain measurements and calculations, it did negatively impact on

overall LSC efficiency. If future devices could achieve the same light gains using record-holding 26.7% efficient monocrystalline cells, these LSC designs could theoretically achieve efficiencies of 1.29% for bulk-doped devices and 1.31% for thin-film devices [45].

**3.3. Waveguide Absorption.** Bulk-doped and thin-film LSCs produced similar light gains, but the two designs exhibited important differences in their optical properties. If the dye properties and light collection processes remained consistent between devices, we would expect the thin-film and bulk-doped LSCs to be optimized with similar optical densities and similar dye quantities (even if the dye might be more concentrated in the thin-film construction) [46]. However, the optimized thin-film LSC contained 58% less dye than the optimized bulk-doped device, and absorbance values in Figure 6 demonstrate that the thin-film LSC exhibited lower absorbance values across the spectrum. While both waveguides demonstrate an absorbance peak at 565 nm, the thin-film absorbance in this region is almost 56% less than the bulk-doped measurement. One possible explanation for the low optical densities of optimized thin-film LSCs is that dye interactions were limiting device performance at higher concentrations.

These results are supported by studies that have characterized LR305-doped PDMS in greater detail. Steinbruck

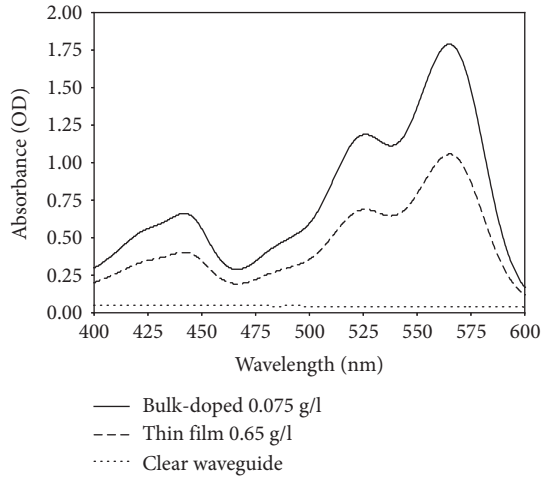


FIGURE 6: Absorbance spectra of bulk-doped, thin-film, and clear LSC waveguides. The thin-film waveguide had a 56% lower absorbance than the bulk-doped waveguide at 565 nm. Quenching and self-absorption may limit thin-film device performance at higher dye concentrations, resulting in devices that are optimized with lower optical densities.

et al. [43] found that LR305 is prone to aggregation in PDMS due to low solubility. Similarly, Buffa et al. [31] observed quenching and self-absorption losses in PDMS waveguides when concentrations of LR305 exceeded 0.1 g/l. The optimized thin-film LSC in this study had a concentration of 0.65 g/l (well above 0.1 g/l) suggesting that thin-film devices were limited to lower optical densities than the bulk-doped LSCs due to increased quenching and self-absorption losses at higher dye concentrations.

**3.4. Light Gain and Aperture.** To compare light collection from the inner regions (near the device center) and outer regions (near the device perimeter) of the finished LSCs, light gains were measured while the device perimeters were shaded from incident light. Figure 7 presents the light gains per unit of exposed area for the optimized bulk-doped and thin-film LSCs. Bulk-doped and thin-film devices both exhibited similar trends to previously characterized rigid devices [24, 29, 30]. Light gain contributions were greatest near the device centers due to the capture of direct light and the short travelling distance for concentrated light. At locations closer to the device perimeters, the light gain contributions were diminished due to dye and waveguide reabsorption.

The thin-film device in Figure 7 outperformed the bulk-doped device at smaller apertures due to differences in the waveguide properties above the solar cell. Unlike the thin-film device, the bulk-doped solar cell was mounted beneath a waveguide that contained dye, and this dye absorbed and reemitted some direct light before it could be collected by the solar cell. Because the bulk-doped and thin-film devices performed similarly when most or all of the device surfaces were exposed to incoming light, we conclude that the bulk-doped device was more effective at collecting concentrated light from the outer regions of the waveguide. Poor light harvesting from the thin-film waveguide is consistent with the

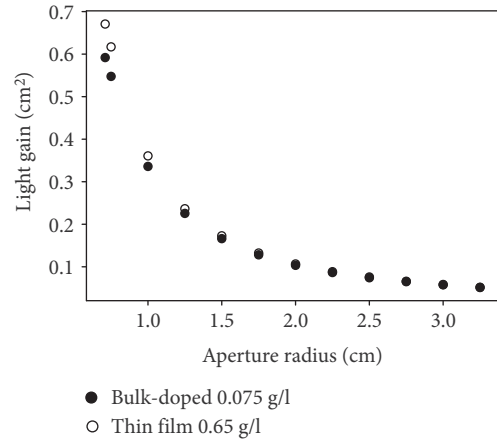


FIGURE 7: LSC light gains per unit exposed area during masking experiments. The thin-film device was more effective at collecting direct light. The bulk-doped device was more effective at collecting concentrated light from the waveguide.

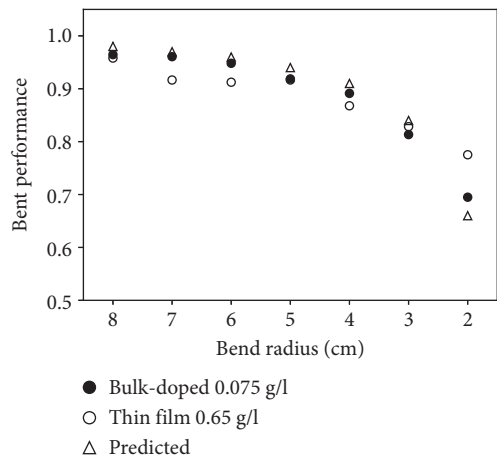


FIGURE 8: Bent waveguide performance. Values represent the bent waveguide light gains scaled by the flat waveguide light gains. Both devices performed similarly to predicted values determined by the fraction of light intercepted by the bent geometry.

lower waveguide absorbance and possible dye interactions found in Section 3.3.

**3.5. Device Bending.** Bent devices were characterized to explore the feasibility of deploying front-facing LSCs on curved and/or uneven surfaces. Figure 8 shows the bent waveguide performance when the optimized devices were curved over bend tools with radii between 8 and 2 cm. To quantify our bend performance, short circuit currents of device reference cells were subtracted from the short circuit currents of the finished devices and the results were scaled by the corresponding unbent values (see equation (2)).

Figure 8 indicates that the optimized thin-film LSC was less impacted than the bulk-doped devices at small bend radii. This result is consistent with the masking results

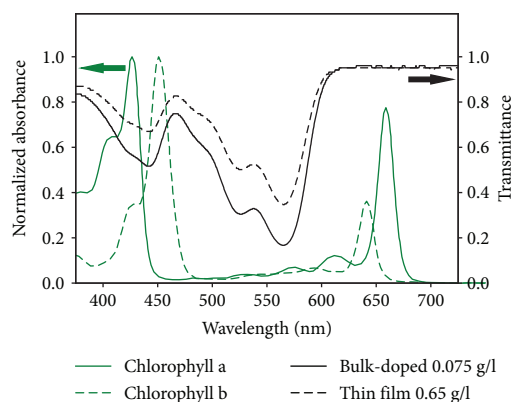


FIGURE 9: Waveguide transmittance and normalized absorbance of chlorophylls a and b in diethyl ether. Waveguides of both devices primarily concentrate wavelengths between 500 and 600 nm and transmit the majority of the light absorbed by the two primary plant pigments. The optimized thin-film LSC transmits more light due to its lower optical density. Absorbance measurements were taken from Lichtenthaler [47].

discussed in Section 3.4. More extreme bending disproportionately impacted light collection near the device perimeters where reabsorption losses had their greatest impact. The thin-film device was less impacted by this bending due to the losses that were already occurring near the LSC perimeter.

In a study on flexible LSCs made with monocrystalline  $\mu$ -cells, Yoon et al. [28] found that light gains in bent devices were proportional to the areas of the bent devices projected onto a plane normal to the incident light. To test devices in this study against this trend, values for projected device areas were expressed as fraction of flat device areas and included in Figure 8. The LSCs in this study followed the predicted trend with the exception of the thin-film device at the 2 cm bend radius. The general agreement with the predicted values for both LSCs is consistent with findings from Tummeltshammer et al. [41] who showed that the moderate bending of flexible waveguides does not significantly increase escape cone losses.

**3.6. Growing Environment.** Optical measurements of our optimized waveguides provide insight into the agricultural growing environments that could be supported underneath the LSC materials considered in this study. Figure 9 presents waveguide transmittance values alongside the absorbance spectra of chlorophylls a and b, the primary photoreceptor pigments in photosynthesis. Absorbance spectra, taken from Lichtenthaler [47], demonstrate that chlorophyll a absorbs most strongly at 428 nm and 660 nm and chlorophyll b absorbs most strongly at 452.2 nm and 641.8 nm. All of these values are distinct from the minimum waveguide transmittance at 565 nm.

More than 95% of photosynthetically active light in the red portion of the solar spectrum was transmitted through the optimized LSC waveguides. However, transmittance was significantly diminished at photosynthetically active blue wavelengths due to the broad shoulder of the LR305

absorption peak. The transmittance of the optimized bulk-doped waveguide at 426 nm, for example, was only 57%. The thin-film waveguide transmitted a larger fraction of these blue wavelengths, due to its lower dye content and optical density. Because the thin-film design both absorbed less light than the bulk-doped design and emitted less down-shifted light from the surfaces of the waveguide, the two waveguides exhibited similar transmittance values in the red portion of the spectrum.

Despite the altered spectrum created by the LR305-PDMS layers, this LSC technology still holds promise for applications in agricultural operations. The impacts of these waveguides on incident spectra are nearly identical to those documented in LR305-PMMA/glass greenhouse panels that successfully supported tomato production in past studies [19, 34]. Researchers in one study also noted that crop varieties have varied responses to altered spectra and some varieties may benefit from reduced levels of blue light [34]. The best designs for future growing conditions will almost certainly depend on the needs of the specific plant varieties being grown.

## 4. Conclusions

In this study, the first flexible front-facing LSCs utilizing LR305 and PDMS were demonstrated. Bulk-doped devices were optimized for light gain with LR305 concentrations between 0.075 and 0.175 g/l. Thin-film devices were optimized between 0.5 and 0.75 g/l. The two device constructions demonstrated similar light gains to comparable rigid devices made with PMMA and LR305. Bulk-doped devices proved to be less effective at collecting direct light, and thin-film devices appeared less effective at concentrating light due to quenching and self-absorption losses at higher dye concentrations. Light collection was minimally impacted by moderate bending in both LSC designs, suggesting that flexible, front-facing devices could be developed into effective tools for power generation on curved and uneven surfaces.

Our data suggest that quenching and self-absorption losses are important limiting factors in LR305-PDMS LSCs. Future research should be carried out to quantify escape cone and nonunity quantum yield losses in flexible, front-facing devices. Another area of inquiry is to explore other flexible host materials such as polymethylphenylsiloxane (PMPS) and polyethylene terephthalate (PET).

Transmittance measurements of the optimized waveguides in this study suggest that both designs significantly alter the potential growing conditions underneath the devices. In particular, they significantly reduce the amount of blue light that plants would receive if these technologies were to be installed above crops in agricultural settings. However, past studies on rigid LSC panels suggest these conditions can still support productive growing environments [34]. LSCs modeled after our bulk-doped designs would support growing environments with less blue light than those modeled after our thin-film designs, but the best designs for future growing conditions will depend on the needs of the specific plant varieties being grown.

Future research is still needed to better understand how specific crop varieties respond to these altered spectra (in particular, reduced levels of blue light). Another area of concern is the long-term durability of LR305-PDMS devices in outdoor environments. For this reason, a variety of UV stabilizers and flexible host materials should be considered and subjected to reliability and durability testing. Additional prototypes should also be developed to optimize device parameters such as durability, waveguide thickness, solar cell size, cell placement, and growing environment.

### Data Availability

The experimental data used to support the findings of this study are included within the supplementary information file(s) (available here).

### Conflicts of Interest

The authors declare that there is no conflict of interest regarding the publication of this paper.

### Acknowledgments

The authors give special thanks to Bruce Wittmershaus, Ph.D., for proof reading this article. Materials and summer researchers that supported this research were paid for by Allegheny College.

### Supplementary Materials

All data presented in this article are contained in the supplementary file titled “Flexible Front-Facing LSC Data.xls.” Data for Figures 4–9 are contained on spreadsheets labeled by their respective figures. For more information about this file, feel free to contact the corresponding author. (*Supplementary Materials*)

### References

- [1] IRENA, *Renewable Power Generation Costs in 2017*, International Renewable Energy Agency, 2018.
- [2] G. Kavlak, J. McNerney, and J. E. Trancik, “Evaluating the causes of cost reduction in photovoltaic modules,” *Energy Policy*, vol. 123, pp. 700–710, 2018.
- [3] SEIA and Wood Mackenzie Power & Renewables, *U.S. Solar Market Insight*, Solar Energy Industries Association, 2018.
- [4] IEA, *Renewables 2018 – Market Analysis and Forecast from 2018 to 2023*, International Energy Agency, 2018.
- [5] R. Chiabrando, E. Fabrizio, and G. Garnerio, “The territorial and landscape impacts of photovoltaic systems: definition of impacts and assessment of the glare risk,” *Renewable and Sustainable Energy Reviews*, vol. 13, no. 9, pp. 2441–2451, 2009.
- [6] R. R. Hernandez, S. B. Easter, M. L. Murphy-Mariscal et al., “Environmental impacts of utility-scale solar energy,” *Renewable and Sustainable Energy Reviews*, vol. 29, pp. 766–779, 2014.
- [7] R. Lakhani, G. Doluweera, and J. Bergerson, “Internalizing land use impacts for life cycle cost analysis of energy systems: a case of California’s photovoltaic implementation,” *Applied Energy*, vol. 116, pp. 253–259, 2014.
- [8] S. Ong, C. Campbell, P. Denholm, R. Margolis, and G. Heath, “Land-use requirements for solar power plants in the United States,” Tech. Rep., National Renewable Energy Lab. (NREL), Golden, CO, USA, 2013.
- [9] T. Tsoutsos, N. Frantzeskaki, and V. Gekas, “Environmental impacts from the solar energy technologies,” *Energy Policy*, vol. 33, no. 3, pp. 289–296, 2005.
- [10] F. Hyder, K. Sudhakar, and R. Mamat, “Solar PV tree design: a review,” *Renewable and Sustainable Energy Reviews*, vol. 82, pp. 1079–1096, 2018.
- [11] H.-M. Neumann, D. Schär, and F. Baumgartner, “The potential of photovoltaic carports to cover the energy demand of road passenger transport,” *Progress in Photovoltaics: Research and Applications*, vol. 20, no. 6, pp. 639–649, 2012.
- [12] T. Nordmann and L. Clavadetscher, “PV on noise barriers,” *Progress in Photovoltaics: research and applications*, vol. 12, no. 6, pp. 485–495, 2004.
- [13] A. Shekhar, V. K. Kumaravel, S. Klerks et al., “Harvesting roadway solar energy—performance of the installed infrastructure integrated PV bike path,” *IEEE Journal of Photovoltaics*, vol. 8, no. 4, pp. 1066–1073, 2018.
- [14] D. Chemisana, “Building integrated concentrating photovoltaics: a review,” *Renewable and Sustainable Energy Reviews*, vol. 15, no. 1, pp. 603–611, 2011.
- [15] R. Reisfeld and S. Neuman, “Planar solar energy converter and concentrator based on uranyl-doped glass,” *Nature*, vol. 274, no. 5667, pp. 144–145, 1978.
- [16] W. G. J. H. M. van Sark, K. W. J. Barnham, L. H. Slooff et al., “Luminescent solar concentrators - a review of recent results,” *Optics Express*, vol. 16, no. 26, pp. 21773–21792, 2008.
- [17] W. G. J. H. M. van Sark, “Luminescent solar concentrators – a low cost photovoltaics alternative,” *Renewable Energy*, vol. 49, pp. 207–210, 2013.
- [18] B. C. Rowan, L. R. Wilson, and B. S. Richards, “Advanced material concepts for luminescent solar concentrators,” *IEEE Journal of Selected Topics in Quantum Electronics*, vol. 14, no. 5, pp. 1312–1322, 2008.
- [19] C. Corrado, S. W. Leow, M. Osborn et al., “Power generation study of luminescent solar concentrator greenhouse,” *Journal of Renewable and Sustainable Energy*, vol. 8, no. 4, article 043502, 2016.
- [20] K. Kapsis and K. Kapsis, *Modelling, Design and Experimental Study of Semi-Transparent Photovoltaic Windows for Commercial Building Applications*, [Ph.D. thesis], Concordia University, 2016.
- [21] F. Meinardi, F. Bruni, and S. Brovelli, “Luminescent solar concentrators for building-integrated photovoltaics,” *Nature Reviews Materials*, vol. 2, no. 12, article 17072, 2017.
- [22] F. M. Vossen, M. P. J. Aarts, and M. G. Debije, “Visual performance of red luminescent solar concentrating windows in an office environment,” *Energy and Buildings*, vol. 113, pp. 123–132, 2016.
- [23] S. W. Leow, C. Corrado, M. Osborn, and S. A. Carter, “Monte Carlo ray-tracing simulations of luminescent solar concentrators for building integrated photovoltaics,” in *Proceeding of SPIE 8821, High and Low Concentrator Systems for Solar Electric Applications VIII*, 882103, San Diego, CA, USA, 2013.
- [24] C. Corrado, S. W. Leow, M. Osborn, E. Chan, B. Balaban, and S. A. Carter, “Optimization of gain and energy conversion

- efficiency using front-facing photovoltaic cell luminescent solar concentrator design,” *Solar Energy Materials and Solar Cells*, vol. 111, pp. 74–81, 2013.
- [25] B. Vishwanathan, A. H. M. E. Reinders, D. K. G. de Boer et al., “A comparison of performance of flat and bent photovoltaic luminescent solar concentrators,” *Solar Energy*, vol. 112, pp. 120–127, 2015.
- [26] S. Woei Leow, C. Corrado, M. Osborn, M. Isaacson, G. Alers, and S. A. Carter, “Analyzing luminescent solar concentrators with front-facing photovoltaic cells using weighted Monte Carlo ray tracing,” *Journal of Applied Physics*, vol. 113, no. 21, article 214510, 2013.
- [27] X. Sheng, L. Shen, T. Kim et al., “Doubling the power output of bifacial thin-film GaAs solar cells by embedding them in luminescent waveguides,” *Advanced Energy Materials*, vol. 3, no. 8, pp. 991–996, 2013.
- [28] J. Yoon, L. Li, A. V. Semichaevsky et al., “Flexible concentrator photovoltaics based on microscale silicon solar cells embedded in luminescent waveguides,” *Nature Communications*, vol. 2, no. 1, p. 343, 2011.
- [29] Y. Zhang, S. Sun, R. Kang et al., “Polymethylmethacrylate-based luminescent solar concentrators with bottom-mounted solar cells,” *Energy Conversion and Management*, vol. 95, pp. 187–192, 2015.
- [30] J. Zhang, M. Wang, Y. Zhang et al., “Optimization of large-size glass laminated luminescent solar concentrators,” *Solar Energy*, vol. 117, pp. 260–267, 2015.
- [31] M. Buffa, S. Carturan, M. G. Debije, A. Quaranta, and G. Maggioni, “Dye-doped polysiloxane rubbers for luminescent solar concentrator systems,” *Solar Energy Materials and Solar Cells*, vol. 103, pp. 114–118, 2012.
- [32] K. A. Colby, J. J. Burdett, R. F. Frisbee, L. Zhu, R. J. Dillon, and C. J. Bardeen, “Electronic energy migration on different time scales: concentration dependence of the time-resolved anisotropy and fluorescence quenching of Lumogen Red in poly(methyl methacrylate),” *The Journal of Physical Chemistry A*, vol. 114, no. 10, pp. 3471–3482, 2010.
- [33] G. Maggioni, A. Campagnaro, S. Carturan, and A. Quaranta, “Dye-doped parylene-based thin film materials: application to luminescent solar concentrators,” *Solar Energy Materials and Solar Cells*, vol. 108, pp. 27–37, 2013.
- [34] M. E. Loik, S. A. Carter, G. Alers et al., “Wavelength-selective solar photovoltaic systems: powering greenhouses for plant growth at the food-energy-water nexus,” *Earth’s Future*, vol. 5, no. 10, pp. 1044–1053, 2017.
- [35] J. D. White, “Alternative Energy: Making the controlled environment a greener, more stable place,” *Inside Grower*, pp. 18–20, 2017.
- [36] AZoCleantech, “Solar greenhouses can generate electricity & grow crops,” 2018, <https://www.azocleantech.com/news.aspx?newsID=24326>.
- [37] Z. Cai, W. Qiu, G. Shao, and W. Wang, “A new fabrication method for all-PDMS waveguides,” *Sensors and Actuators A: Physical*, vol. 204, pp. 44–47, 2013.
- [38] C. H. Chou, J. K. Chuang, and F. C. Chen, “High-performance flexible waveguiding photovoltaics,” *Scientific Reports*, vol. 3, no. 1, p. 2244, 2013.
- [39] C.-H. Chou, M.-H. Hsu, and F.-C. Chen, “Flexible luminescent waveguiding photovoltaics exhibiting strong scattering effects from the dye aggregation,” *Nano Energy*, vol. 15, pp. 729–736, 2015.
- [40] S. F. H. Correia, P. P. Lima, E. Pecoraro et al., “Scale up the collection area of luminescent solar concentrators towards metre-length flexible waveguiding photovoltaics,” *Progress in Photovoltaics: Research and Applications*, vol. 24, no. 9, pp. 1178–1193, 2016.
- [41] C. Tummeltshammer, A. Taylor, A. J. Kenyon, and I. Papakonstantinou, “Flexible and fluorophore-doped luminescent solar concentrators based on polydimethylsiloxane,” *Optics Letters*, vol. 41, no. 4, pp. 713–716, 2016.
- [42] M. Gajic, F. Lisi, N. Kirkwood, T. A. Smith, P. Mulvaney, and G. Rosengarten, “Circular luminescent solar concentrators,” *Solar Energy*, vol. 150, pp. 30–37, 2017.
- [43] N. Steinbruck, M. Konemann, and G. Kickelbick, “Effect of polysiloxane encapsulation material compositions on emission behaviour and stabilities of perylene dyes,” *RSC Advances*, vol. 8, no. 32, pp. 18128–18138, 2018.
- [44] G. Griffini, M. Levi, and S. Turri, “Thin-film luminescent solar concentrators: a device study towards rational design,” *Renewable Energy*, vol. 78, pp. 288–294, 2015.
- [45] M. A. Green, Y. Hishikawa, W. Warta et al., “Solar cell efficiency tables (version 50),” *Progress in Photovoltaics: Research and Applications*, vol. 25, no. 7, pp. 668–676, 2017.
- [46] R. Bose, D. J. Farrell, A. J. Chatten, M. Pravettoni, A. Buchtemann, and K. W. J. Barnham, “Novel configurations of luminescent solar concentrators,” in *Proceedings of the 22nd European Photovoltaic Solar Energy Conference and Exhibition*, pp. 210–214, Milan, 2007.
- [47] H. K. Lichtenthaler, “[34] Chlorophylls and carotenoids: pigments of photosynthetic biomembranes,” *Methods in Enzymology*, vol. 148, pp. 350–382, 1987.

## Research Article

# Design and Analysis of a Stand-Alone PV System for a Rural House in Pakistan

Amjad Iqbal  and M. Tariq Iqbal 

*ECE, Faculty of Engineering and Applied Sciences, Memorial University of Newfoundland, Canada*

Correspondence should be addressed to M. Tariq Iqbal; [tariq@mun.ca](mailto:tariq@mun.ca)

Received 29 August 2018; Revised 8 February 2019; Accepted 7 March 2019; Published 23 April 2019

Guest Editor: Mattia De Rosa

Copyright © 2019 Amjad Iqbal and M. Tariq Iqbal. This is an open access article distributed under the Creative Commons Attribution License, which permits unrestricted use, distribution, and reproduction in any medium, provided the original work is properly cited.

In this paper, thermal modeling of a typical rural house in Pakistan has been done using BEopt, to determine the hourly load profile. Using the load data, the design of a stand-alone PV system has been completed using HOMER Pro. The designed system consists of a 5.8 kW PV with eight batteries of 12 V, 255 Ah, and a 1.4 kW inverter. The system analyses show that such system can support mainly lighting and appliance load in a rural house. The dynamic model of the designed system has been simulated in MATLAB-Simulink. Perturbation and observation-based algorithm has been used for maximum power extraction from PV. Simulation results indicate that the system can provide a stable voltage and frequency for the domestic load. The method and analysis presented here can be used for the PV system design for other parts of the world.

## 1. Introduction

In this case study, a rural house in Pakistan has been considered for the load profile, PV sizing, and system design. It was selected because most of the remote communities of underdeveloped countries like Pakistan have high solar resource but are isolated from the main grid, and they face long hours of load shedding. The system analysis, sizing, and current per kilowatt hour cost encourage renewable energy and PV system in other parts of the world specifically in the countries of South Africa and South Asia which are rich in solar resource and have the insufficient electric supply. Therefore, this study will help in implementing small PV systems to meet the domestic load demand of the people living in the solar irradiance-rich areas of the world.

The efficiency and output power of PV depend upon the solar irradiance, location, face angle of the PV panel, type of PV (monocrystalline, polycrystalline, microamorphous silicon, and amorphous silicon), and the efficiency of the components, but the available solar irradiance and location play a significant role [1]. Another study [2] showed that the hybrid system of PV and diesel would be viable than a stand-alone PV system. The latest research has led to a

significant improvement in the efficiency of the PV system to harness the clean energy [3]. Due to this, the stand-alone PV systems are becoming more ubiquitous for the electrification of off-grid communities and other projects like the water pumping system [4–6], and in this growing trend, this study will be helpful for small PV system designing and sizing.

Pakistan is a developing country, and it is facing a power crisis for more than twenty years. The gap in power generation (18,000 MW) and demand (25,000 MW) is continuously increasing, because load shedding hours in the rural areas are increasing every year and now have reached up to 6 h in winter and 10 h in summer [7–10]. To meet the urban and industrial sector power demand, the power of the rural area is cut down resulting more suffering of rural people than urban people. More than 50% of the population of Pakistan is living in rural areas, and daily power outage is one of the main reasons for the low GDP [11]. The sufferings of the rural people and some assumptions made in the sizing of such system [12] are the driving forces for this research work.

If an alternate system is designed for the rural people, it would not only reduce their worries but will also make improvements in the country's GDP. Fortunately, Pakistan is rich in solar energy potential, and according to Jamal and

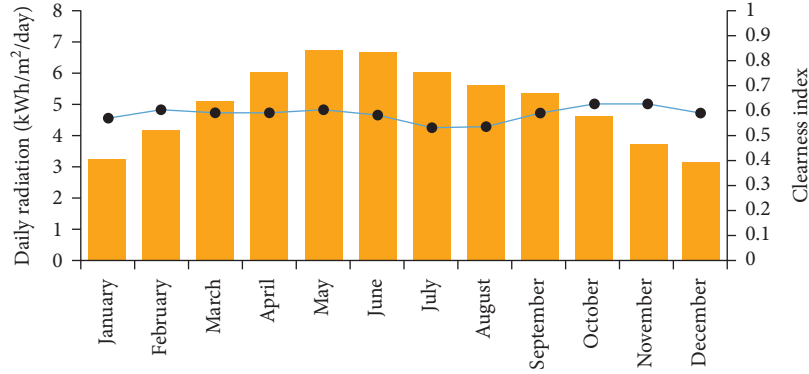


FIGURE 1: Solar energy potential at the selected location.

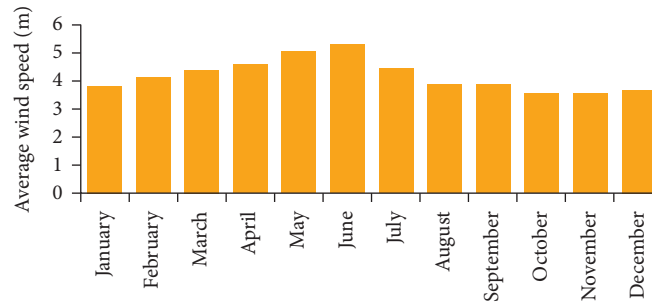


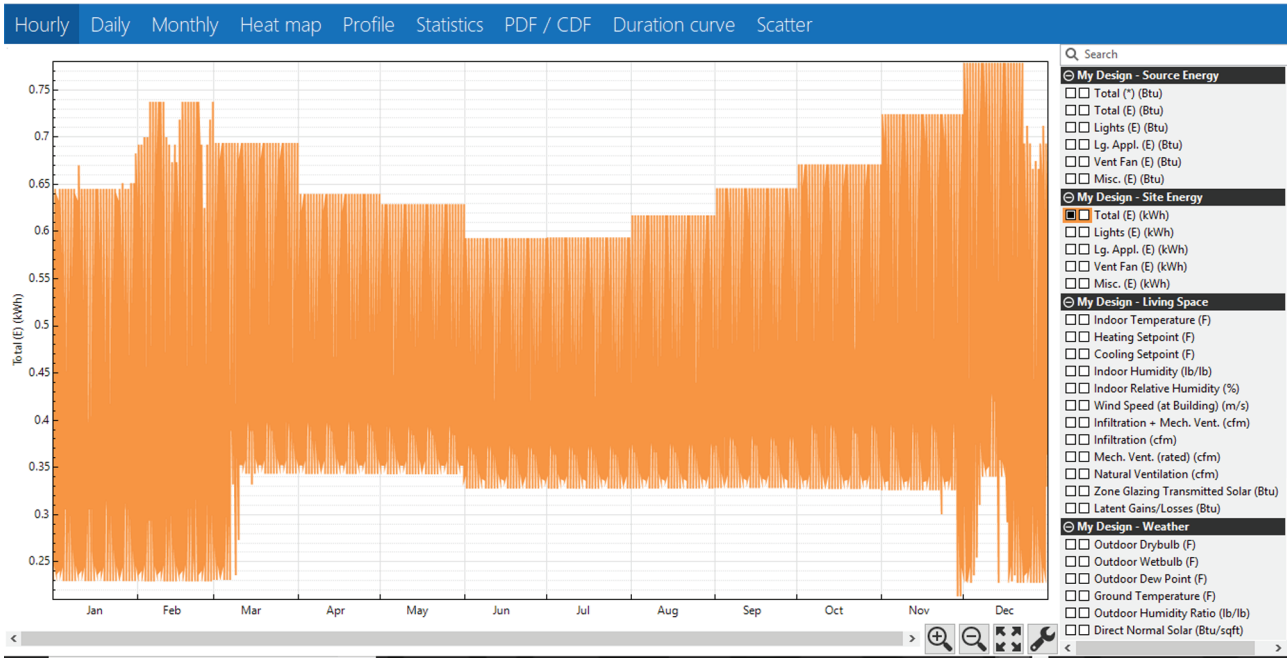
FIGURE 2: Wind speed data for the selected location (50 m).

TABLE 1: Load estimate of a typical rural house in Pakistan.

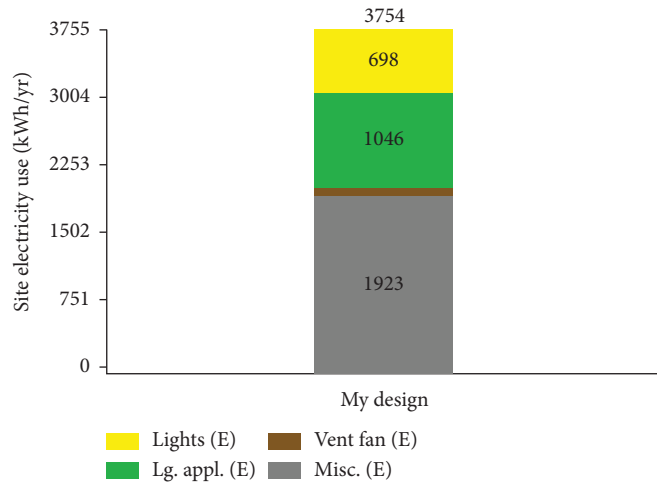
Load	Lights	Fans	Refrigerator	TV (17")	Miscellaneous load
Power rating	25 W	75 W	200 W	150 W	
# of items	4	3	1	1	
Total power	100 W	225 W	200 W	150 W	100 W

Hohmeyer and Stackhouse et al. [13, 14], the annual solar irradiance ranges from 4.0 to 5.28 kWh/m<sup>2</sup>/day. Figure 1 shows the average monthly sunshine of 250 h for the chosen site. Although, many papers like [13, 15–17] have been written on this topic, most of them address generic issues of the PV system, and even in [12], an attempt has been made to size and propose a PV system for a typical house and a load of a house has been considered to be 5 kWh/day (1800 kWh/year). Further, the proposed system is undersized, and idealistic conditions have been assumed like daily solar irradiance would be greater than 5 kWh/m<sup>2</sup>/day and intermittence of weather conditions and bad weather backup has not been taken into considerations. We present complete thermal modeling of a typical house done in BEopt to observe the hourly load profile for one year, and according to that, the system sizing has been completed. Using HOMER Pro, an optimized and low-cost system has been selected which gives energy at the rate of \$0.19/kWh and the system design has been explained in the coming sections. Simulations of a stand-alone PV system have been completed in Simulink. In the proposed system's simulations, a perturbation and observation-based maximum power point tracking (MPPT) algorithm has been implemented, and the battery bank

protection against under/overvoltage has been carried out. MPPT is the operating state of the PV at which it delivers maximum power to a resistive load [18]. Before opting the PV system, the study of other available energy resources was also done. Annual wind speed data for the selected site has been shown in Figure 2. The average annual wind speed is not more than 4.15 m/s [14], because wind energy use was eliminated. The rural areas in Pakistan are not rich in geothermal energy source because geotemperature varies by only 3–3.5°C for the depth of 100 m [19–21]. Similarly, ocean energy could not be considered because more than 50% of the population of Pakistan lives in the Punjab Province which is more than 500 km away from the ocean. A brief analysis of available renewable energy resources for a typical house and hourly energy consumption for one year has been estimated in Section 2. Section 3 explains the HOMER Pro-based system sizing for the house including the size of the proposed PV system considering 18% efficiency. A single inverter and a battery bank which can provide backup for more than two days in abnormal weather conditions have been selected. Simulink-based simulations have been explained in Section 4. The last section gives the conclusion and analysis of the proposed system.



(a)



(b)

FIGURE 3: (a) Hourly load flow data of the house for a typical year. (b) Annual energy consumption of the house by different types of load (lights, large appliances, ventilation fans, and miscellaneous load).

## 2. Estimation of the Hourly Load and Annual Energy Consumption of the House

The selected house is in a remote community of Punjab Province and in the outskirts of district Faisalabad with the coordinates of  $31^{\circ}13'N$  and  $73^{\circ}24'E$ . The thermal modeling has been completed by estimating the residential load; the results of annual energy consumption from BEopt were compared with the utility bill, and a minor variation of less than 4% was observed.

In the rural areas, people do not use electric heaters or air conditioner for heating/cooling purposes and for cooking they use petroleum gas or wood. The typical load is very small, and an approximated load of a typical house is 7-

9 kWh/day according to the BEopt results. Here, in system sizing backup, storage has been assumed to be 10 kWh/day. Load of Table 1 was entered in BEopt, which was collected by counting the number of active appliances and their nameplate power consumption. The hourly load profile for a year was generated and has been shown in Figure 3(a) which shows that the energy consumption is relatively higher in the months of February, November, and December due to longer nights. Figure 3(b) shows the total kWh consumption round the year by different load types (lights, large appliances, ventilation fans, and other miscellaneous appliances). Miscellaneous load seems too high compared to others because it accommodates all different types of load other than the list presented in Table 1.

Sensitivity Cases											
Architecture						Cost			System		
SPR-E20 (kW)	SSIG 12 255	Cybo1000N (kW)	Dispatch	COE (\$)	NPC (\$)	Operating cost (\$/yr)	Initial capital (\$)	Ren Frac (%)	Total Fuel (L/yr)	Capital Cost (\$)	SPF
5.88	8	1.40	CC	\$0.199	\$9,650	\$332.39	\$5,353	100	0	1,763	

Optimization Results											
Architecture						Cost			System		
SPR-E20 (kW)	SSIG 12 255	Cybo1000N (kW)	Dispatch	COE (\$)	NPC (\$)	Operating cost (\$/yr)	Initial capital (\$)	Ren Frac (%)	Total Fuel (L/yr)	Capital Cost (\$)	SPF
5.88	8	1.40	LF	\$0.199	\$9,650	\$332.39	\$5,353	100	0	1,763	
5.88	8	1.40	CC	\$0.199	\$9,650	\$332.39	\$5,353	100	0	1,763	
5.87	8	1.42	LF	\$0.199	\$9,652	\$332.56	\$5,353	100	0	1,761	
5.87	8	1.42	CC	\$0.199	\$9,652	\$332.56	\$5,353	100	0	1,761	
5.91	8	1.37	LF	\$0.199	\$9,653	\$332.20	\$5,359	100	0	1,773	
5.91	8	1.37	CC	\$0.199	\$9,653	\$332.20	\$5,359	100	0	1,773	

FIGURE 4: HOMER sizing and optimization results.

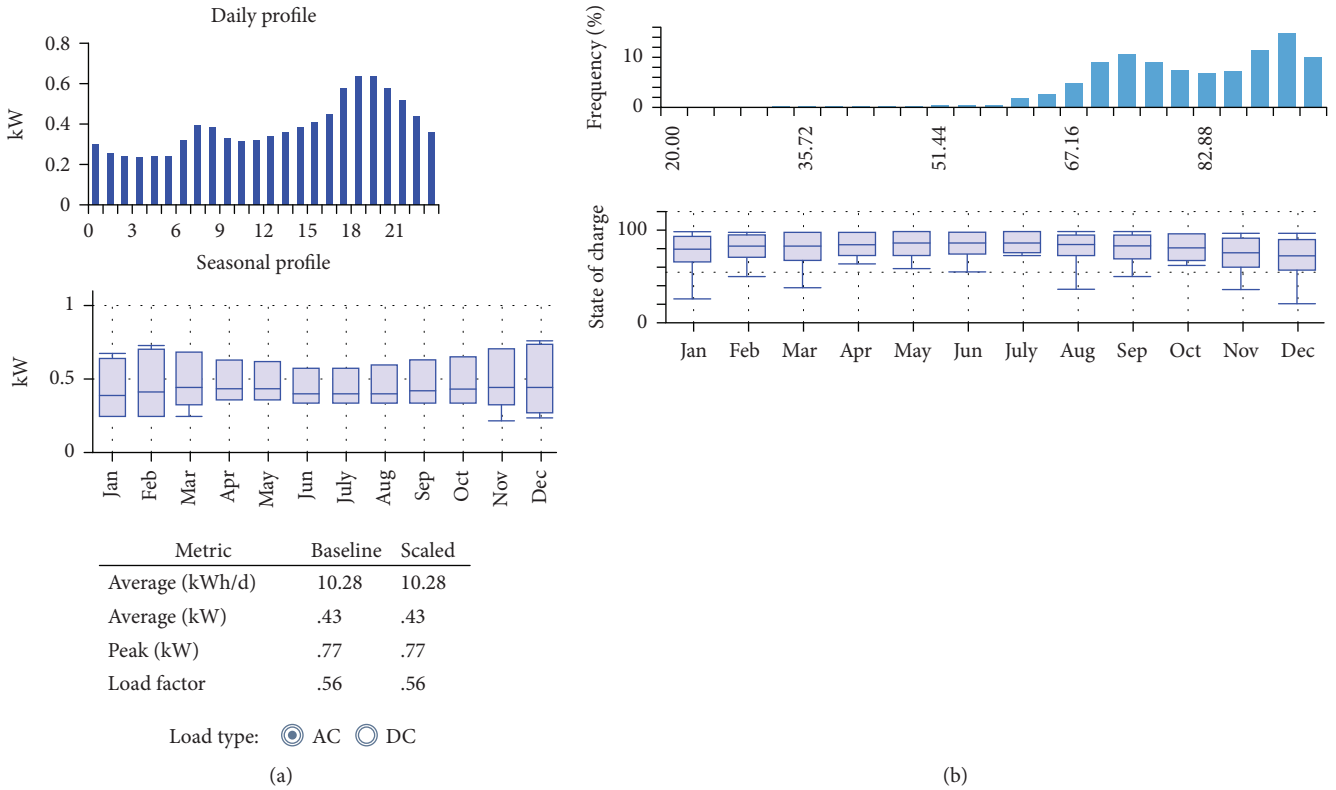


FIGURE 5: (a) Hourly load profile for a typical day and average demand of each month. (b) Battery bank discharge frequency and the depth of discharge.

TABLE 2: Project estimated costs [24].

Component	PV	Converter	Battery
Rating of each component	327 W	1.4 kW	SSIG 12 V, 255 Ah
Required # of components	18	1	8
Final rating	5.886 kW	1.4 kW	48 V, 510 Ah
Cost/unit	\$173	\$180	\$426
Total cost	\$3114	\$180	\$3408

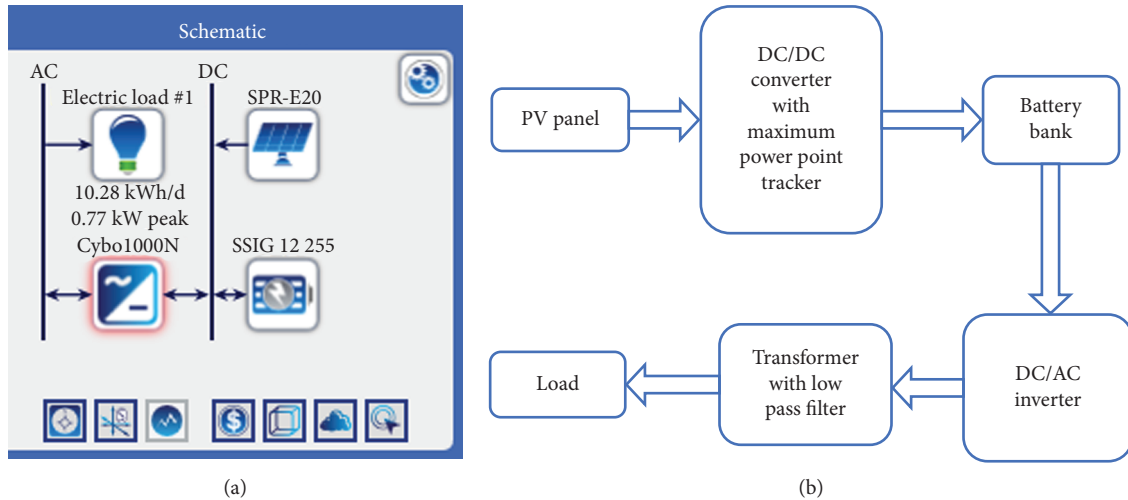


FIGURE 6: (a) System structure with integrated subblocks. (b) Flow chart of the system structure with subblocks followed in Simulink simulations.

### 3. System Sizing and Optimization

The desired system sizing was completed in HOMER Pro; the data for solar irradiance was downloaded from [22], and HOMER results have been shown in Figure 4. In results, more than 3000 different combinations consisting of a different number of PV panels and battery banks were calculated in HOMER and, finally, the chosen system was found the most economical considering the factors such as initial capital cost, cost/kWh, net present cost, unmet load, excess electricity generation, and the efficiency of the system. According to the optimized results, the PV panels of SunPower 5.88 kW, 8 batteries of SSIG 12 V, 255 Ah (two strings of 48 V), and a converter of 1.4 kW will be enough to meet the load. For PV, SunPower polycrystalline has been selected due to the economical reasons despite its relatively less efficiency (18%) as compared to the silicon monocrystalline PV panels (20%) [23]. The above proposed system gives the power backup for 47 h for bad weather conditions as well and has minimum excess electricity. The power inverter is 1.4 kW, and it has been sized based upon the peak demand of AC load which is not more than 800 W during peak time. The required PV panel was sized considering the factors of load demand, required power backup, irradiance, etc. Therefore, there is a difference between PV panel size (5.8 kW) and the converter rating (1.4 kW). When the PV output is sufficient to meet the load demand, the battery bank will be in floating state and will only be discharged during night time or when the PV output becomes insufficient to meet load demand. Further, the average daily energy consumption of the house is 10.3 kWh; therefore, the proposed battery bank size determined in HOMER size optimization will be sufficient to give backup of 47 h for bad weather conditions. In actual system sizing, a safety factor of 1.3 times has also been included to protect against overloading or withstand the surges and the efficiency of the PV system has been taken 18% according to the nameplate of SunPower.

The load profile and the battery state of charge have been shown in Figures 5(a) and 5(b), respectively. Figure 5(a)

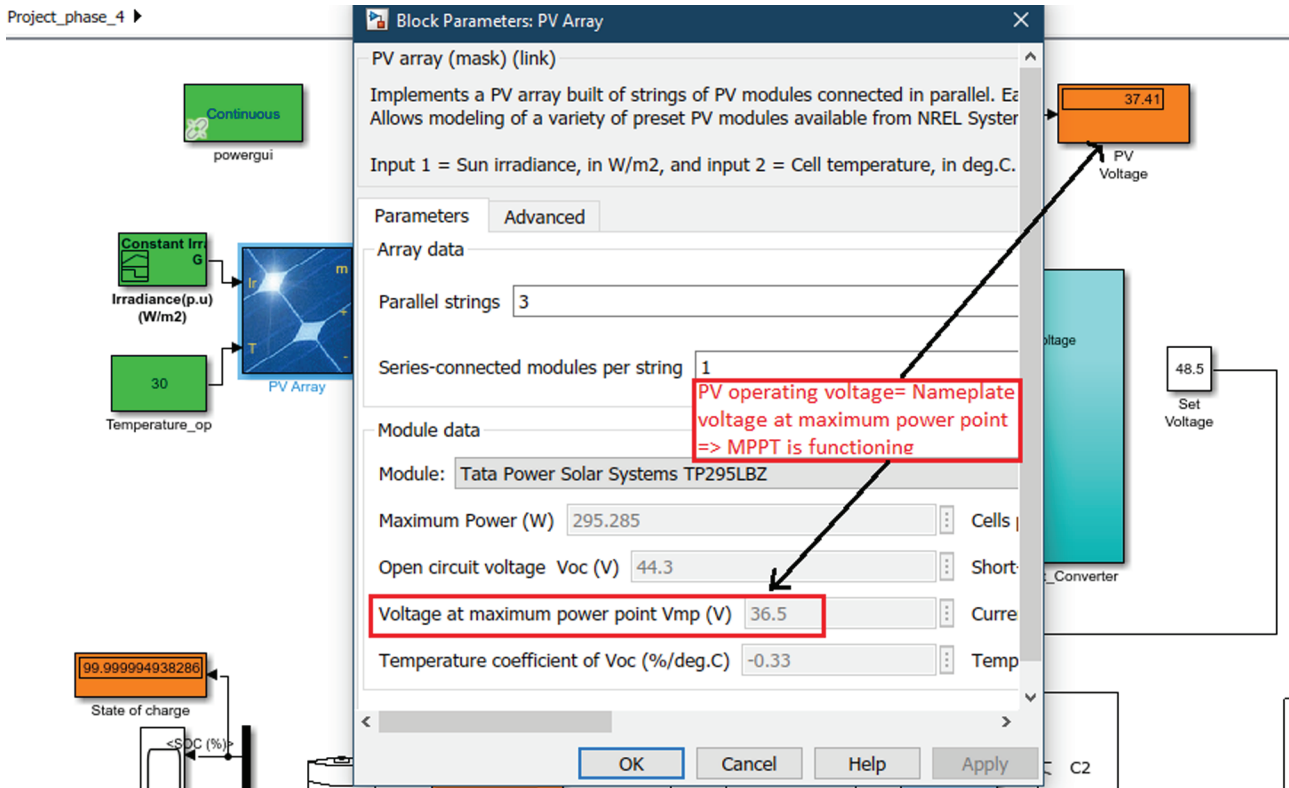
shows the 24-hour load profile with peak hours of early morning and evening as observed in our real system, and the average daily demand is not more than 10.3 kWh. Figure 5(b) shows the storage state of charge and the percentage of discharge, and depth of discharge is never worse than 25%. Table 2 shows the information about the rating and cost of the system components. Most of the data about components' cost were collected from [24]. It includes 70% of replacement cost, and it can be seen that the overall project does not cost more than \$9650.

The site does not have sufficient sources of wind and geothermal energy as indicated in the literature review; therefore, those sources have not been included in HOMER sizing and optimizations. The chosen site has no obstacles or trees to cause the shadow on the PV system; therefore, shadow and its impact have been ignored.

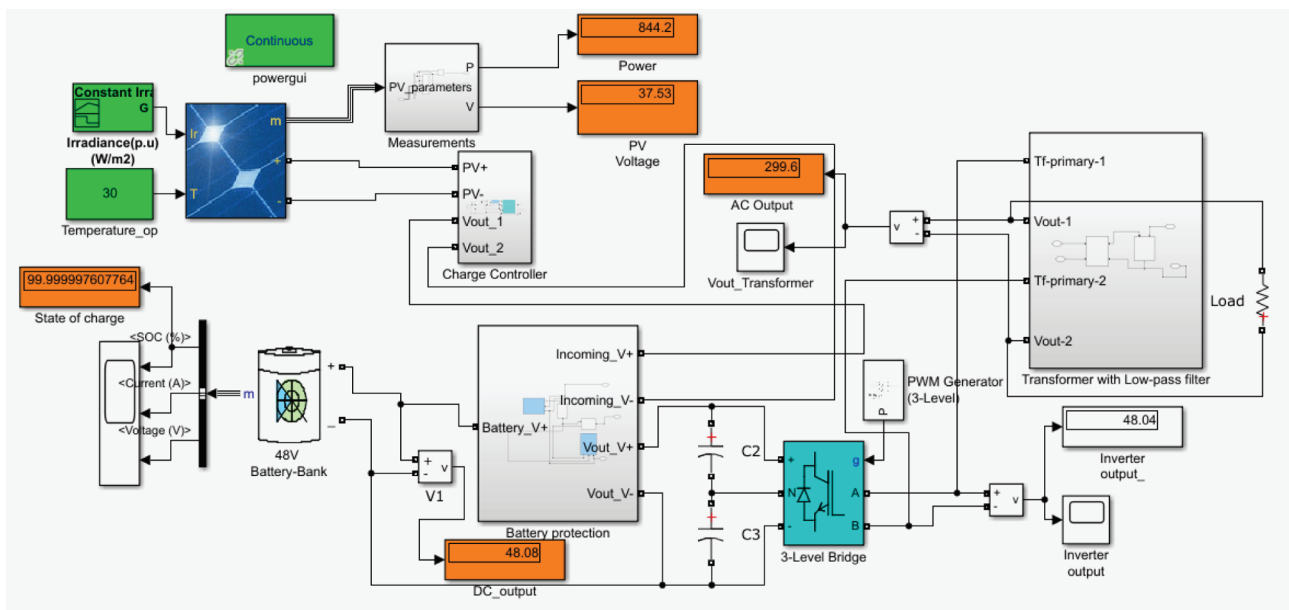
### 4. Proposed System Simulations in Simulink

The system block diagram has been shown in Figure 6. Figure 6(a) shows the block diagram of the system in which the solar panel with the maximum power point tracker (MPPT) is connected with the DC bus. The block of the battery bank which also has the charge controller and under/over-voltage protection is connected with the same DC bus. The third block in this figure is the Cybo1000N converter which not only converts DC into AC but also ensures the power quality (reduce the harmonics) and links the DC and AC buses. The simulations of the proposed system have been completed in Simulink following the block diagram shown in Figure 6(b) which is the extension of the blocks shown in Figure 6(a).

In the Simulink simulations, the PV system output is fed to the block of the DC/DC converter with a controller. The algorithm of the maximum power point tracker (MPPT) has been implemented in the same block to control the duty cycle of the converter. It maintains the output DC voltage equal to 48 V and feeds to the battery bank. Under normal operating conditions (when the PV output is enough to meet



(a)



(b)

FIGURE 7: (a) Output voltage of PV when the system is operating at maximum power point (MPP) under MPPT. (b) Simulink simulations for the complete system.

load demand), the battery bank will be in a floating state. Therefore, its state of charge shown in Figure 7 shows that it fully charged. Single-phase six-step inverter which operates with a switching frequency of 5 kHz is connected with the battery bank. Its output is a six-step AC waveform with 50 Hz frequency which is the standard power system frequency in Pakistan. The voltage level of the six-step AC form

is boosted to 212 V RMS (300 V peak) by a single-phase transformer which also has a filter on secondary winding to reduce the harmonics.

To track the maximum power point for PV, perturbation and observation-based algorithm has been implemented. It was opted out of many other algorithms because of its simplicity and quick response and is free

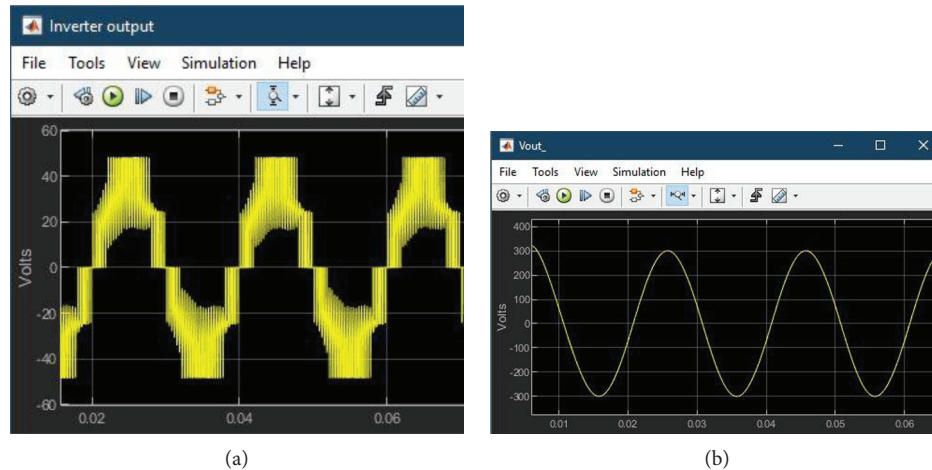


FIGURE 8: (a) Output of the 6-step inverter (low-voltage side). (b) Final output of 50 Hz, 212 V RMS for the AC load (high-voltage side).

from derivatives and integrals like other algorithms. In Simulink, the battery protection unit protects the battery from deep discharging and also protects from overvoltage for any abnormal condition. The battery protection units for the battery bank and system are based upon the comparison of the output voltage and the reference Zener voltage, and based upon that, a decision is made whether to keep the system connected or turned off. The design calculations for the buck-boost converter were completed using equation (1) [25], and the filter design was completed following [26]. In the following equations,  $D$  is for duty cycle and  $f$  is for the switching frequency:

$$L \geq \frac{(1-D)^2}{2f} R, \quad (1)$$

$$C = (2\pi f)^2 L.$$

The complete Simulink diagram has been shown in Figures 7(a) and 7(b). Figure 7(a) shows the output voltage of PV when MPPT is controlling its operating point. In Figure 7(a), the voltage is 37.5 V and with time MPPT fixes the output exactly equal to the nameplate value of the PV to get maximum power. Figure 7(b) shows the complete Simulink diagram of the system which gives the desired output and corroborates the system validations. The simulation results have been shown in Figure 8, where Figure 8(a) shows the output of a six-step inverter and Figure 8(b) shows the final output of the system which is 212 V RMS (600 V peak-to-peak voltage) with the standard frequency of 50 Hz. This simulation identifies all electrical parts required for the system and can be used to study the impact of changing inputs on the output voltage.

## 5. Conclusion

For a typical house of the rural area in Pakistan, the complete thermal modeling, sizing, and optimization of a stand-alone PV system with detailed cost calculations have been presented in this paper. The designed system consists of 5.8 kW PV, eight batteries of 12 V and 255 Ah, and a

1.4 kW inverter, and overall, it costs \$9650 and produces electricity at \$0.199/kWh. This research presents a detailed procedure to design a PV system for remote locations where grid supply is not possible or economically viable. Following this method, one can estimate the load, size a system, simulate the system, and determine the expected performance. Therefore, this study seems potentially helpful in designing a stand-alone PV system.

## 6. Future Work

It could be seen that the battery bank requires a significant capital cost which overall affects the system economical viability. In the future, a large scale implementation of the PV system study could be done to explore the implementation of other combinations for energy storage systems along with the battery bank, e.g., compressed air, hydrogen gas, flywheel, pumped hydro, and other options like these. A hybrid and cheaper energy storage system will prove helpful in harnessing clean and cheap energy.

## Data Availability

The data used to support the findings of this study are available from the corresponding author upon request.

## Conflicts of Interest

The authors of this work declare that all used software and devices were selected on professional basis. Furthermore, the authors certify that there is no actual or potential conflict of interest in relation to this article.

## Acknowledgments

This research was funded by the Natural Sciences and Engineering Research Council (NSERC) of Canada. The authors would like to acknowledge the financial support of the NSERC and the technical support of friends, family, and the Memorial University of Newfoundland.

## References

- [1] C. R. Charan, A. J. Laxmi, and P. Sangeetha, "Optimized energy efficient solution with stand alone PV system," *MAT-TER: International Journal of Science and Technology*, vol. 3, no. 1, pp. 16–27, 2017.
- [2] H. Rezzouk and A. Mellit, "Feasibility study and sensitivity analysis of a stand-alone photovoltaic–diesel–battery hybrid energy system in the north of Algeria," *Renewable and Sustainable Energy Reviews*, vol. 43, pp. 1134–1150, 2015.
- [3] Global CCS Institute, "Renewable generation scenarios from 2020," <https://hub.globalccsinstitute.com/publications/renewable-energy-review/4-renewable-generation-scenarios-2020>.
- [4] B. Bogno, J. P. Sawicki, P. Petit et al., "230 V<sub>DC</sub> elementary block in off-grid PV systems," *Sustainable Energy Technologies and Assessments*, vol. 29, pp. 1–11, 2018.
- [5] K. Rahra, D. Rekioua, T. Rekioua, and S. Bacha, "Photovoltaic pumping system in Bejaia climate with battery storage," *International Journal of Hydrogen Energy*, vol. 40, no. 39, pp. 13665–13675, 2015.
- [6] A. Mohammedi, D. Rekioua, and N. Mezzai, "Experimental study of a PV water pumping system," *Journal of Electrical Systems*, vol. 9, no. 2, pp. 212–222, 2013.
- [7] K. Kiani, *Loadshedding Rears Its Head as Fuel Stocks Dip*, DAWN, 2018, <https://www.dawn.com/news/1405137>.
- [8] International Renewable Energy Agency, *Renewable Readiness Assessment Pakistan*, IRENA, Abu Dhabi, 2018.
- [9] The DAWN, "Load-shedding despite megawatts7, July 2018," <https://www.dawn.com/news/1405341>.
- [10] National Transmission and Despatch Company, *Power System Statistics 2014-2015*, NTDC, Lahore, 2015.
- [11] G. Saghir and S. Malik, "Estimating monetary policy reaction function of the State Bank of Pakistan," August 2018, [http://pu.edu.pk/images/journal/pesr/PDF-FILES/7-v55\\_1\\_17.pdf](http://pu.edu.pk/images/journal/pesr/PDF-FILES/7-v55_1_17.pdf).
- [12] M. Ali, A. Yousaf, and F. G. Seharan, "Feasibility evaluation of stand-alone photovoltaic systems for residential loads," in *2018 9th International Renewable Energy Congress (IREC)*, pp. 1–4, Hammamet, Tunisia, March 2018.
- [13] N. Jamal and O. Hohmeyer, "Solar resources' potential role in the development of renewable based electric power system by 2050: the case of Pakistan prospects of solar in Pakistan," in *2014 International Conference on Energy Systems and Policies (ICESP)*, pp. 1–7, Islamabad, Pakistan, November 2014.
- [14] P. W. Stackhouse, D. Westberg, J. M. Hoell, W. S. Chandler, and T. Zhang, "Atmospheric Science Data Center," *Surface Meteorology and Solar Energy*, vol. 3.1.2, pp. 9–24, 2013, Release 6.0 Methodology.
- [15] R. S. Farswan, H. Khan, and B. G. Fernandes, "A low cost reliable stand-alone photo-voltaic system," in *2014 IEEE International Conference on Power Electronics, Drives and Energy Systems (PEDES)*, Mumbai, India, December 2014.
- [16] M. F. Aziz and N. Abdulaziz, "Prospects and challenges of renewable energy in Pakistan," in *2010 IEEE International Energy Conference*, pp. 161–165, Manama, Bahrain, December 2010.
- [17] G. N. Prodromidis and F. A. Coutelieres, "A comparative feasibility study of stand-alone and grid connected RES-based systems in several Greek Islands," *Renewable Energy*, vol. 36, no. 7, pp. 1957–1963, 2011.
- [18] A. Daniela, P. Ejnar, and W. Henrik, "Models for a stand-alone PV system," *Forskningssenter Risoe. Risoe-R*, vol. 1219, no. 1219, 2001.
- [19] U. Younas, B. Khan, S. M. Ali et al., "Pakistan geothermal renewable energy potential for electric power generation: a survey," *Renewable and Sustainable Energy Reviews*, vol. 63, pp. 398–413, 2016.
- [20] N. Alam Zaigham, Z. Alam Nayyar, and N. Hisamuddin, "Review of geothermal energy resources in Pakistan," *Renewable and Sustainable Energy Reviews*, vol. 13, no. 1, pp. 223–232, 2009.
- [21] I. A. Gondal, S. A. Masood, and M. Amjad, "Review of geothermal energy development efforts in Pakistan and way forward," *Renewable and Sustainable Energy Reviews*, vol. 71, pp. 687–696, 2017.
- [22] R. Affolter, *Pakistan - Solar Radiation Measurement Data (2014 - 2017)*, World Bank Group, Islamabad, 2018.
- [23] S. Das and A. K. Akella, "Power flow control of PV-wind-battery hybrid renewable energy systems for stand-alone application," *International Journal of Renewable Energy Research*, vol. 8, no. 1, 2018.
- [24] <https://www.solaris-shop.com/trojan-signature-ssig-12-255-flooded-12v-229ah-battery/>.
- [25] G. Stahl, M. Rodriguez, and D. Maksimovic, "A high-efficiency bidirectional buck-boost DC-DC converter," in *2012 Twenty-Seventh Annual IEEE Applied Power Electronics Conference and Exposition (APEC)*, pp. 1362–1367, Orlando, FL, USA, February 2012.
- [26] R. W. Erickson and D. Maksimovic, *Fundamentals of Power Electronics*, Springer US, New York, NY, USA, 2nd edition, 2001.

## Research Article

# Performance Modelling of Dual Air/Water Collector in Solar Water and Space Heating Application

Viacheslav Shemelin  and Tomas Matuska 

University Centre for Energy Efficient Buildings, Czech Technical University in Prague, Trinecka 1024,  
273 43 Bustehrad, Czech Republic

Correspondence should be addressed to Viacheslav Shemelin; [viacheslav.shemelin@cvut.cz](mailto:viacheslav.shemelin@cvut.cz)

Received 30 November 2018; Revised 24 January 2019; Accepted 6 February 2019; Published 18 April 2019

Guest Editor: Paolo Conti

Copyright © 2019 Viacheslav Shemelin and Tomas Matuska. This is an open access article distributed under the Creative Commons Attribution License, which permits unrestricted use, distribution, and reproduction in any medium, provided the original work is properly cited.

In the present work, the detailed mathematical model of a dual air/water solar collector (DAWC) has been developed and experimentally verified. To demonstrate the application of the DAWC, three buildings with different energy performance levels and three building locations were chosen in analyzed case studies. Four solar collector systems were compared with one another. The solar yield of the described systems was determined by simulation using the detailed theoretical model of DAWC. The results indicate that in the case of combining a domestic hot water preparation system and recirculating-air heating system based on DAWC, it is possible to achieve up to 30% higher solar energy yield compared to a conventional solar domestic hot water preparation system dependent on climate and building performance.

## 1. Introduction

Flat-plate solar collectors are probably the most fundamental and most studied technology for solar-power domestic hot water systems. Flat-plate collector technology has evolved over 60 years. Products on sale today have been proven to be durable and reliable, and therefore, collectors are considered as a fairly mature technology. However, even if this device has reached a good technological level and position in the market, the scientific and technological world has shown a constant attention to improve the energy performance of the collector. The ways of increasing the energy performance generally can be divided into two categories: the use of new technologies, materials, and components and the combination of already existing solar utilization technologies in one facility (hybrid collector).

The objective of combining two different solar utilization technologies is to make the application field for a given collector wider and increase the potential energy gain from the area occupied by the collector. A known example of such a multipurpose collector is a photovoltaic-thermal solar collector combining PV technology and a solar thermal collector.

The present study is focused on the dual-fluid solar collector, combining the air and liquid solar collectors. The idea of combining both types of technology in a dual air/water solar collector (DAWC) is not new. It has emerged from the typical situation in moderate and cold climatic zones, where solar radiation is sufficient for the preparation of hot water for households needs (50-60°C) during summer, whereas the output temperatures from solar collectors during winter generally do not reach values higher than 30°C; however, it can be sufficient, for example, for preheating fresh air. Such an integrated design allows increasing the annual energy yield of a solar system and maximizing the operating time, which makes it more cost-effective than the conventional solar water or air systems.

A number of researchers have studied the thermal performance of solar collectors working with two different types of fluids simultaneously. Assari et al. [1] presented a mathematical model for a dual air/water solar collector by the effectiveness method. The model was experimentally verified and subsequently used for the performance analysis of a dual air/water solar collector with three different kinds of air channels, such as rectangular fin, triangular fin, and without fin.

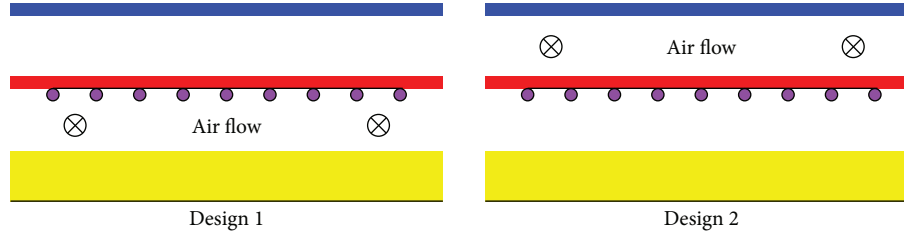


FIGURE 1: Solar DAWC designs considered in the Type 207 model.

The results of the modelling indicated that the rectangular fin has a better performance compared with the others. Jafari et al. [2] provided energy and exergy analysis of a dual air/water solar collector with triangle air channels. The study showed that the dual air/water solar collector has better energy and exergy efficiency than a conventional liquid or air collector. Ma et al. [3] presented experimental and theoretical analyses of the efficiency of a dual air/water solar collector with L-shaped fins and confirmed that the air flow rate is a key factor for thermal efficiency. Later, Mohajer et al. [4] conducted an experimental investigation of a dual air/water solar collector designed by Assari et al. [1]. The experiments showed that the system based on dual-purpose solar collectors could be used as a domestic drying system as well as for providing domestic hot water. Arun and Arun [5] concentrated their research on the utilization of a porous medium in the construction of a dual-purpose solar collector, and they indicated that the utilization of a porous medium leads to the increase in the thermal efficiency of the collector. Nematollahi et al. [6] presented an experimental comparison of a single-fluid solar system based on a liquid collector and a dual air/water solar system based on a dual air/water solar collector. The results showed that the dual air/water system has higher efficiency than a single-fluid system. Venkatesh and Christraj [7] provided an experimental investigation of a multipurpose solar collector system based on the combination of water and air collectors and confirmed its higher system efficiency compared with the conventional system. As opposed to the previous studies, Ji et al. [8] provided an analysis of the separate utilization of the air and water parts of a dual air/water solar collector. In the proposed system, a building-integrated dual-function solar collector will be used to provide space heating during a cold winter and water heating during summer. The results showed a decrease in heating load during winter and a reliably performing hot water preparation system during the summer season.

In the present study, the detailed theoretical model of DAWC has been developed and experimentally verified. Subsequently, the model had been used for annual performance simulation of four different solar systems. To demonstrate the application of the DAWC, three buildings from different locations and each with different energy consumptions were chosen as case studies. The distinctive feature of the presented study is a comparison of the different potential applications of dual air/water solar collectors for the buildings with different energy performance levels and different climatic conditions.

## 2. Detailed Theoretical Model of DAWC

To evaluate the energy performance of the different solar systems based on DAWC, the TRNSYS simulation environment was used. TRNSYS (transient system simulation program) is widely used for both solar and nonsolar simulation studies [9]. A system model consists of individual models of components, which are interconnected by linking the outputs of one component to the inputs of another. Each model is represented by parameters and inputs to compute outputs as a function of time. Since available TRNSYS libraries of component models do not contain any mathematical model of the DAWC collector, the detailed theoretical model of a dual air/water solar collector (Type 207) was created for use in the TRNSYS environment based on the previous models of a liquid solar collector (Type 205) and an air solar collector (Type 206). More detailed information about these models could be found in Shemelin and Matuska [10, 11] and Shemelin et al. [12].

The presented model does not imply the simultaneous work of the liquid and air parts. It means that DAWC model operates either as a liquid collector or as an air collector, depending on the Operating Mode. If the Operating Mode is equal to 0, the model operates as a liquid collector; if it is equal to 1, it operates as an air collector.

**2.1. Description of the Model.** The presented model is a detailed mathematical model developed for thermal performance simulations of two different solar collector designs. The considered designs of DAWC are shown in Figure 1. Design 1 represents an absorber pipe upper-bond configuration with a single air flow between the absorber and the bottom frame insulation. Design 2 represents an absorber pipe upper-bond configuration with a single air flow between the absorber and transparent cover.

The DAWC can be specified by a variety of detailed parameters, such as the optical properties of the transparent cover and absorber and the thermophysical properties of the main components of the solar collector. Moreover, the transparent cover (a single-glazing, transparent-insulation structure) and the back thermal insulation are defined by temperature-dependent thermal conductance.

The presented model of DAWC solves the one-dimensional energy balance of the solar collector under steady-state conditions according to the principle of the Hottel-Whillier equation for usable thermal output:

$$\dot{Q}_u = A_{\text{abs}} F_R [(\tau\alpha)_n G_t - U(T_{\text{in}} - T_{\text{amb}})]. \quad (1)$$

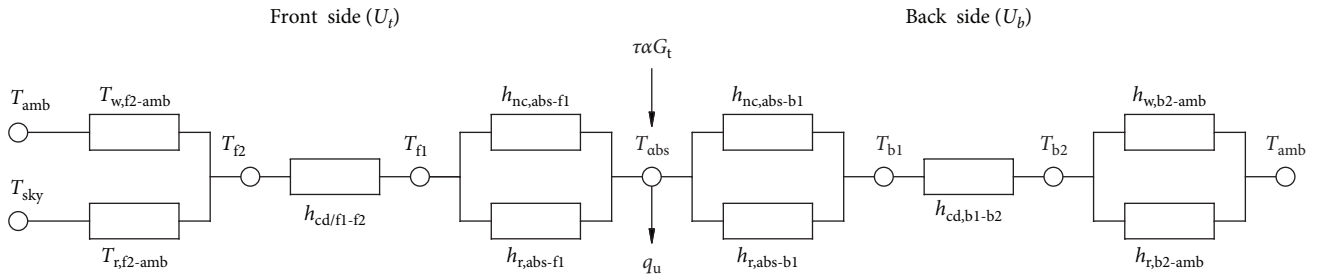


FIGURE 2: The thermal network of external energy balance if Operating Mode is equal to 0—a liquid collector.

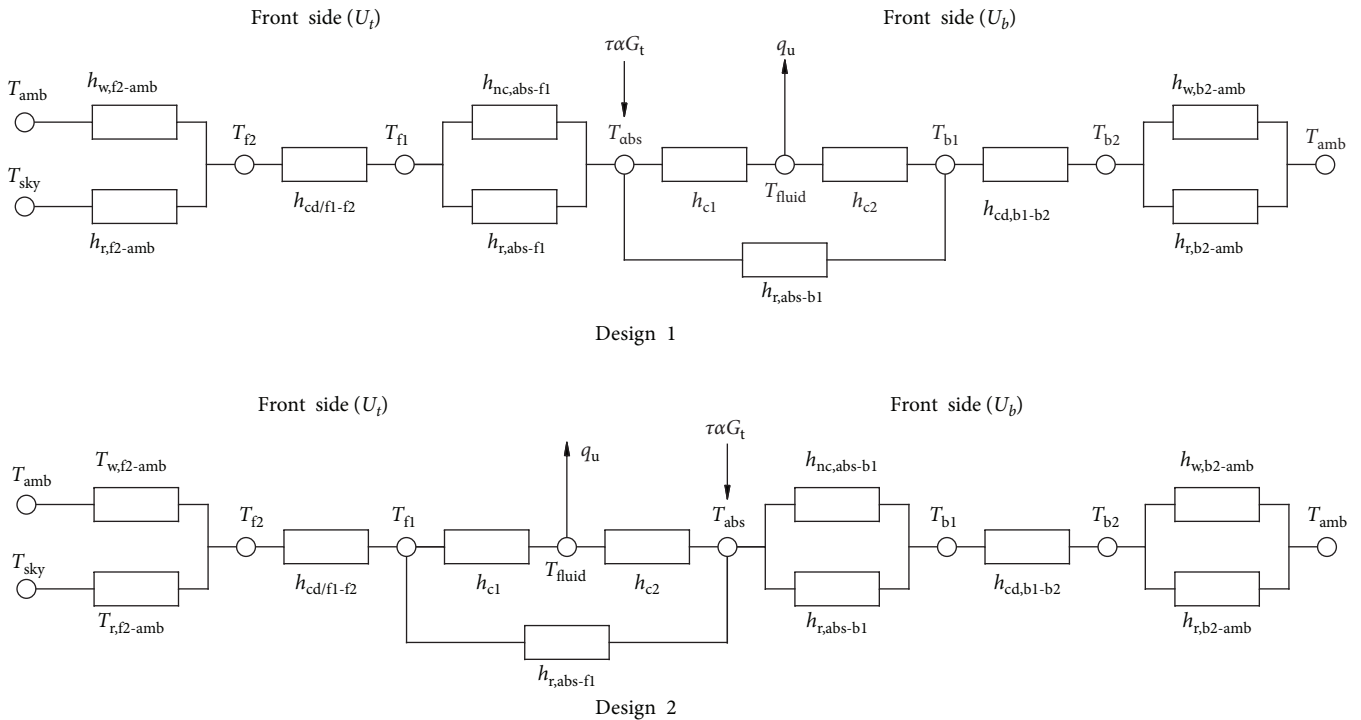


FIGURE 3: The thermal network of external energy balance if Operating Mode is equal to 0—a liquid collector.

In this equation,  $A_{abs}$  is the absorber area ( $m^2$ ),  $F_R$  is the collector heat removal factor (-),  $\tau$  is the solar transmittance of the collector cover (-),  $\alpha$  is the solar absorptance of the absorber (-),  $G_t$  is the total solar irradiance ( $W/m^2$ ),  $U$  is the overall heat loss coefficient of the collector ( $W/m^2 \cdot K$ ),  $\vartheta_{in}$  is the inlet fluid temperature (K), and  $T_{amb}$  is the ambient temperature (K).

The proposed model in general consists of two parts solved in iteration loops: the external energy balance of the absorber (heat transfer from the absorber surface to the ambient environment, see Figures 2 and 3) and the internal energy balance of the absorber (heat transfer from the absorber surface into the heat transfer fluid). Both the external and internal energy balances are mutually dependent. The overall collector heat loss coefficient  $U$  (temperature dependent) as the main output from the external balance is one of the inputs for the internal balance. On the other side, the mean absorber temperature  $T_{abs}$  (K) as the output from

the internal balance is used as the input for the external balance. Since heat transfer coefficients are temperature dependent, the surface temperatures for the main planes of a collector are calculated in the iteration loop until consecutive results of the mean temperatures differ by less than 0.01 K.

Another iteration loop has been introduced to transfer the results from the external balance to the internal balance and the results from the internal balance to the external balance. The basic electric analogy of the proposed model is presented in Figures 2 and 3. A more detailed description of the proposed model could be found in Shemelin et al. [12].

The model was implemented in a TRNSYS environment, as Type 207 offers the parametric analysis for different construction alternatives for annual solar collector performance in the given solar system application. There is also a possibility to change mathematical correlations describing the fundamental heat transfer phenomena (natural convection,

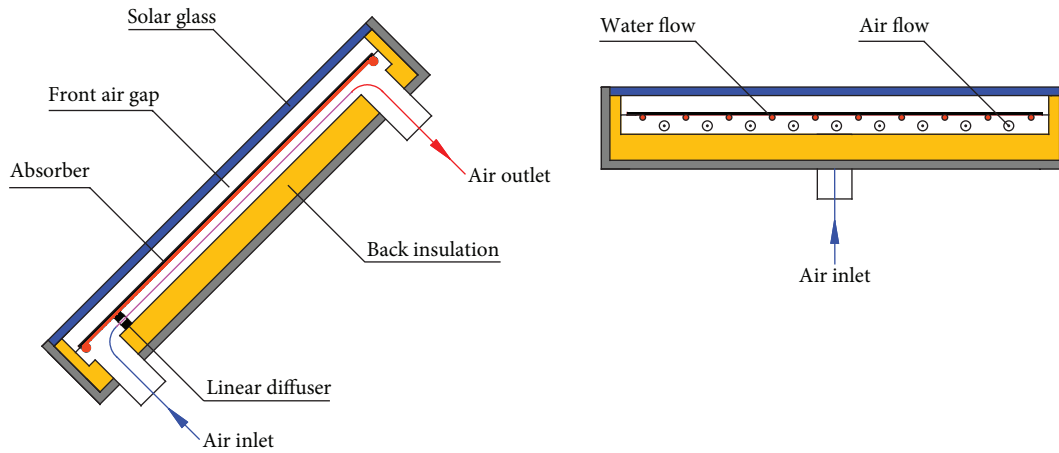


FIGURE 4: Design of the prototype of DAWC.



FIGURE 5: The experimental testing of the liquid and air parts of DAWC.

wind convection, forced convection, etc.) and to perform sensitivity analysis for selected correlations.

**2.2. Model Verification.** The model has been experimentally verified on a prototype of DAWC (see Figure 4) in the frame of solar collector testing according to the European standard EN ISO 9806 within the accredited Solar Laboratory of the Czech Technical University in Prague. The testing of the liquid and air parts has been conducted separately (see Figure 5). The prototype of DAWC has been built from the experimental solar water collector by adjusting the interior air gap. The detailed parameters of the produced prototype are listed in Table 1. If the Operating Mode is liquid heating, water flows in the copper tubes and the air channels are closed at the inlet and outlet. On the

other hand, the inlet and outlet of water pipes are closed in the air heating mode.

Figures 6 and 7 show experimentally evaluated efficiency points and theoretically modelled efficiency characteristics both in the liquid and air operating modes. Experimental data points of solar collector efficiency are coupled with combined standard uncertainty bars in the graphs. The uncertainty analysis has been provided based on methodology published in Mathioulakis et al. [13] and Müller-Schöll and Frei [14]. The theoretical calculation of the efficiency characteristic by the model is subjected to the uncertainty of real collector parameters which are used as inputs for the model. Therefore, the results of the theoretical calculation could be presented as two delimiting curves where the collector efficiency values can be found in reality. It is evident from the

TABLE 1: Main parameters of the dual air/water solar collector.

Collector parameter	Value	Collector parameter	Value
Dimensions (W/L/H)	$1 \times 1.6 \times 0.087$ m	Absorber emissivity	0.05
Area (gross, aperture, absorber)	$1.6 \text{ m}^2, 1.52 \text{ m}^2, 1.49 \text{ m}^2$	Header pipe	Cu $22 \times 1$ mm
Cover material	Solar glass 4 mm	Number of riser tubes	10
Front air gap thickness	30 mm	Distance between riser pipes	100 mm
Absorber material	Aluminium 0.4 mm	Air flow channel	10 mm
Cover transmittance	0.92	Back insulation thickness	40mm
Absorber absorptance	0.95	Insulation material	Rockwool

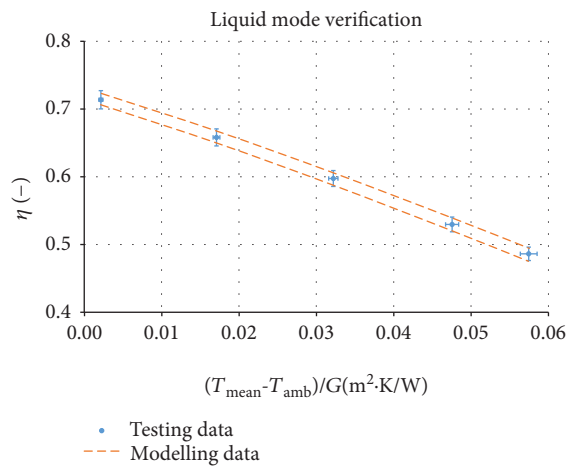


FIGURE 6: Mathematical model verification—liquid heating mode.

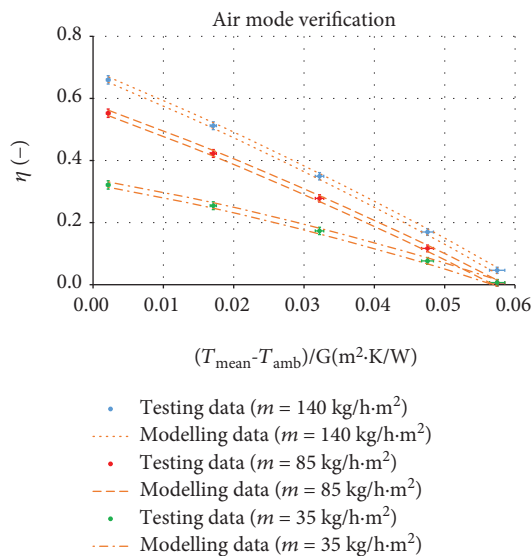


FIGURE 7: Mathematical model verification—air heating mode.

results that simulated efficiency characteristics fit the measurements relatively well, which gives confidence in the developed model. More information about model verification and uncertainty analysis can be found in Shemelin et al. [12].



FIGURE 8: Three-dimensional geometry of the considered buildings.

### 3. Case Studies

To evaluate the energy performance of the DAWC solar system, the system's annual solar yield has been analyzed for a specific site and under specific conditions. Three single-family houses (buildings A, B, and C) (see Figure 8) from different locations (Stockholm, Prague, and Milan) and each with different energy performance levels were considered as case studies for comparative analysis. The detailed building parameters are listed in Table 2. To provide calculations of the total heat demand, the simulation software TRNSYS 17 was used. The climate data used in the analysis were taken from TMY (Meteonorm) for Stockholm, Prague, and Milan. The climatic conditions of the considered sites are listed in Table 3. The results of the modelling are outlined in Figures 9 and 10.

### 4. Solar Systems

To provide comparative analysis of the potential applications of the dual air/water collectors, four different solar energy systems were analyzed. The reference system (RS) is a conventional solar domestic hot water system (see Figure 11) designed with conventional flat-plate liquid collectors with the following parameters: optical efficiency, 0.81; linear heat loss coefficient,  $3.58 \text{ W/m}^2\cdot\text{K}$ ; quadratic heat loss coefficient,  $0.0045 \text{ W/m}^2\cdot\text{K}^2$ ; and incidence angle modifier,  $\text{IAM}_{50} = 0.92$ . The detailed parameters of the reference system are listed in Table 4. There is a different collector area design

TABLE 2: Main parameters of buildings in the analysis.

Key values	Building A	Building B	Building C
		General data	
Occupancy		4 persons	
Climate data source		TMY, Meteororm	
Set point temperature (day/night)		20°C/20°C	
Ventilation air flow rate		100 m <sup>3</sup> /h	
Efficiency of heat recovery unit		75%	
Internal gains (occupants + equipment)		2 W/m <sup>2</sup>	
Weighted mean <i>U</i> value	0.187 W/m <sup>2</sup> ·K	0.375 W/m <sup>2</sup> ·K	0.489 W/m <sup>2</sup> ·K
		Building geometry data	
Gross floor area		286 m <sup>2</sup>	
Heated floor area		246 m <sup>2</sup>	
Ventilated volume		607 m <sup>3</sup>	
		Hot water consumption	
Cold water temperature		Based on TMY	
Hot water temperature		55°C	
Tap profile		160 l/day (7.00: 65 l; 12.00: 30 l; 19.00: 65 l)	

TABLE 3: Climatic conditions of considered sites.

Annual values	Stockholm/Sweden	Prague/Czech Republic	Milan/Italy
Latitude	59.65°N	50.10°N	45.43°N
Mean ambient temperature	5.3°C	7.9°C	11.7°C
Minimum ambient temperature	-19.9°C	-15.2°C	-7.7°C
Maximum ambient temperature	28.3°C	30.7°C	45.1°C
Global solar horizontal irradiation	981 kWh/m <sup>2</sup>	999 kWh/m <sup>2</sup>	1255 kWh/m <sup>2</sup>
Global solar irradiation on tilted surface (South, 45°)	1231 kWh/m <sup>2</sup>	1114 kWh/m <sup>2</sup>	1392 kWh/m <sup>2</sup>

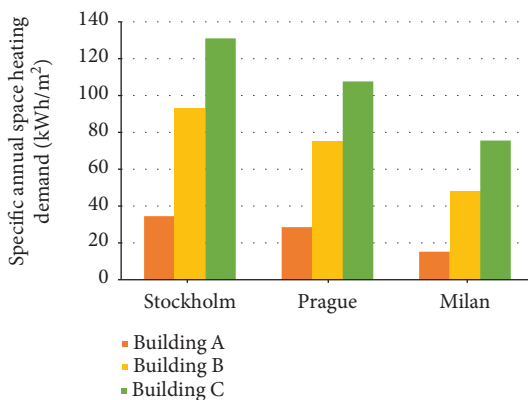


FIGURE 9: Specific space heating demand for buildings and locations.

for each different location to achieve a similar solar fraction for the hot water heating application ( $60 \pm 7\%$ ).

The first alternative system (V1) is based on a DAWC which operates during the hot season in a liquid mode for hot water preparation and then operates for the rest of the

year (cold season) for the preheating of fresh air before it enters the heat recovery ventilation unit (see Figure 12). In the air heating mode, the fresh air is led through the collector and then optionally heated in the heat recovery ventilation unit. In the case of insufficient sunlight (cloudy sky or night time), the air bypasses the collector.

The second system (V2) has the same configuration as the first alternative (V1) with the exception that the collector is installed at the output of the heat recovery ventilation unit. In the air heating mode, the fresh air is firstly preheated in the heat recovery ventilation unit and then optionally is led through the collector (see Figure 13). The preheated air is led through the collector only in cases when the collector has a potential to heat up the air, otherwise the preheated air bypasses the collector.

The third system (V3) differs from the previous two systems—the DAWC operates during the hot season in a liquid mode for hot water preparation and then operates for the rest of the year (cold season) as a solar air collector for a direct recirculating air heating system (see Figure 14). In the air heating mode, the circulating air from the rooms is heated in the collector and then it is led back to the building. The fresh air, after preheating in the heat recovery unit, is mixed

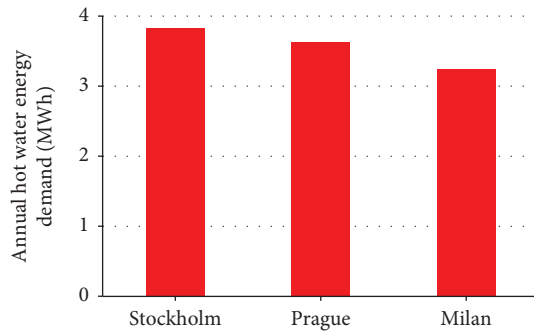


FIGURE 10: Hot water heating demand for given locations.

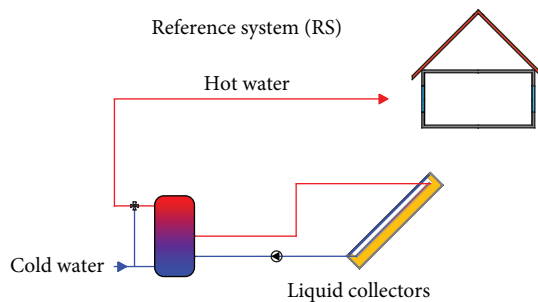


FIGURE 11: The configuration of the reference system (RS).

with the circulation air and only after is it brought into the living rooms. On cloudy days and at night, the circulation air does not flow through the collector. The main feature of this variant is that the flow rate is not limited by the ventilation air flow rate and could be increased up to  $400 \text{ m}^3/\text{h}$ .

The duration of the hot and the cold seasons is different for each system and is dependent on the climatic conditions and the total heat demand of the building. Basically, the mathematical model of DAWC is able to determine in which mode (water or air heating mode) it should operate to get the maximum performance.

The design parameters of the DAWC collector which were used in the simulation of all alternative systems (V1, V2, and V3) are the same as the prototype DAWC and are listed in Table 1. The solar domestic hot water system parameters in the liquid mode are the same as for the reference system and are listed in Table 4. The air heating mode system parameters and operating conditions are shown in Table 5.

## 5. Results and Discussion

To demonstrate the application of the DAWC, three buildings (buildings A, B, and C) from three different locations (Stockholm, Prague, and Milan) and each with different energy performance levels were chosen as case studies for comprehensive analysis. Four different solar systems were compared in the analysis. The solar yield of the described systems was determined by detailed simulations in TRNSYS as the difference in the total heat demand of a building with and without a solar system. The results of the simulation

are shown in Table 6. Values in parentheses indicate the relative difference between the given alternative and the reference system.

Firstly, the results of the simulation indicate that the DAWC design allows increasing the annual energy yield of the solar system depending on the building type and climate. It can be explained by the fact that during the cold season the intensity of solar radiation is not sufficient to heat the liquid in the collector to a usable temperature for domestic hot water supply, but on the other hand, it is sufficient to heat the ambient fresh air at low temperature or the circulation air at the temperature of the room. Besides, it can be seen that the higher building heat energy consumption is correlated to the higher solar energy yield of the compared systems. It means that the DAWC in an air heating mode not only reduces the ventilation heat loss but also contributes to a reduction of the space heating demand.

Secondly, it can be observed that the alternative system V3 shows the highest annual solar energy yield among the compared systems. This result is a consequence of the higher efficiency of DAWC (air heating mode) due to the favorable operating conditions. The efficiency of the air part of DAWC depends on a number of parameters, but the collector air flow rate is dominant (see Figure 5). In the case of the alternatives V1 and V2, the collector air flow rate is limited by the ventilation air flow rate of  $100 \text{ m}^3/\text{h}$ , while in the case of the alternative V3, the air flow is increased to  $400 \text{ m}^3/\text{h}$ .

In the case of the alternative V1, the performance of the heat recovery unit is limited because the air temperature after DAWC could be significantly higher than the outdoor temperature. Moreover, if the fresh air temperature after DAWC is higher than  $18^\circ\text{C}$ , the fresh air bypasses the heat recovery unit and flows directly to the building. Here, the solar DAWC replaces the heat recovery for the ventilation.

If the collector is placed behind the heat recovery unit to provide an additional rise in temperature to the room inlet air, the collector system is energetically more favorable (system V2). Nevertheless, the efficiency of DAWC is limited because the air temperature after the heat recovery unit is higher than the outdoor temperature and consequently the solar collector thermal losses are higher compared to the configuration in system V1.

Naturally, the combination of the DAWC system with heat recovery from the exhaust air reduces the possible heat savings by the DAWC collector. Here, the DAWC and heat recovery system are competing systems and the potential savings are thus limited in total.

Finally, the simulation results show that the DAWC solar system is more efficient in cold and moderate climatic zones than in warm climatic zones. For warm climates, the ambient air temperature during the day in winter is high and space heating demand is low, so the performance of the DAWC (air heating mode) is limited. On the other hand, there is still high hot water energy demand which is not practically limited during winter. As a result, sometimes it is more efficient for DAWC to operate in liquid mode during winter than in the air heating mode for warm climates. Similarly, the larger potential for the DAWC application is indicated for buildings with a higher space heating demand.

TABLE 4: Solar domestic hot water system parameters and operating conditions for given alternatives (RS, V1, V2, and V3).

Parameter	Description
Collector orientation	South, 45° (based in the roof slope)
Collector area	Stockholm and Prague: 4.8 m <sup>2</sup> ; Milan: 3.2 m <sup>2</sup>
Collector mass flow rate	50 l/h·m <sup>2</sup>
Heat transfer medium	Propylene glycol
Pump control	Pump switching on/off temperature difference collector-storage 8 K/2 K
Piping	Supply and return pipes are located in the internal and external environments: 10 m each, DN 16 with 25 mm thermal insulation ( $\lambda = 0.04 \text{ W/m}^2 \cdot \text{K}$ )
Heat exchanger	Smooth tube heat exchanger with $UA = 400 \text{ W/K}$ ( $\pm 15\%$ ) for 42°C/40°C (inlet temperature/tank storage temperature)
Tank storage	Volume: 200 l; heat loss: 1.4 kWh/day; height/diameter ratio: 2.5

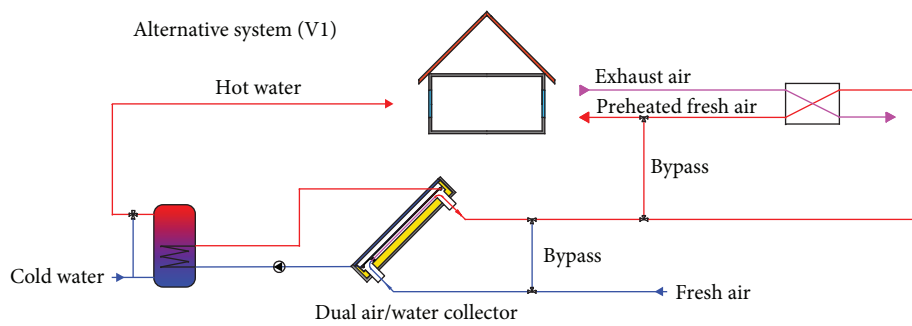


FIGURE 12: The configuration of the alternative system V1.

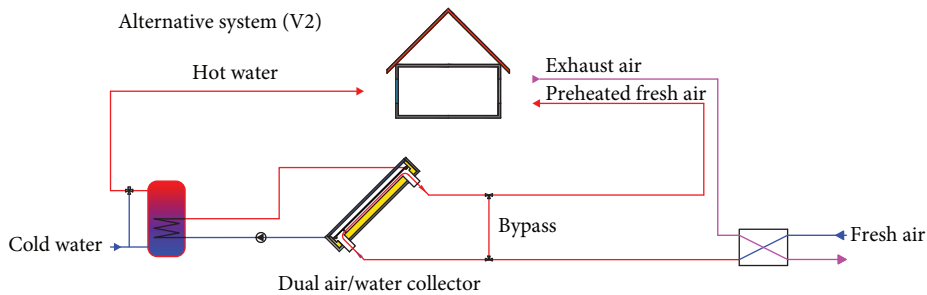


FIGURE 13: The configuration of the alternative system V2.

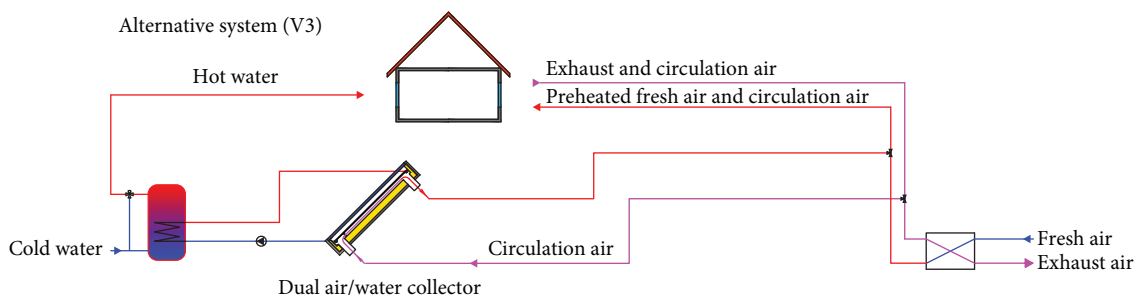


FIGURE 14: The configuration of the alternative system V3.

TABLE 5: Air heating mode (V1, V2, and V3).

Parameter	V1	V2	V3
Collector orientation	South, 45° (based on the roof slope)		
Collector area	Based on the collector area for the reference variant		
Set point temperature	22°C		
Function	Fresh air preheating (before HR unit)	Fresh air preheating (after HR unit)	Direct air heating (recirculating air)
Air flow rate	100 m <sup>3</sup> /h	100 m <sup>3</sup> /h	400 m <sup>3</sup> /h

TABLE 6: The simulation results of the annual solar energy yield of the compared systems.

	RS (kWh/m <sup>2</sup> )	V1 (kWh/m <sup>2</sup> )	V2 (kWh/m <sup>2</sup> )	V3 (kWh/m <sup>2</sup> )
Stockholm				
Building A	418	418 (0%)	439 (5%)	460 (9%)
Building B	418	424 (1%)	461 (10%)	494 (16%)
Building C	418	456 (9%)	511 (20%)	582 (32%)
Prague				
Building A	426	426 (0%)	432 (1%)	448 (5%)
Building B	426	427 (0%)	443 (4%)	474 (11%)
Building C	426	437 (2%)	467 (9%)	529 (22%)
Milan				
Building A	677	677 (0%)	677 (0%)	680 (0%)
Building B	677	677 (0%)	684 (1%)	692 (2%)
Building C	677	681 (1%)	711 (5%)	739 (9%)

## 6. Conclusions

A detailed mathematical model of DAWC has been developed and verified by the experimental testing of the collector in liquid and air heating modes. Subsequently, the comprehensive analysis of different solar systems based on DAWC for three building types (energy performance levels) in three climatic locations has been provided.

Based on the simulation using practical design data, the following can be concluded:

- (i) The alternative V3 with the application of DAWC in the air recirculation heating system shows the highest annual solar energy yield among the compared systems. Depending on the building type, the proposed system V3 allows increasing the annual energy yield of the solar system by up to 32% for the Stockholm climatic conditions, by up to 22% for the Prague climatic conditions, and by up to 9% for the Milan climatic conditions as well
- (ii) The DAWC system is more efficient for buildings with high heat energy consumption, located especially in moderate and cold climates. For instance, for moderate climatic conditions and for a building with “high” heat energy consumption the annual energy yield of the alternative solar system V3 is about 103 kWh/m<sup>2</sup> higher compared to the

reference system RS. On the other hand, for the same climatic conditions and for a building with “low” heat energy consumption the annual energy yield is only 22 kWh/m<sup>2</sup> higher compared to the reference system RS

- (iii) The combination of the DAWC system with heat recovery from the exhaust air reduces the potential heat savings

## Data Availability

The detailed simulation results are available from the corresponding author upon request.

## Conflicts of Interest

The authors declare that there is no conflict of interests regarding the publication of this paper.

## Acknowledgments

This work has been supported by the Ministry of Education, Youth, and Sports within the National Sustainability Programme I, project No. LO1605.

## References

- [1] M. R. Assari, H. Basirat Tabrizi, and I. Jafari, “Experimental and theoretical investigation of dual purpose solar collector,” *Solar Energy*, vol. 85, no. 3, pp. 601–608, 2011.
- [2] I. Jafari, A. Ershadi, E. Najafpour, and N. Hedayat, “Energy and exergy analysis of dual purpose solar collector,” *Academy of Science and Technology*, vol. 81, pp. 259–261, 2011.
- [3] J. Ma, W. Sun, J. Ji, Y. Zhang, A. Zhang, and W. Fan, “Experimental and theoretical study of the efficiency of a dual-function solar collector,” *Applied Thermal Engineering*, vol. 31, no. 10, pp. 1751–1756, 2011.
- [4] A. Mohajer, O. Nematollahi, M. M. Joybari, S. A. Hashemi, and M. R. Assari, “Experimental investigation of a hybrid solar drier and water heater system,” *Energy Conversion and Management*, vol. 76, pp. 935–944, 2013.
- [5] A. V. AK and P. Arun, “Simulation studies on porous medium integrated dual purpose solar collector,” *International Journal of Renewable Energy Research*, vol. 3, no. 1, pp. 114–120, 2013.
- [6] O. Nematollahi, P. Alamdari, and M. R. Assari, “Experimental investigation of a dual purpose solar heating system,” *Energy Conversion and Management*, vol. 78, pp. 359–366, 2014.
- [7] R. Venkatesh and W. Christraj, “Experimental investigation of multipurpose solar heating system,” *Journal of Energy Engineering*, vol. 141, no. 3, 2015.

- [8] J. Ji, C. Luo, T.-T. Chow, W. Sun, and W. He, "Thermal characteristics of a building-integrated dual-function solar collector in water heating mode with natural circulation," *Energy*, vol. 36, no. 1, pp. 566–574, 2011.
- [9] A. Fiksel, J. W. Thornton, S. A. Klein, and W. A. Beckman, "Developments to the TRNSYS simulation program," *Journal of Solar Energy Engineering*, vol. 117, no. 2, p. 123, 1995.
- [10] V. Shemelin and T. Matuska, *TRNSYS Type 205—Model of Glazed Solar Liquid Collector Based on Detailed Construction Parameters and Energy Balance*, CVUT UCEEB, 2017, <http://www.uceeb.eu/results-rp2>.
- [11] V. Shemelin and T. Matuska, *TRNSYS Type 206—Model of Glazed Solar Air Collector Based on Detailed Construction Parameters and Energy Balance*, CVUT UCEEB, 2017, <http://www.uceeb.eu/results-rp2>.
- [12] V. Shemelin, T. Matuska, and B. Sourek, *TRNSYS Type 207—Model of Dual Solar Air-Liquid Collector Based on Detailed Construction Parameters and Energy Balance*, CVUT UCEEB, 2017, <http://www.uceeb.eu/results-rp2>.
- [13] E. Mathioulakis, K. Vorpoulos, and V. Belessiotis, "Assessment of uncertainty in solar collector modeling and testing," *Solar Energy*, vol. 66, no. 5, pp. 337–347, 1999.
- [14] C. Müller-Schöll and U. Frei, "Uncertainty analyses in solar collector measurement," in *Proceedings of the Eurosun Congress*, Copenhagen, Denmark, 2000.

## Research Article

# Numerical Investigations on Charging/Discharging Performance of a Novel Truncated Cone Thermal Energy Storage Tank on a Concentrated Solar Power System

Qianjun Mao <sup>1</sup>, Ning Liu,<sup>1</sup> and Li Peng <sup>1,2</sup>

<sup>1</sup>School of Urban Construction, Wuhan University of Science and Technology, Wuhan 430065, China

<sup>2</sup>College of Chemistry and Chemical Engineering, Northeast Petroleum University, Daqing 163318, China

Correspondence should be addressed to Qianjun Mao; [maoqianjun@163.com](mailto:maoqianjun@163.com) and Li Peng; [sjkpl@163.com](mailto:sjkpl@163.com)

Received 9 August 2018; Revised 10 October 2018; Accepted 30 October 2018; Published 27 January 2019

Guest Editor: Mattia De Rosa

Copyright © 2019 Qianjun Mao et al. This is an open access article distributed under the Creative Commons Attribution License, which permits unrestricted use, distribution, and reproduction in any medium, provided the original work is properly cited.

Developing a concentrated solar power (CSP) technology is one of the most effective methods to solve energy shortage and environmental pollution all over the world. Thermal energy storage (TES) system coupling with phase change materials (PCM) is one of the most significant methods to mitigate the intermittence of solar energy. In this paper, firstly, a 2D physical and mathematical model of a novel truncated cone shell-and-tube TES tank has been proposed based on enthalpy method. Secondly, the performance during the charging/discharging process of the truncated cone tank has been compared with the traditional cylindrical tank. Finally, the effects of inlet conditions of heat transfer fluid (HTF), and thickness of tube on the charging/discharging process, stored/released energy capacity; energy storage/release rate and heat storage efficiency have been investigated. The results show that the performance of truncated cone tank is better, and the charging/discharging time reduces 32.08% and 21.59%, respectively, compared with the cylindrical tank. The effect of wall thickness on the truncated cone TES tank can be ignored. And the inlet temperature and velocity of HTF have the significant influence on the charging/discharging performance of TES tank. And the maximum heat storage efficiency of the truncated cone TES tank can reach 93%. However, some appropriate methods should be taken for improving the thermal energy utilization rate of HTF in the future. This research will provide insights and significant reference towards geometric design and operating conditions in TES system.

## 1. Introduction

The sustainable development of low-carbon economy has become the inevitable choice to realize the win-win situation of economic development and environmental protection around the world. To alleviate the associated environmental problems, reduction of the use of fossil fuels by developing more cost-effective renewable energy technologies becomes increasingly significant. Among various types of renewable energy sources, solar energy takes a large proportion [1–3]. And many believe that actively developing CSP technology is one of the most effective ways to solve current global energy supply problems. However, one major drawback of solar energy is intermittence. To mitigate this issue, the need for energy storage

system arises in most of the areas where CSP technology is utilized [4, 5].

The thermal energy can be stored in different forms, such as sensible heat, latent heat, thermochemical, or a combination of these [6]. In sensible thermal storage, the thermal energy is temporarily stored with rise/fall temperature in the storage media. In latent thermal storage, the considerable latent heat of PCM is absorbed/desorbed in the phase transition process for storing/releasing thermal energy, and this system with PCM owns the advantages of nearly constant temperature and much higher energy density per unit volume compared to the sensible thermal storage. And in thermochemical thermal storage, large amount of enthalpy change in endothermic/exothermic chemical reactions is used to store/release thermal energy,

and the approach is still in the laboratory research stage due to its complexity, safety, and harsh operation condition [7–9]. Thus, latent thermal storage system with PCM is now an effective and feasible solution to store thermal energy in CSP plants.

Avci, Dadollahi, Tao et al. [10–12] investigated the effect of the inlet condition of HTF on the thermal energy storage performance of a cylindrical shell-and-tube TES system for CSP technology. The results indicated that the increase of inlet temperature and velocity of the HTF can enhance the charging performance and energy storage capacity in a TES system. Fang et al. [13] proposed an index of effective energy storage ratio to characterize the effective energy storage capacity of LHTES system with the same volume of tube-in-tank design. The analysis provided implications on an optimal design of LHTES systems in practical CSP plants. Assari et al. [14] studied the TES performance with the different inlet and outlet location of the fluid in horizontal cylindrical tank by numerical and experimental method. The results showed that an appropriate location for the hot water inlet resulted in better thermal stratification in the storage tank, in addition, an appropriate location for the cold water outlet resulted a better collector efficiency, which both increased the performance of solar water heater system.

Many researchers found that the natural convection had a great influence on the charging process in TES system. Seddegh et al. [15] studied the influence of natural convection on charging/discharging of vertical cylindrical TES tank, which was developed to experimentally investigate how the natural convection is initiated and how the energy is transferred from the HTF to PCM in the LHTES system. Tao and He [16] investigated the influence of natural convection and the fins on performance of horizontal latent heat storage tank. The results showed that the high temperature molten salt flows upward which enhances the PCM melting rate in upside and weakens the melting rate in downside due to the effects of natural convection. Kurnia and Sasmitob [17] proposed a rotating TES system to overcome the shortcoming of natural convection. The results revealed that rotation does increase the heat transfer performance, and this system with up to 25% and 41% enhancement can be achieved during charging and discharging, respectively. Gao et al. [18] investigated the thermal performance of the cubic TES system with coil tubes. The results showed that natural convection accelerated the thermal energy transport in the melt phase in the upper region but weakened the heat transfer in the bottom region.

In general, the molten salt is one of the most promising PCM used in CSP plant; however, the main shortcomings of them are low thermal conductivity, and a lot of works have been studied to overcome this issue and to enhance the heat transfer rate of TES tank in CSP system. Parsazadeh, Yang et al. [19, 20] investigated the melting process in shell-and-tube TES system with annular fins. The numerical results showed that the fins exhibited a promising potential for enhancing heat transfer in CSP technology. Amagour et al. [21] studied the finned-tube LHTES system based on the method of equivalent circular fin efficiency for the calculation of the effective heat transfer surface area. And the

compact finned-tube system presented a satisfactory overall performance compared to other published results. Gasia et al. [22] compared the performance of TES in four systems including the addition of fins and the use of two different HTF. The results revealed that the finned designs showed an improvement of up to 40% for the same HTF, and water showed results up to 44% higher than silicone for the same design. Zhu, Eslami et al. [23, 24] studied the transient behavior of the rectangular thermal energy tank equipped with fin configurations. The results showed that the fins can obviously enhance the thermal performance. Parsazadeh and Duan [25] analyzed the influence of nanoparticles added on HTF and PCM on a shell-and-tube TES system for CSP technology.

In addition, the packed bed LHTES system with spherical capsules has been studied in recent years for enhancing the heat transfer rate in CSP plants. Bellan et al. [26] analyzed the dynamic thermal performance of high temperature latent thermal energy system packed with spherical capsules. The results indicated that the Stefan number and the shell properties of the capsule significantly influence the thermal performance of the system. Ma and Zhang [27] adopted Al-Si and air as the PCM and HTF, respectively, and built the packed bed system. The results showed that the performance of PCM is better than rock due to the high latent heat and thermal conductivity of the PCM (alloy). Abdulla and Reddy [28] investigated the thermal performance of a packed-bed thermocline TES system, and it was found that the relative to inlet salt velocity and operating temperature range have more influence on the thermal performance of TES system.

It is clear from the literature reviewed above that the natural convection accelerated the thermal energy transport in the upper region and weakened the heat transfer in the bottom region during the charging process [16, 18]. And the shell-and-tube TES system is the promising design to store energy due to its symmetrical structure and simple analysis. Therefore, this paper proposed a novel truncated cone shell-and-tube TES tank of CSP plant to enhance the heat transfer by taking advantage of natural convection. And it is compared with the performance of traditional cylindrical TES tank. A 2D model is built to numerically investigate the effects of inlet temperature, velocity of the HTF, and the thickness of tube on the charging/discharging performance with this novel TES system. This research will provide a significant reference towards geometric design and operating conditions by considering the effect of natural convection on a TES system for CSP plant.

## 2. Physical Model and Governing Equations

*2.1. Physical Model of a Novel Truncated Cone Tank.* The physical model is shown in Figure 1, which is a truncated cone shell-and-tube configuration. The HTF flows in the inner tube, and the shell side is full of PCM with the mass of 54%  $\text{NaNO}_3$  and 46%  $\text{KNO}_3$ . The length ( $L$ ) of this tank is 200 mm, the radius for the inner tube ( $R_{\text{in}}$ ) is 20 mm, and the material of the inner tube is steel. In addition, the container external surface is treated as an adiabatic

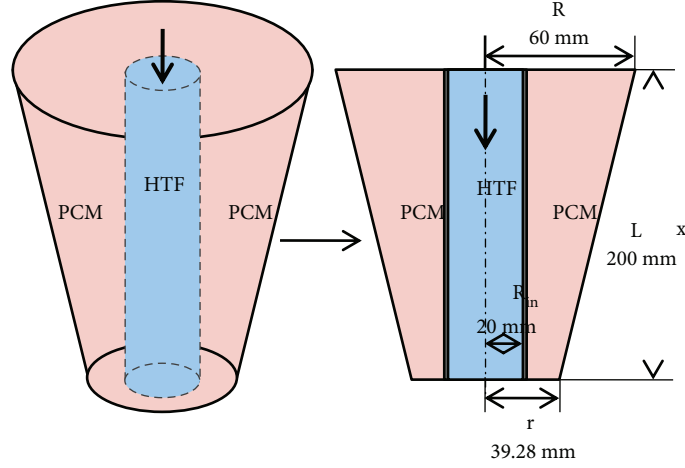


FIGURE 1: Schematic diagram of a truncated cone shell-and-tube TES model.

boundary with the radius of the top and bottom as 60 mm ( $R$ ) and 39.28 mm ( $r$ ), respectively, and the taper of this truncated cone model is 0.2072. Under the condition of the constant volume/mass of the PCM and the same radius of the inner tube, the traditional cylindrical shell-and-tube model is built and simulated. The thermophysical properties of PCM are shown in Table 1.

In order to simplify the physical and mathematical model, the following assumptions are adopted [8, 29].

- (1) The HTF flow entering the tube was laminar and simultaneously developing
- (2) The thermal conduction and viscous dissipation in the axial direction is neglected for PCM
- (3) The thermal properties of PCM in both solid and liquid phase do not change with the temperature
- (4) Adiabatic wall was assumed
- (5) The models are simplified to 2D axisymmetric

**2.2. Governing Equations.** The enthalpy method is adopted to deal with the moving boundary problem in a solid-liquid phase change process. The corresponding governing equations are shown as follows [12, 30].

For the HTF,

$$\frac{\partial \theta_f}{\partial t} = -A \frac{\partial \theta_f}{\partial x} - B(\theta_f - T)_a, \quad (1)$$

where  $\theta_f = T - T_m$ ;  $A = \dot{m}_f / \rho_f \pi R_{in}^2$ ,  $B = 2h / (\rho C_p)_f R_{in}$ ,  $h = (k/2R_{in})0.022P_r^{0.8}$ , and  $T_a$  is the average temperature of the PCM and  $T_m$  is the melting temperature.

For the PCM,

$$(\rho C_p)_p \frac{\partial \theta}{\partial t} = \frac{\partial}{\partial x} \left( \lambda'_p \frac{\partial \theta}{\partial x} \right) + \frac{1}{r} \frac{\partial}{\partial r} \left( r \lambda_p \frac{\partial \theta}{\partial r} \right) - \rho_p \Delta H \frac{\partial f}{\partial t}, \quad (2)$$

where  $\theta = T - T_m$ ,  $f$  is the liquid fraction of the PCM,

TABLE 1: Thermophysical properties of PCM.

	PCM (NaNO <sub>3</sub> /KNO <sub>3</sub> )
$\rho$ (kg/m <sup>3</sup> )	2040(s), 1950(l)
$\lambda$ (W/m·K)	0.5(s), 0.3(l)
$C_p$ (J/kg·K)	1420(s), 1500(l)
$T_m$ (K)	497
$\Delta H$ (kJ/kg)	105.8

\*The "(s)" and "(l)" stand for "solid" and "liquid" of PCM, respectively.

$\Delta H$  is the PCM melting enthalpy.  $\lambda'$  and  $\lambda_p$  are the thermal conductivity of PCM in  $x$  and  $r$  direction (W/m·K).

The energy equation (2) is formulated by enthalpy method. And the liquid fraction is determined as

$$\begin{cases} f = 0, \theta < 0, \\ 0 < f < 1, \theta = 0, \\ f = 1, \theta > 0. \end{cases} \quad (3)$$

To calculate the stored energy of the PCM, the stored energy capacity of the TES system is given by [31]

$$Q = m \int_{T_0}^{T_m} C_{p,s} dT + mf \Delta H + m \int_{T_m}^{T_a} C_{p,l} dT. \quad (4)$$

Meanwhile, the released energy capacity of the TES system is given by

$$Q' = m \int_{T_0}^{T_m} C_{p,l} dT + mf \Delta H + m \int_{T_m}^{T_a} C_{p,s} dT, \quad (5)$$

where  $m$  is the mass of PCM (kg),  $T_0$  is the initial temperature of the PCM (K),  $T_m$  is the melting temperature and  $T_a$  is the average temperature of PCM at the end of melting process (K),  $f$  is the liquid fraction of PCM, and  $\Delta H$  is the enthalpy of fusion (kJ/kg). Meanwhile,  $C_{p,s}$  and  $C_{p,l}$  represent the specific heat of the PCM at the state of

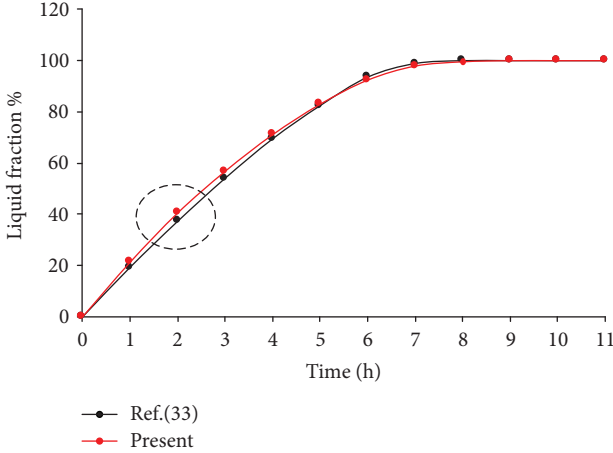


FIGURE 2: Comparison between the present result and the result of literature Ref. [32].

solid and liquid (kJ/kg·K), respectively. The equation has three parts with the first part representing sensible heat stored in the solid phase, the second part represents latent heat of fusion, and the third part represents sensible heat stored in PCM in the liquid phase.

### 3. Model Validation and Testing

The finite volume solver ANSYS Fluent 16.0 is used to discretize the governing equations. Due to the coupled energy transfer process between the HTF and PCM, the energy equation both for HTF and for PCM is integrated solving in the whole computational domain. Accordingly, to calculate the Reynolds number of HTF ( $Re_{\max} = 1654 < 2300$ ,  $v_{\max} = 1.2$  m/s), the laminar is selected as the flow model. And the coupled fluid dynamic and energy equations are solved by SIMPLEC algorithm. The second order upwind method is applied as the spatial discretization method for pressure, momentum, and energy. In order to ensure the accuracy of the calculation, the residual of the energy equation is less than  $10^{-6}$ .

In order to validate the reliability of the physical model, the setting, calculation, and simulation results based on Fluent 16.0 software, the comparisons between the present numerical predictions, and the literature results which is the theoretical analysis by C language in MATLAB software [32] were performed under the same geometric parameters and operation conditions. The comparative results are shown in Figure 2. In the plots, the melting time is approximately 7h both of the two methods, and the melting time error is about 6.67%. Meanwhile, the maximum melting error is about 8.70% at 2h, which is shown in the dashed circle. The results show that these errors (8.7% and 6.67%) are within the allowable range of engineering errors. Therefore, the good agreements show that the physical model and simulation results based on Fluent 16.0 software in the present paper are acceptable and reliable. It can be seen that the settings of Fluent 16.0 here can be used for simulation experiments.

TABLE 2: The results of mesh independent and time step independent test.

Total mesh	Total melting time (s)	Time step (s)	Total melting time (s)
12,400	6926	0.05	6939
24,080	6936	0.1	6941
46,224	6942	0.5	6942
92,017	6953	1	6953
179,177	6961	2	6979

The mesh of this model consists of the quadrilateral cells. To ensure mesh independent result, mesh independence test was conducted by systematically increasing the number of cell and the results as shown in Table 2. The results did not show a significant change in the total melting time as the number of cells increases to 179,177. Therefore, in order to save the computational time, the mesh size of 46,224 cells for the truncated cone shell-and-tube TES model was chosen for the simulations. Besides, the maximum and minimum time steps are 2s and 0.05s, respectively. And the Courant number is the default value. Accordingly, to analyze the total melting time of the five cases, the time step size of 0.5s was the most appropriate to be accounted for the transient nature of the model and the results as shown in Table 2.

## 4. Results and Discussions

### 4.1. The Charging Process of TES

4.1.1. Comparison of the TES Performance between Cylindrical and Truncated Cone TES Model in Charging Process. In order to compare the TES performance between traditional cylindrical and truncated cone TES tanks, the inlet temperature and velocity of HTF are 797K and 1.2 m/s, respectively.

The contour of the PCM liquid fraction and temperature field in the cylindrical and truncated cone tank during the melting process are shown in Figure 3. It is noted that the melting starts on the tube wall surface and expands inside the PCM, and the upper region of the PCM is melting first compared to the lower region. From the corresponding temperature field, it can be found that the temperature shows an obvious ladder distribution, and the temperature closing to the heat pipe region and the top region of the PCM is higher. This phenomenon can be explained in terms of heat conduction and natural convection. On the one hand, the temperature difference is larger in the upper region of the PCM and HTF, so that the heat transfer rate is faster in this region. On the other hand, the higher-temperature liquid PCM rises because of the effect of natural convection, which promotes the melting of the upper PCM. However, the influence of the heat conduction can be ignored in the heat transfer process, because the length of these two models studied in this paper is identical.

According to the melting time and liquid fraction in Figure 3, on the whole, the truncated cone tank can melt

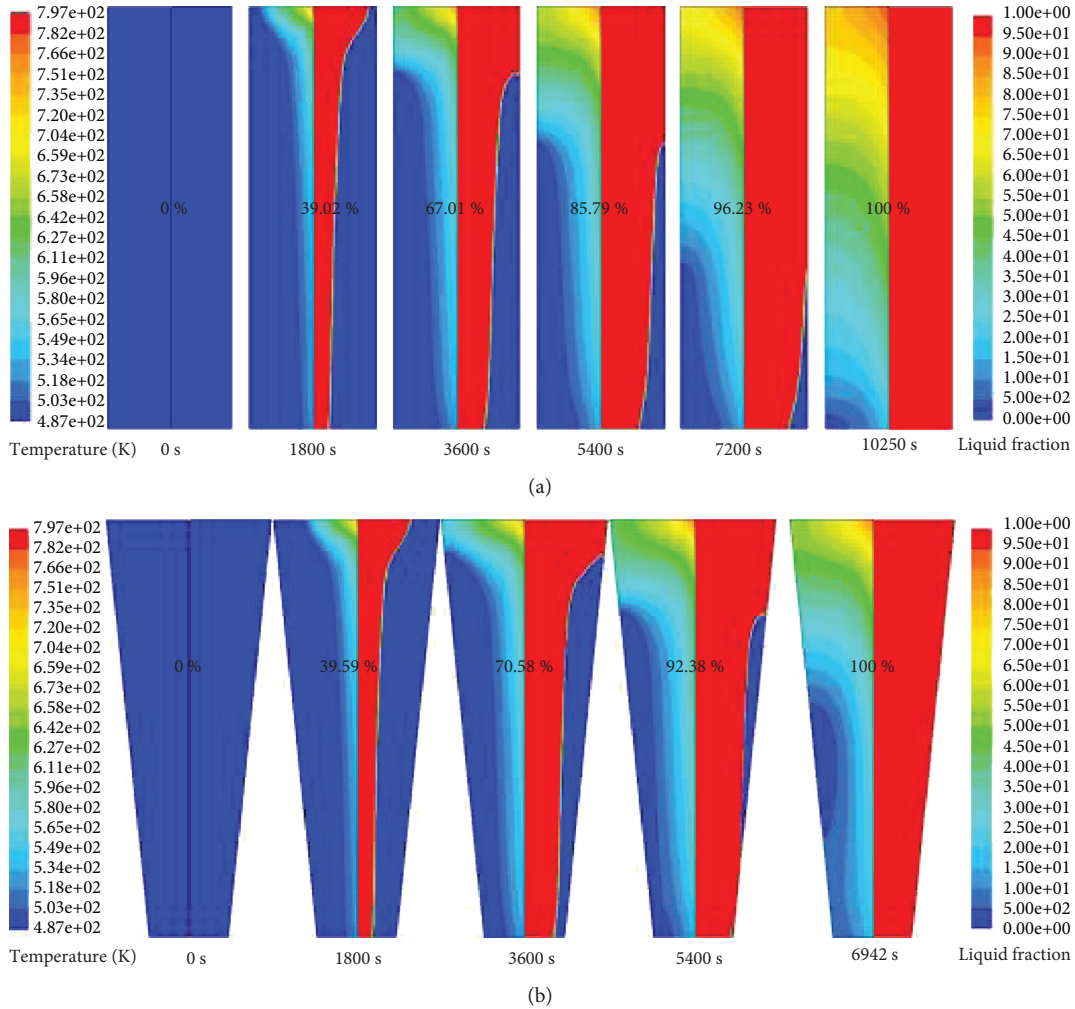


FIGURE 3: Contour of the PCM temperature (left) and liquid fraction (right) in the (a) cylindrical and (b) truncated cone model during the charging process.

much faster than the cylindrical tank at the same operating condition during the process. However, the liquid fraction of a truncated cone tank is about 40%, which is equal to the liquid fraction of a cylindrical tank at 1800 s. After that, the melting process of a truncated cone tank is obviously quicker than a cylindrical tank, and the total melting time reduces about 32.08% compared with the cylindrical tank. This indicates that the thermal energy storage performance of a truncated cone tank is better and the melting process is faster than the cylindrical tank under the same operating condition.

Figure 4 presents the simulated liquid PCM velocity field with a cylindrical and truncated cone TES tank during the melting process, which can explain the reason of the upper region of PCM melt faster than the lower region of PCM. It can be seen that the clockwise convection circulation arises at the liquid region of PCM, and the high-temperature liquid PCM at the vicinity of the HTF pipe flows upward due to the effect of natural convection, whereas the low-temperature liquid PCM flows downward along the liquid/solid interface of PCM because of the action of natural gravity. In this situation, the natural convection

accelerates the thermal energy transfer at the top region and weakened the thermal energy transfer at the bottom region of the PCM. Therefore, the truncated cone tank can obviously reduce the melting time compared to the cylindrical TES tank.

**4.1.2. Effects of Thickness of Tube on Charging Process.** In order to study the effect of thickness of tube on the TES performance during the charging process, the inlet temperature and velocity of HTF are 797 K and 1.2 m/s, respectively, and the initial temperature of PCM and tube is 487 K. Meanwhile, the radius for the inner tube ( $R_{in}$ ) is always 20 mm.

Figure 5 presents the effects of different thickness of tube on liquid fraction and melting process. It can be seen that the liquid fraction of PCM decreases with the increasing thickness of tube in the early stage. The possible reason is that the thermal resistance increases with the increase of the thickness of the tube lead to the melting rate reduce. And after that, the liquid fraction increases with the increasing thickness of tube during the melting process. That is because the increasing thickness of the tube makes the mass

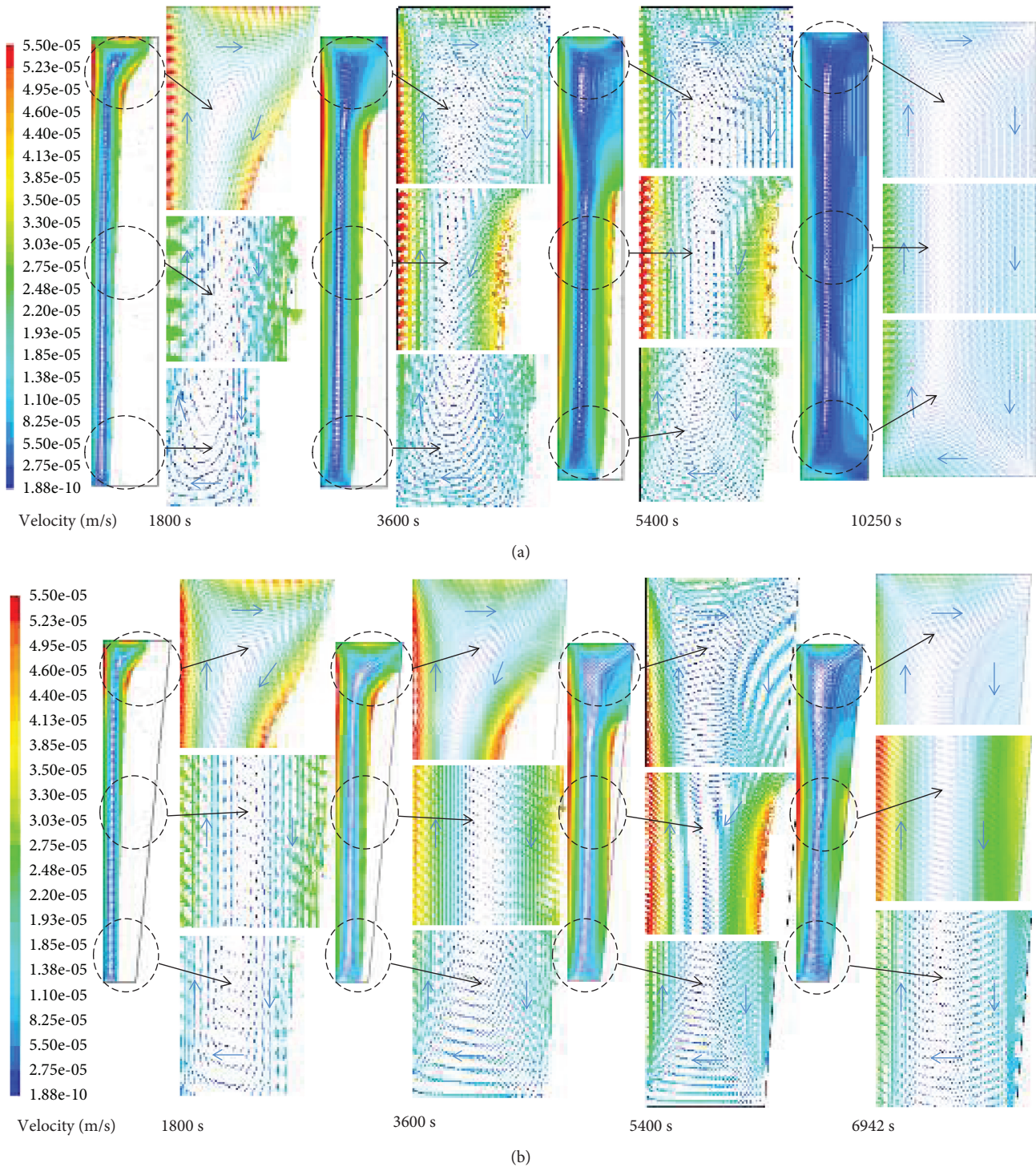


FIGURE 4: The simulated liquid PCM velocity field with cylindrical (a) and truncated cone (b) TES unit during the melting process.

of PCM reduce slightly, as a whole, the melting time of PCM will be slightly reduced with the decrease of the PCM. And the influence of the thickness of tube on the melting time gradually weakens with the increasing of the wall thickness. However, the reduction of the melting time can be negligible compared to the case where the wall thickness is neglected. Therefore, the effect of wall thickness on the truncated cone TES system is ignored in the rest of the studies.

*4.1.3. Effects of Inlet Temperature of HTF on Charging Process.* The initial temperature of PCM with 487 K, and the inlet velocity of HTF with 1.2 m/s is chose to study the effects of inlet temperature of HTF on the melting process. And the inlet temperature of the HTF is six temperature gradients, including 597 K, 647 K, 697 K, 747 k, 797 K, and 847 K.

The effects of inlet temperature of HTF on melting process are shown in Figure 6, which include the charging

process of a cylindrical TES tank under the inlet temperature of HTF at 797 K. It can be seen that the melting time decreases with the increasing inlet temperature of HTF, and the slope of this curve is larger in the early stage. Higher temperature difference between HTF and PCM leads to the heat transfer rate increasing. At the same time, it can be seen that the higher the inlet temperature of the HTF is, the bigger the slope of the melting curve is and the higher the heat storage rate of the PCM is. And under the same operating conditions (the inlet temperature of HTF is 797 K), the charging time of the truncated cone TES tank is shorter than that of the cylindrical tank. The results are consistent with the contour of the PCM liquid fraction and temperature in the cylindrical and truncated cone tank during the charging process.

The effects of initial inlet temperature of HTF on the outlet temperature of HTF are presented in Figure 7. Meanwhile, the numbers represent the total melting time during the charging process. From Figure 7, the initial inlet temperature increasing from 597 K to 847 K, the melting time will decrease from 15,111 s to 6262 s, which reduces about 58.56%. And the outlet temperature increases with the increasing initial inlet temperature. For each case, the outlet temperature of the HTF increases slowly during this process. As a whole, the higher the inlet temperature of the HTF, the greater the temperature difference between the inlet and the outlet temperature. And when the inlet temperature is 847 K, the corresponding minimum outlet temperature is 786 K, and the temperature difference is about 60 K. It can be seen that the thermal energy utilization rate from HTF is very low during this process. Therefore, some methods should be taken to reduce the loss of energy and improve the thermal energy utilization rate of HTF in the TES system for enhancing the CSP plant efficiency.

Figure 8 presents the effects of initial inlet temperature of HTF on the total stored energy capacity and energy storage rate during the charging process. The histogram and curve show the total stored energy capacity and total energy storage rate of the TES tank, respectively. And the value of the total stored energy capacity is calculated by equation (4). The total energy storage rate is calculated by following equation.

$$v_Q = \frac{Q}{t}, \quad (6)$$

where the  $v_Q$  represents the total energy storage rate (J/s),  $Q$  is the total stored energy capacity (J), and  $t$  is the charging time (s).

The histogram indicates that the total stored energy capacity and initial inlet temperature of HTF has notable positive correlation, and the initial inlet temperature of HTF increasing from 597 K to 847 K, the total stored energy capacity will increase from 506.55 kJ to 753.21 kJ, which increases about 48.69%. However, the increment of stored energy capacity decreases with the increase of inlet temperature. Meanwhile, the curve shows that the total energy storage rate increases significantly with the increase of inlet temperature, and the inlet temperature increasing from

597 K to 847 K, the energy storage rate will increase from 33.52 J/s to 120.28 J/s, which increases about four times.

It is shown that the inlet temperature of HTF has the significant influence on the TES system for a truncated cone shell-and-tube tank. The increase of inlet temperature can not only shorten the total charging time but also increase the total stored energy capacity and energy storage rate. Therefore, it is very important to select the proper inlet temperature of HTF according to the actual operating conditions to improve the storage efficiency of the TES system in the CSP plant.

*4.1.4. Effects of Inlet Velocity of HTF on Charging Process.* In order to study the effect of the inlet velocity of HTF on the charging process of the TES tank, the initial temperature of the PCM and HTF is 487 K and 797 K, respectively. And the inlet velocity of the HTF is six temperature gradients, including 0.2 m/s, 0.4 m/s, 0.6 m/s, 0.8 m/s, 1.0 m/s, and 1.2 m/s.

Figure 9 presents the effects of inlet velocity of HTF on liquid fraction during the charging process. As a whole, the slope of the melting curve decreases gradually in the charging process of liquid fraction up to 100%. And the charging time decreases with the increasing inlet velocity of HTF, because the higher velocity of HTF makes the temperature difference between HTF and PCM augment, which leads to the heat transfer rate increasing. With the increase of inlet velocity, the effect of HTF on charging time becomes smaller and smaller.

The effect of inlet velocity on outlet temperature of HTF is presented in Figure 10. The result shows that the outlet temperature increases with the increase of the inlet velocity of HTF. From the curves, the tendency of outlet temperature is rather gradual during the process. However, the outlet temperature difference of HTF is decreasing with the increasing initial inlet velocity. It was found that increasing the velocity of HTF from 0.2 m/s to 1.2 m/s reduces the melting time from 11,334 s to 6972 s by 38.48%. And when the inlet velocity of HTF is 0.2 m/s, the outlet temperature is the smallest (the minimum outlet temperature of 695 K), and the maximum temperature difference is 102 K. At this time, there is still a large amount of heat energy to not be utilized from the HTF.

Figure 11 presents the effects of inlet velocity of HTF on the total stored energy capacity and total energy storage rate during the process. The histogram shows that the total stored energy capacity of the TES tank increases with the increase of the inlet velocity of HTF, but the increasing amplitude is decreasing gradually. And the inlet velocity increasing from 0.2 m/s to 1.2 m/s, the total stored energy capacity will increase from 571.80 kJ to 669.49 kJ, which increases about 17.08%. However, the increment of stored energy capacity decreases with the increasing velocity. The curve indicates that the energy storage rate increases with the increase of inlet velocity of HTF, and the inlet velocity increasing from 0.2 m/s to 1.2 m/s, the total energy storage rate will increase from 50.45 J/s to 96.02 J/s, which increases about double. It can be seen that the inlet velocity of the HTF has a great influence on the heat storage characteristics of the TES tank in the CSP system.

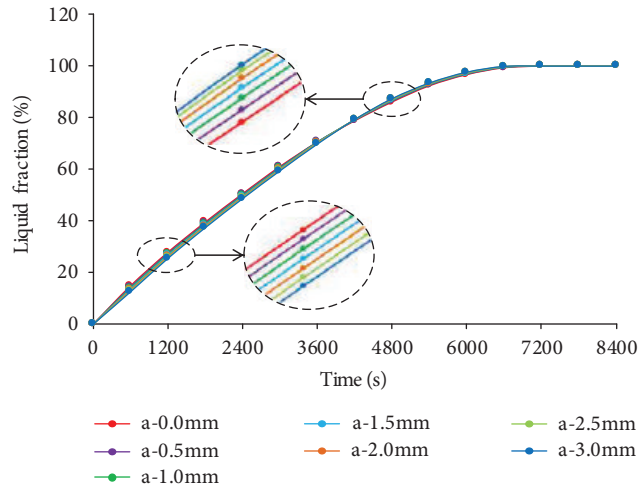


FIGURE 5: Effects of thickness of tube on liquid fraction.

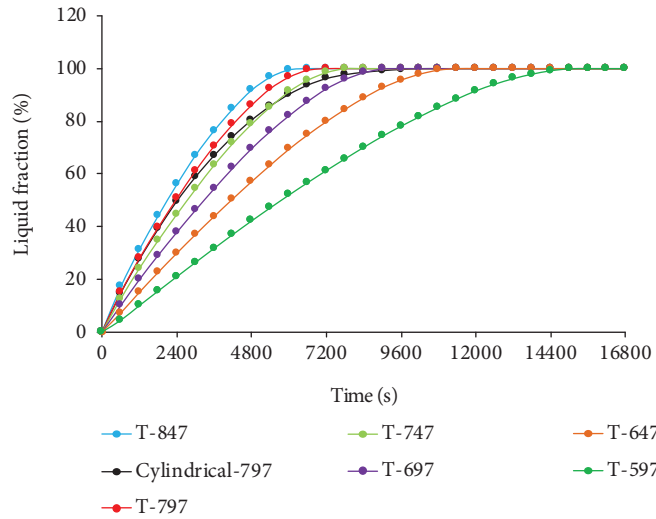


FIGURE 6: Effects of inlet temperature of HTF on liquid fraction.

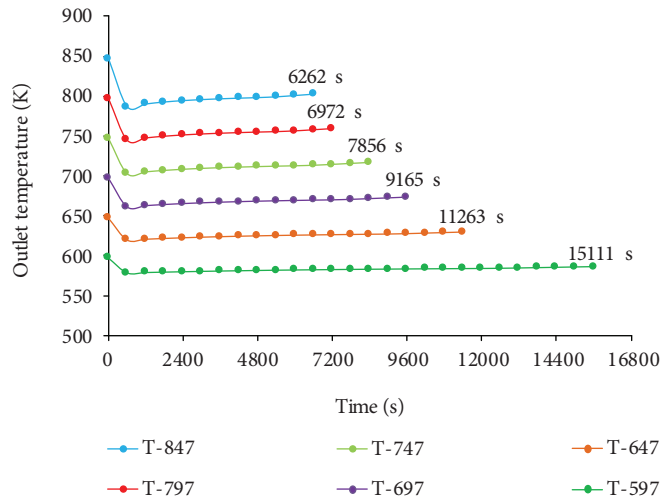


FIGURE 7: Effects of inlet temperature of HTF on outlet temperature of HTF.

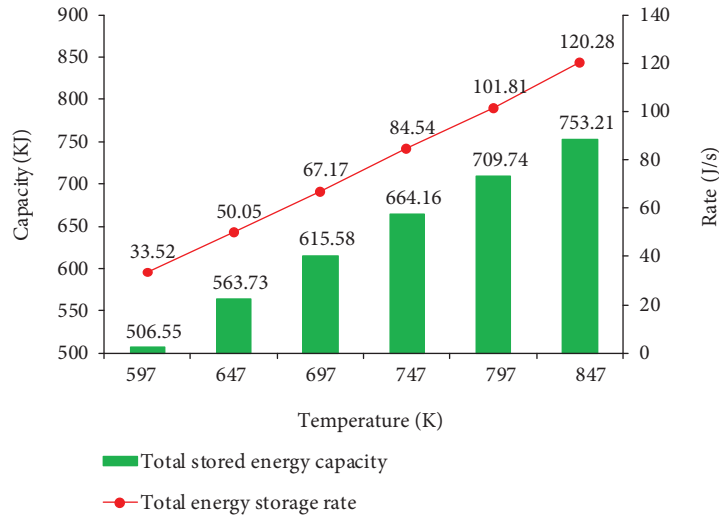


FIGURE 8: Effects of inlet temperature of HTF on the total stored energy capacity and energy storage rate.

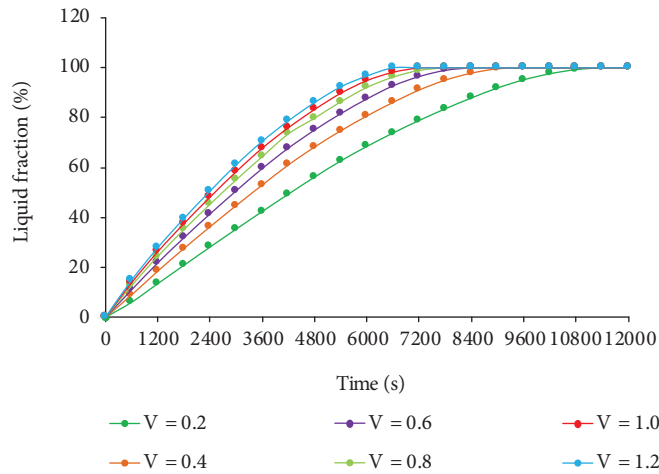


FIGURE 9: Effects of inlet velocity of HTF on liquid fraction.

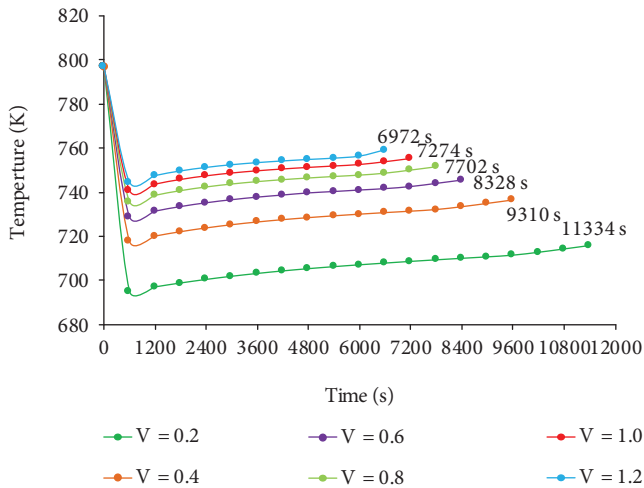


FIGURE 10: Effects of inlet velocity of HTF on outlet temperature of HTF.

#### 4.2. Discharging Process of TES

4.2.1. Comparison of the TES Performance between Cylindrical and Truncated Cone TES Model during the Discharging Process. In order to compare the thermal energy release performance between traditional cylindrical and truncated cone TES tanks, the inlet temperature and velocity of HTF are 377 K and 1.2 m/s, respectively, and the initial temperature of PCM and steel is 507 K.

The contour of the PCM liquid fraction and temperature field in the cylindrical and truncated cone model during the discharging process are shown in Figure 12. It is found that the PCM begins to solidify at the surface of the heat conduction tube wall, and the upper region of PCM solidification is firstly compared to the bottom region of PCM. In this process, it can be seen that the temperature field is consistent with the solid-liquid phase of the PCM in TES tank. On the whole, the temperature of upper PCM is lower than the bottom region. This phenomenon can directly explain the reason that the upper PCM completed the solidification process firstly.

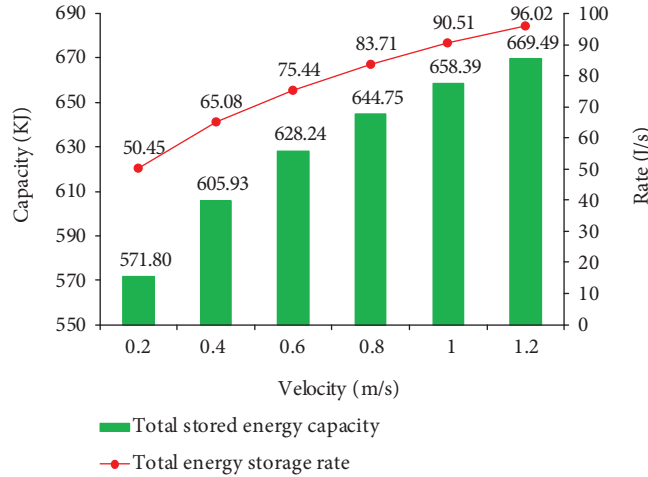


FIGURE 11: Effects of inlet velocity of HTF on the total stored energy capacity and energy storage rate.

From the total discharging process, the truncated cone tank can solidify slightly faster than the cylindrical tank at the same operating condition during the discharging process. The liquid fraction difference of them is only 0.64% at 3600 s, which shows the thermal energy release rate is almost parallel at the beginning. After that, the liquid fraction of a truncated cone tank is decreasing faster than a cylindrical tank. It can be found that the discharging rate of a truncated cone unit is faster than a cylindrical tank, and the discharging time reduces about 21.59% compared to the cylindrical model. This indicates that the thermal energy release performance of truncated cone TES tank is slightly better than the traditional cylindrical tank for CSP plant under the same operating condition.

And Figure 13 presents the simulated liquid PCM velocity field with truncated cone TES tank at 3600 s. It can be seen that the anticlockwise convection circulation arises at the liquid region of PCM. And the high-temperature liquid PCM at the vicinity of shell flows upward due to the effect of natural convection, which is weakened compared to the charging process. Whereas the low-temperature liquid PCM flows downward along the liquid/solid PCM interface because of the natural gravity, which is accelerated compared to the charging process. In this situation, the natural convection makes the higher-temperature liquid PCM flow upward, which accelerates the thermal energy releasing at the upper region of PCM during the discharging process due to the lower temperature at the top of HTF. Therefore, the truncated cone TES tank can also reduce the discharging time compared to the traditional cylindrical TES tank.

**4.2.2. Effects of Inlet Temperature of HTF on Discharging Process.** In order to investigate the effects of initial inlet temperature of HTF on discharging process, the inlet velocity of HTF is 1.2 m/s, the initial temperature of PCM is 507 K, and the inlet temperature of the HTF is six temperature gradients, including 377 K, 387 K, 397 K, 407 K, 417 K, and 427 K. The thickness of tube is neglected due to its slight effect on thermal energy storage performance.

Figure 14 shows the effects of initial inlet temperature of HTF on discharging time and liquid fraction of PCM during the discharging process, which include the discharging process of cylindrical TES tank under the inlet temperature of HTF at 377 K. It can be seen that the slope of the curves of the TES tanks decreases gradually under different inlet temperatures of HTF, which indicates that the thermal energy release rate of the TES tanks reduce gradually. The larger the inlet temperature of the HTF is, and the smaller the slope of the whole corresponding curve is. Under the same operating conditions, the total discharging time of the truncated cone TES tank is shorter than that of the cylindrical tank. The results are consistent with the contour of the PCM liquid fraction and temperature in the cylindrical and truncated cone tank during the discharging process (Figure 12).

When the inlet temperature of the HTF is 377 K, it takes 12,920 s for the cylindrical tank to complete the discharging process and only 10,130 s for the truncated cone tank, which reduces 21.59%. For the truncated cone TES tank, the discharging time increases with the increasing inlet temperature. When the inlet temperature of HTF increase from 377 K to 427 K, the discharging time will increase from 10,130 s to 15,380 s, which increases about 51.82%. It can be seen that the inlet temperature of HTF has great influence on the discharging process of the TES tank in the CSP system, and the thermal energy release performance of the truncated cone TES tank is better than the cylindrical tank.

Figure 15 presents the effects of inlet temperature of HTF on the total released energy capacity and total energy release rate during the discharging process, which include the results of cylindrical TES tank under the inlet temperature at 377 K ("C-377" in Figure 15). And the total released energy capacity is calculated by equation (5). The total energy release rate is calculated by the following equation.

$$v_{Q'} = \frac{Q'}{t}, \quad (7)$$

where the  $v_{Q'}$  represents the total energy release rate

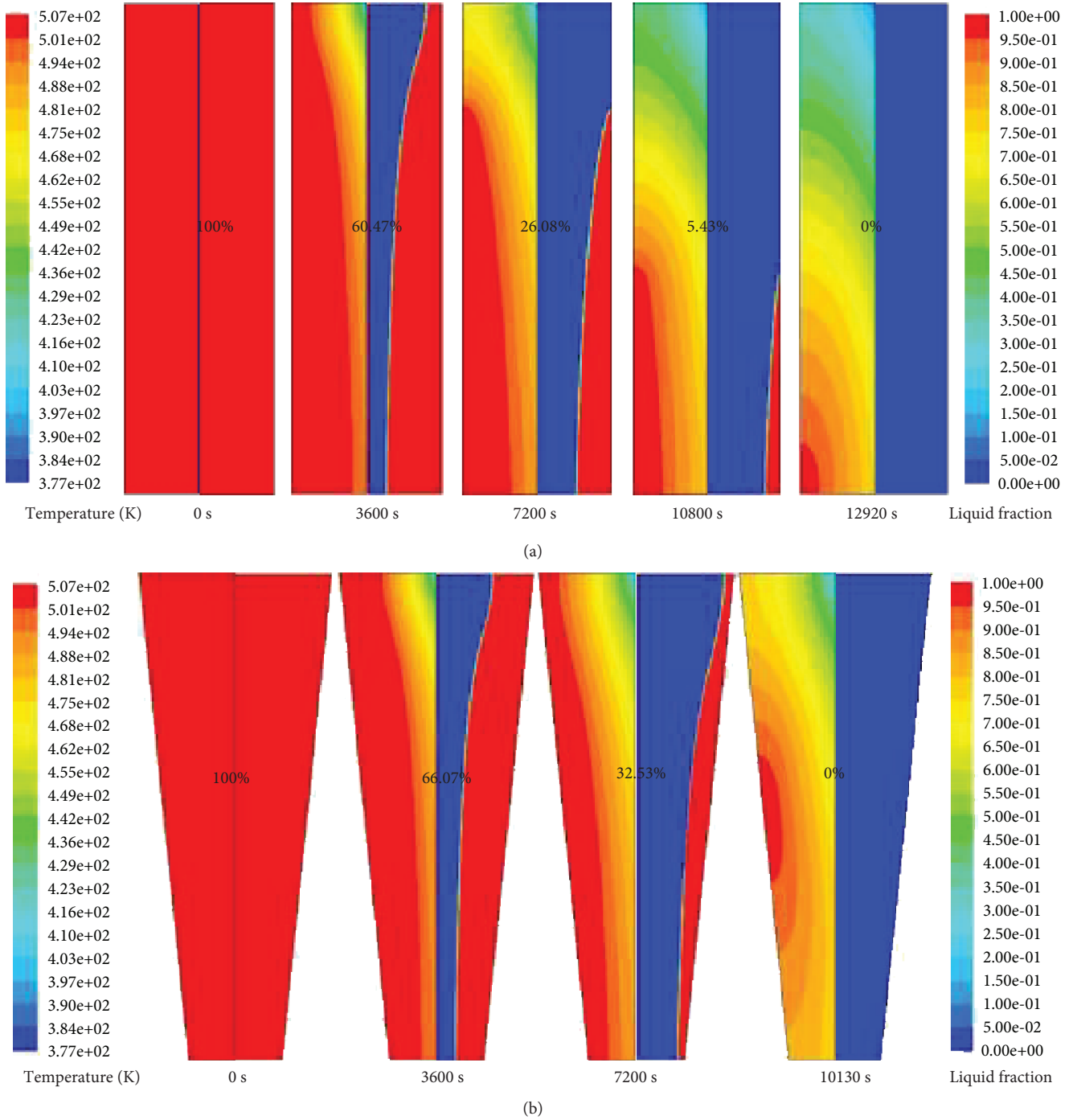


FIGURE 12: Contour of the PCM temperature (left) and liquid fraction (right) in the (a) cylindrical and (b) truncated cone model during the solidification process.

(J/s),  $Q'$  is the total released energy capacity (J), and  $t$  is the discharging time (s).

When the inlet temperature is 377 K, it can be seen that the total released energy capacity of the cylindrical tank (537.91 kJ) is much larger than that of the truncated cone TES tank (469.53 kJ). However, the energy release rate of the truncated cone tank is greater than that of the cylindrical tank, which increases 9.87% compared to the cylindrical

tank. It can be found that the heat energy utilization rate from the PCM of the truncated cone TES tank is higher than that of the cylindrical tank.

For truncated cone TES tank, the total released energy capacity decreases with the increase of the inlet temperature of HTF in Figure 15. And the initial inlet temperature of HTF increasing from 377 K to 427 K, the total released energy capacity will decrease from 469.53 kJ to 439.06 kJ, which

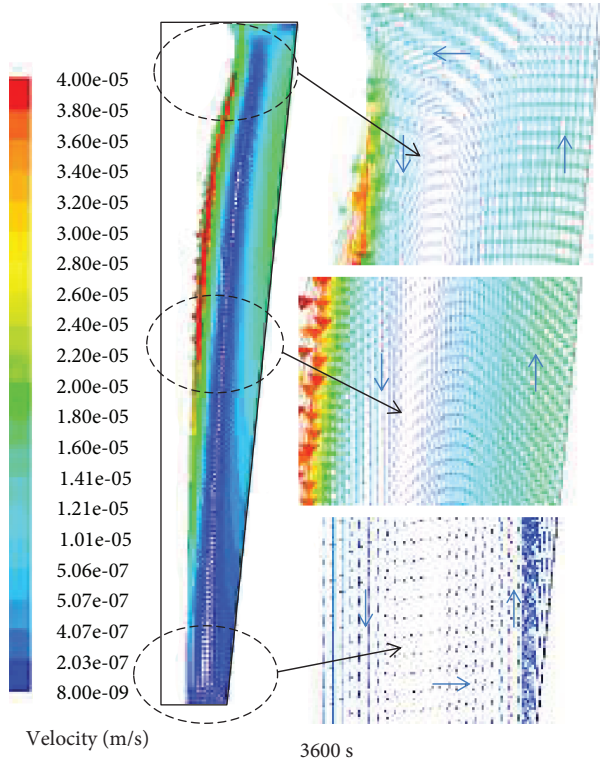


FIGURE 13: The simulated liquid PCM velocity field with truncated cone TES unit during discharging process.

reduces about 6.49%. Meanwhile, the curve shows that the total energy release rate decreases significantly with the increasing inlet temperature of HTF, and the initial inlet temperature increasing from 377 K to 427 K, the total energy release rate will decrease from 46.19 J/s to 28.48 J/s, which reduces about 38.34%.

**4.2.3. Effects of Inlet Velocity of HTF on Discharging Process.** In order to investigate the influence of inlet velocity of HTF on the discharging process of a truncated cone TES tank, according to the results of the inlet temperature for HTF on the heat discharging process, the inlet temperature of 397 K is selected to the study. The initial temperature of PCM is 507 K, and the inlet velocity of the HTF is six temperature gradients, including 0.2 m/s, 0.4 m/s, 0.6 m/s, 0.8 m/s, 1.0 m/s, and 1.2 m/s.

The effect of inlet velocity of HTF on liquid fraction and discharging process is shown in Figure 16. From the curves, the slope of curves is gradually decreasing during the discharging process. With the increase of the inlet velocity of HTF, the discharging time is gradually shortened, and the amplitude of the shortening is gradually reduced. Thus, the smaller the inlet velocity of the HTF is, the larger the effect on the discharging time of the TES tank is. The inlet velocity of HTF increasing from 0.2 m/s to 1.2 m/s, the discharging time will decrease from 19,270 s to 12,150 s, which reduces about 36.95%.

Figure 17 presents the effects of inlet velocity of HTF on the total released energy capacity and total energy release rate during the discharging process. From the

histograms and curve, the total released energy capacity and energy release rate increase with the increase of inlet velocity of HTF. And inlet velocity of HTF increasing from 0.2 m/s to 1.2 m/s, the released energy capacity will increase from 440.92 kJ to 455.36 kJ, which increases slightly about 3.27%. And the total energy release rate increases about 65.17%. This is because with the increase of the inlet velocity of the HTF, the total released energy capacity increases, while the total discharging time decreases gradually, which leads to the phenomenon that the total energy release rate increases greatly.

**4.3. Analysis of Heat Storage Efficiency of TES Tank.** In order to analyze the heat storage efficiency of the truncated cone TES tank, firstly, the heat storage efficiency is calculated by following equation.

$$\eta = \frac{Q'}{Q}, \quad (8)$$

where the  $Q'$  and  $Q$  is the total released energy capacity and total stored energy capacity, respectively.

Then, according to the above results, the stored and released energy capacity in a truncated cone TES tank has been calculated. In this process, the influence of the inlet temperature and velocity of the HTF on the heat storage efficiency of the truncated cone TES tank can be compared and analyzed.

Figure 18 shows the influence of the inlet temperature of the HTF on the storage efficiency of the TES tank, in which the  $x$ -axis is the inlet temperature of the HTF during the charging process, the  $y$ -axis is the heat storage efficiency, and the legend shows the inlet temperature of HTF during the discharging process.

From the diagram, it can be found that the heat storage efficiency decreases with the increase of the inlet temperature of HTF in the charging process. And the maximum heat storage efficiency of the TES tank can reach 93% and the minimum is about 58%, which indicated that the inlet temperature of the HTF has a great influence on the heat storage efficiency of the TES system in CSP plant.

When the inlet temperature of the HTF is constant during the charging process, the higher the inlet temperature of the HTF during the discharging process is, the lower the heat storage efficiency of the TES tank is. Meanwhile, when the inlet temperature of the HTF is constant during the discharging process, the higher the inlet temperature of the HTF during the charging process is, the lower the heat storage efficiency of the TES tank is. Compared with the discharging process, the inlet temperature of HTF in the charging process has the more significant effect on the heat storage efficiency. As a whole, the lower the inlet temperature of the HTF is, the higher the thermal energy utilization efficiency is, that is, the higher the heat storage efficiency of the TES tank is.

The influence of the inlet velocity of the HTF on the storage efficiency of the TES tank is shown in Figure 19, in which the  $x$ -axis is the inlet velocity of the HTF during the charging process, the  $y$ -axis is the heat storage efficiency,

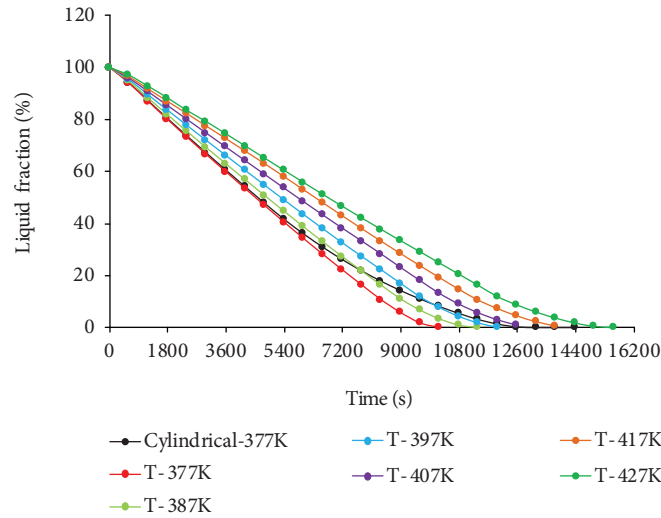


FIGURE 14: Effects of initial inlet temperature of HTF on liquid fraction.

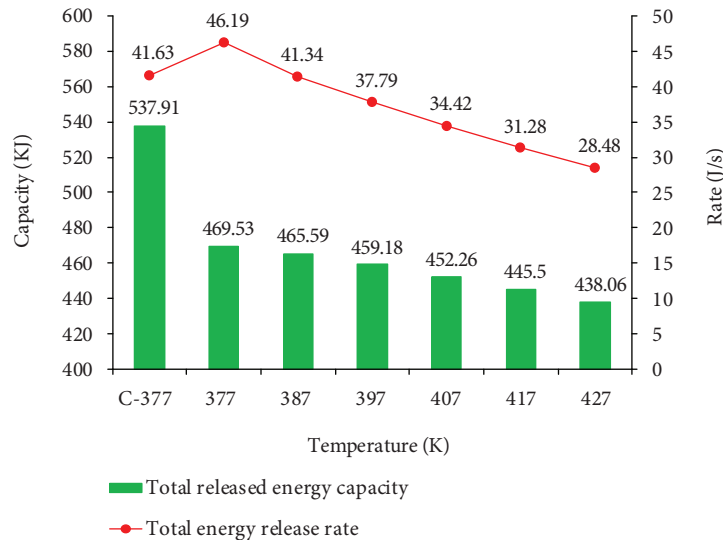


FIGURE 15: Effects of inlet temperature of HTF on the total released energy capacity and energy release rate.

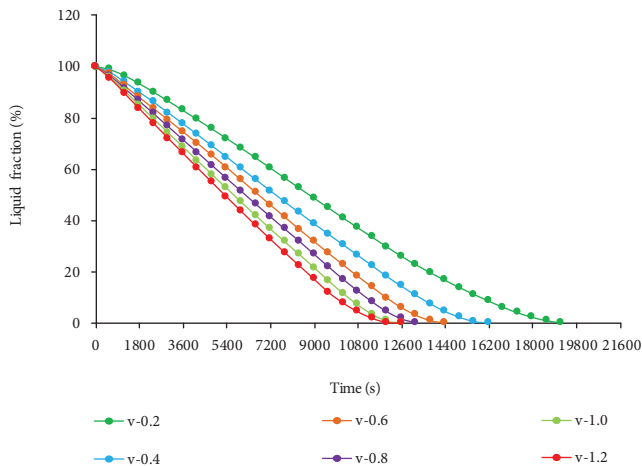


FIGURE 16: Effects of inlet velocity of HTF on liquid fraction.

and the legend shows the inlet velocity of HTF during the discharging process.

It can be found that the heat storage efficiency decreases with the increase of the inlet velocity of HTF in the charging process. In the calculation range, the range of heat storage efficiency of a truncated cone TES tank is 80% ~ 65%, and the effect of velocity on the heat storage efficiency of TES tank is slighter than the influence of the inlet temperature of HTF on it.

When the inlet velocity of the HTF is constant during the charging process, the higher the inlet velocity of the HTF during the discharging process is, the higher the heat storage efficiency of the heat storage tank is. However, when the inlet velocity of the HTF is constant during the discharging process, the higher the inlet velocity of the HTF during the charging process is, the lower the heat storage efficiency of the TES tank is. And compared with the discharging

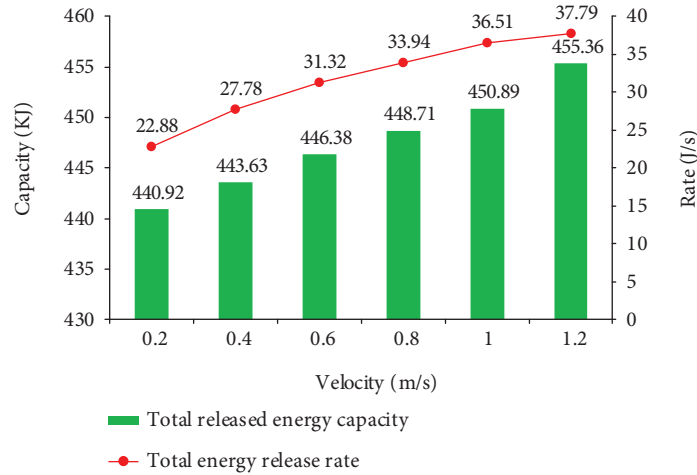


FIGURE 17: Effects of inlet velocity of HTF on the total released energy capacity and energy release rate.

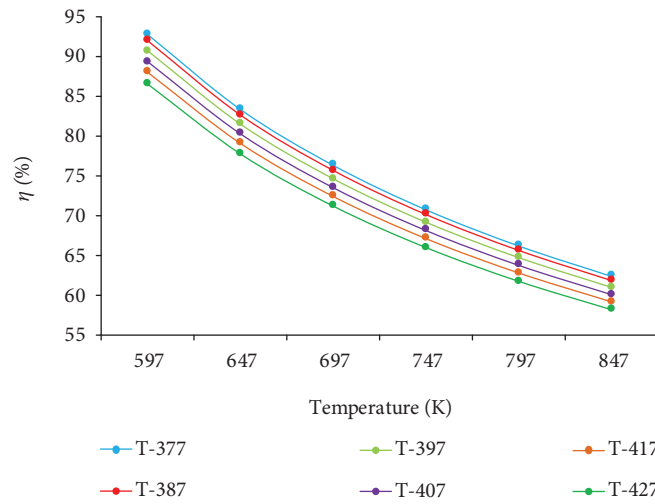


FIGURE 18: Effect of inlet temperature of HTF on heat storage efficiency.

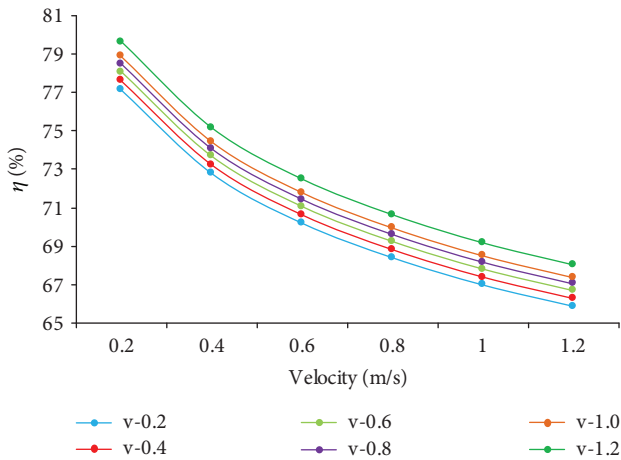


FIGURE 19: Effect of inlet velocity of HTF on heat storage efficiency.

process, the inlet velocity of HTF in the charging process has also the more significant effect on the heat storage efficiency. As a whole, the lower the inlet velocity of the HTF is during the charging process and the higher the inlet velocity of HTF is during the discharging process, the higher the thermal energy utilization efficiency is, that is, the higher the heat storage efficiency of the TES tank is in the CSP system. It can be concluded that the inlet condition (temperature and velocity) of HTF in the charging process has the more obvious impact on the heat storage efficiency of TES system in CSP technology.

### 5. Conclusions

Developing CSP technology is one of the most effective ways to solve energy shortage all over the world. And the TES system is the key to improve the performance of CSP system. In this paper, a two dimensional physical and mathematical model for a novel truncated cone shell-and-tube TES tank has been established based on enthalpy method. Then, the

charging/discharging process of the cylindrical tank and the novel tank has been compared. Meanwhile, the effects of inlet conditions of HTF, and thickness of tube on the charging/discharging process, and heat storage efficiency have been investigated. The following conclusions can be drawn.

- (1) Comparing the performance between cylindrical and truncated cone TES tank, it can be seen that the performance of truncated cone tank is better under the same operating condition, which reduces the charging/discharging time about 32.08% and 21.59%, respectively. And the velocity field of liquid PCM during the charging/discharging process shows clockwise/anticlockwise convection circulation
- (2) The effect of thickness of tube on the charging process of PCM is slight, so the effect of wall thickness on the TES system can be ignored
- (3) During the charging process, with the increase of the inlet temperature of HTF, the charging time reduces about 58.56%, and the stored energy capacity and energy storage rate increase about 48.69% and four times. With the increasing inlet velocity, the melting time reduces about 38.48%, and the stored energy capacity and energy storage rate increase about 17.08% and double. However, the thermal energy utilization rate of HTF is very low
- (4) During the discharging process, with the increase of inlet temperature of HTF, the discharging time increases 51.82%, and the released energy capacity and energy release rate reduce about 6.49% and 38.34%, respectively. With the increasing velocity, the discharging time reduces about 36.95%, and the released energy capacity and energy release rate will increase about 3.27% and 65.17%, respectively
- (5) For the heat storage efficiency, the maximum heat storage efficiency of the truncated cone TES tank can reach 93% in the range of the simulation
- (6) Therefore, the initial operating condition of HTF is the significant factor in the practical applications of the CSP system. Particularly, some appropriate methods should be studied for reducing the loss of energy and improving the thermal energy utilization rate of HTF in the next study. And this researcher will provide the significant reference towards geometric design and operating conditions by considering the effect of natural convection on the TES system in the CSP plants

## Nomenclature

$C_p$ :	Specific heat, J/(kg·K)
$f$ :	Liquid fraction
$h$ :	Heat transfer coefficient, W/m <sup>2</sup> ·K
$v$ :	Velocity, m/s
$v_{\max}$ :	The maximum velocity, m/s
$P_r$ :	Prandtl number

$R_e$ :	Reynolds number
$Re_{\max}$ :	The maximum Reynolds number
$Q$ :	Total stored energy capacity, J
$Q'$ :	Total released energy capacity, J
$t$ :	Charging/discharging time, s
$v_Q$ :	Total energy storage rate, J/s
$v_{Q'}$ :	Total energy release rate, J/s
$m$ :	The mass of the PCM, kg
$R_{in}$ :	The radius of the inner tube, mm
$R$ :	The radius of the shell side or the top of the truncated cone model, mm
$r$ :	The radius of the bottom of the truncated cone model, mm
$a$ :	The thickness of the tube, mm
$L$ :	The length of the PCM unit, mm
$T$ :	Temperature, K
$T_m$ :	Melting point temperature of PCM, K
$T_a$ :	The average temperature of PCM, K
$T_0$ :	The initial temperature, K
CSP:	Concentrated solar power
PCM:	Phase change material
TES:	Thermal energy storage
HTF:	Heat transfer fluid
LHTES:	Latent heat thermal energy storage

## Greek Symbols

$\rho$ :	Density, kg/m <sup>3</sup>
$\lambda$ :	Thermal conductivity, W/m·K
$\lambda_p$ :	Thermal conductivity of PCM in $r$ direction, W/m·K
$\lambda'_p$ :	Thermal conductivity of PCM in $x$ direction, W/m·K
$\Delta H$ :	Enthalpy, kJ/kg
$\eta$ :	Heat storage efficiency

## Data Availability

The data used to support the findings of this study are available from the corresponding author upon request.

## Conflicts of Interest

The authors declare that there is no conflict of interests regarding the publication of this paper.

## Acknowledgments

This work is supported by the National Natural Science Foundation of China (Nos. 51876147 and 51406033). Besides, a very special acknowledgement is made to the editors and referees who made important comments to improve this paper.

## References

- [1] Z. D. Cheng, Y. L. He, F. Q. Cui, R. J. Xu, and Y. B. Tao, "Numerical simulation of a parabolic trough solar collector with nonuniform solar flux conditions by coupling FVM and MCRT method," *Solar Energy*, vol. 86, no. 6, pp. 1770–1784, 2012.

- [2] B. Xu, P. Li, and C. Chan, "Application of phase change materials for thermal energy storage in concentrated solar thermal power plants: a review to recent developments," *Applied Energy*, vol. 160, pp. 286–307, 2015.
- [3] Q. Mao, "Recent developments in geometrical configurations of thermal energy storage for concentrating solar power plant," *Renewable and Sustainable Energy Reviews*, vol. 59, pp. 320–327, 2016.
- [4] S. Kuravi, J. Trahan, D. Y. Goswami, M. M. Rahman, and E. K. Stefanakos, "Thermal energy storage technologies and systems for concentrating solar power plants," *Progress in Energy and Combustion Science*, vol. 39, no. 4, pp. 285–319, 2013.
- [5] G. Alva, L. Liu, X. Huang, and G. Fang, "Thermal energy storage materials and systems for solar energy applications," *Renewable and Sustainable Energy Reviews*, vol. 68, pp. 693–706, 2017.
- [6] A. K. Pandey, M. S. Hossain, V. V. Tyagi, N. Abd Rahim, J. A. L. Selvaraj, and A. Sari, "Novel approaches and recent developments on potential applications of phase change materials in solar energy," *Renewable and Sustainable Energy Reviews*, vol. 82, pp. 281–323, 2018.
- [7] H. J. Xu and C. Y. Zhao, "Thermal performance of cascaded thermal storage with phase-change materials (PCMs). Part I: steady cases," *International Journal of Heat and Mass Transfer*, vol. 106, pp. 932–944, 2017.
- [8] Y. Q. Li, Y. L. He, H. J. Song, C. Xu, and W. W. Wang, "Numerical analysis and parameters optimization of shell-and-tube heat storage unit using three phase change materials," *Renewable Energy*, vol. 59, pp. 92–99, 2013.
- [9] G. Wei, G. Wang, C. Xu et al., "Selection principles and thermophysical properties of high temperature phase change materials for thermal energy storage: a review," *Renewable and Sustainable Energy Reviews*, vol. 81, pp. 1771–1786, 2018.
- [10] M. Avci and M. Y. Yazici, "Experimental study of thermal energy storage characteristics of a paraffin in a horizontal tube-in-shell storage unit," *Energy Conversion and Management*, vol. 73, pp. 271–277, 2013.
- [11] M. Dadollahi and M. Mehrpooya, "Modeling and investigation of high temperature phase change materials (PCM) in different storage tank configurations," *Journal of Cleaner Production*, vol. 161, pp. 831–839, 2017.
- [12] Y. B. Tao and Y. L. He, "Numerical study on thermal energy storage performance of phase change material under non-steady-state inlet boundary," *Applied Energy*, vol. 88, no. 11, pp. 4172–4179, 2011.
- [13] Y. Fang, J. Niu, and S. Deng, "Numerical analysis for maximizing effective energy storage capacity of thermal energy storage systems by enhancing heat transfer in PCM," *Energy and Buildings*, vol. 160, pp. 10–18, 2018.
- [14] M. R. Assari, H. Basirat Tabrizi, and M. Savadkoyh, "Numerical and experimental study of inlet-outlet locations effect in horizontal storage tank of solar water heater," *Sustainable Energy Technologies and Assessments*, vol. 25, pp. 181–190, 2018.
- [15] S. Seddegh, M. M. Joybari, X. Wang, and F. Haghightat, "Experimental and numerical characterization of natural convection in a vertical shell-and-tube latent thermal energy storage system," *Sustainable Cities and Society*, vol. 35, pp. 13–24, 2017.
- [16] Y. B. Tao and Y. L. He, "Effects of natural convection on latent heat storage performance of salt in a horizontal concentric tube," *Applied Energy*, vol. 143, pp. 38–46, 2015.
- [17] J. C. Kurnia and A. P. Sasmito, "Numerical investigation of heat transfer performance of a rotating latent heat thermal energy storage," *Applied Energy*, vol. 227, pp. 542–554, 2018.
- [18] X. Gao, P. Wei, Y. Xie et al., "Experimental investigation of the cubic thermal energy storage unit with coil tubes," *Energy Procedia*, vol. 142, pp. 3709–3714, 2017.
- [19] M. Parsazadeh and X. Duan, "Numerical study on the effects of fins and nanoparticles in a shell and tube phase change thermal energy storage unit," *Applied Energy*, vol. 216, pp. 142–156, 2018.
- [20] X. Yang, Z. Lu, Q. Bai, Q. Zhang, L. Jin, and J. Yan, "Thermal performance of a shell-and-tube latent heat thermal energy storage unit: role of annular fins," *Applied Energy*, vol. 202, pp. 558–570, 2017.
- [21] M. E. H. Amagour, A. Rachek, M. Bennajah, and M. Ebn Touhami, "Experimental investigation and comparative performance analysis of a compact finned-tube heat exchanger uniformly filled with a phase change material for thermal energy storage," *Energy Conversion and Management*, vol. 165, pp. 137–151, 2018.
- [22] J. Gasia, J. Diriken, M. Bourke, J. van Bael, and L. F. Cabeza, "Comparative study of the thermal performance of four different shell-and-tube heat exchangers used as latent heat thermal energy storage systems," *Renewable Energy*, vol. 114, pp. 934–944, 2017.
- [23] F. Zhu, C. Zhang, and X. Gong, "Numerical analysis and comparison of the thermal performance enhancement methods for metal foam/phase change material composite," *Applied Thermal Engineering*, vol. 109, pp. 373–383, 2016.
- [24] M. Eslami and M. A. Bahrami, "Sensible and latent thermal energy storage with constructal fins," *International Journal of Hydrogen Energy*, vol. 42, no. 28, pp. 17681–17691, 2017.
- [25] M. Parsazadeh and X. Duan, "Numerical and statistical study on melting of nanoparticle enhanced phase change material in a shell-and-tube thermal energy storage system," *Applied Thermal Engineering*, vol. 111, pp. 950–960, 2017.
- [26] S. Bellan, T. E. Alam, J. González-Aguilar et al., "Numerical and experimental studies on heat transfer characteristics of thermal energy storage system packed with molten salt PCM capsules," *Applied Thermal Engineering*, vol. 90, pp. 970–979, 2015.
- [27] F. Ma and P. Zhang, "Investigation on the performance of a high-temperature packed bed latent heat thermal energy storage system using Al-Si alloy," *Energy Conversion and Management*, vol. 150, pp. 500–514, 2017.
- [28] A. Abdulla and K. S. Reddy, "Effect of operating parameters on thermal performance of molten salt packed-bed thermocline thermal energy storage system for concentrating solar power plants," *International Journal of Thermal Sciences*, vol. 121, pp. 30–44, 2017.
- [29] M. A. Kibria, M. R. Anisur, M. H. Mahfuz, R. Saidur, and I. H. S. C. Metselaar, "Numerical and experimental investigation of heat transfer in a shell and tube thermal energy storage system," *International Communications in Heat and Mass Transfer*, vol. 53, pp. 71–78, 2014.
- [30] Y. B. Tao and Y. L. He, "Numerical study on performance enhancement of shell-and-tube latent heat storage unit,"

*International Communications in Heat and Mass Transfer*, vol. 67, pp. 147–152, 2015.

- [31] K. S. Reddy, V. Mudgal, and T. K. Mallick, “Review of latent heat thermal energy storage for improved material stability and effective load management,” *Journal of Energy Storage*, vol. 15, pp. 205–227, 2018.
- [32] Q. Mao, H. Chen, Y. Zhao, and H. Wu, “A novel heat transfer model of a phase change material using in solar power plant,” *Applied Thermal Engineering*, vol. 129, pp. 557–563, 2018.